Surface Waves on Periodic Structures at Microwave Frequencies

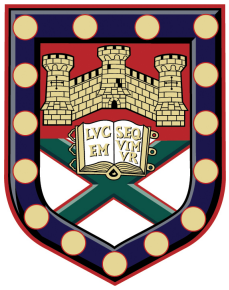

Helen Jennifer Rance
School of Physics
University of Exeter

Thesis submitted to The University of Exeter
for the degree of Doctor of Philosophy in Physics

July 2013

Submitted by Helen Jennifer Rance to the University of Exeter as a thesis for the degree of Doctor of Philosophy in Physics

July 2013

I certify that all material in this thesis which is not my own work has been identified and that no material has previously been submitted and approved for the award of a degree by this or any other University.

Helen Jennifer Rance
July 2013

Abstract

Experimental investigations of structurally-dictated surface waves supported by periodically textured metallic substrates with different symmetries, are the primary focus of the work presented in this thesis. The electromagnetic response of three near perfectly conducting substrates perforated with arrays of holes with different geometries, together with a low-profile high-impedance structure are characterised. Experimental measurement techniques are employed to record the transmission, and reflection from the structures under investigation, together with phase-resolved measurements to directly obtain the dispersion of the surface waves supported by these structures. From these measurements information about the nature of the surface modes supported by the structures under investigation can be observed.

A study of diffractively coupled surface waves supported by a close-packed array of square cross-section, close-ended holes in the limit where the wavelength of incident radiation and periodicity of the hole array are comparable, is presented. An additional grating, which has a periodicity comparable to the hole array is used to control the strength of diffractive coupling to the mode. Using a free-space measurement technique, information about the dispersion of the modes supported by the structure is obtained by recording the azimuthal-dependent reflection from the structure. It is found that the relative positions of the hole array and 'coupling-in' grating is significant, a key issue not addressed in the literature when investigating grating-coupling to surface modes. Good agreement with numerical predictions is demonstrated.

Structurally-dictated surface waves on a metallic substrate pierced by a close-packed array of deep, rectangular holes is characterised. In this arrangement, the fundamental resonance in the holes in the orthogonal directions is different and the frequency therefore to which the dispersion of the surface waves supported by the structure is limited, varies with sample orientation. The anisotropic dispersion, resulting from an ellipsoid of limiting frequencies, is directly mapped using a phase-resolved measurement technique. Furthermore by exploiting the anisotropy of the unit cell, a family of higher order surface waves associated with the quantisation of the electromagnetic fields within the holes is explored in this chapter. Once again good agreement with numerical predictions is shown.

The 'enhanced transmission' recorded through a 'zigzag' hole array, attributed to the excitation of diffractively coupled surface waves, is explored. Due to the specific symmetry of the unit cell of the zigzag hole array it is shown that coupling to these surface waves can be achieved with both transverse magnetic and transverse electric polarised incident radiation. Further, incident radiation can directly couple to the surface modes supported by the zigzag hole array, via scattering from its inherent *in-plane* periodicity. The observed polarisation-selective excitation of individual surface wave bands, agrees well with numerical predictions and is shown to be a direct consequence of the reduced symmetry of the system.

Finally, the dispersion of the modes supported by an ultra-thin, high-impedance surface in the form of a Sievenpiper 'mushroom' structure, with rectangular geometry is directly recorded. The behaviour of the Sievenpiper structure is rather complex and to aid understanding of the electromagnetic response of the structure, the results are compared with the modes supported by a simpler patch array structure. The anisotropy arising from the rectangular geometry is characterised and an in depth discussion of the origin of the modes presented.

Contents

List of Figures

Acknowledgements

Particularly in the last month I have appreciated just how much of a team effort completing a PhD is and I would like to thank all those people that have got me to where I am today. Firstly I would like to thank my supervisors Professor Roy Sambles and Professor Alastair Hibbins for their support and encouragement over the last four years, and for constantly challenging me in those early morning Wednesday meetings! I would like to thank my Mentor Alan Usher, for keeping me on the straight and narrow, and I would also like to give Matt and Ian a special mention. Their roles as unofficial Mentors/Supervisors have guided me through the last fours years. My experience as a PhD student would not have been the same without you both around.

Thank you too to Team Basement members past and present: Alfie, Caz, Nixon, Eddy Stones, Steve, Tom, Luke, Tim ('keep going' Helen), and Chris. As well as all group members for their useful discussions along the way. Also I would like to thank the workshop boys, in particular Nick, you have been a legend!

Chris, thank you for all the 'not long nows' and my Sister Alison for all the random chats to bring me back to reality after being stuck in the depth of thesis blues. Lastly I would like to thank my Mum and Dad, I hope I have made you proud.

Chapter 1

Introduction

1.1 Aim of Research

The electromagnetic (EM) response of metals at low frequencies is dominated by their high conductivities, such that in general, they can be regarded as near-perfect electrical conductors and cannot support bound surface modes. However, adding texture to the surface of a near-perfect conductor can greatly alter the electromagnetic boundary conditions at the surface, such that, even in the region of the EM spectrum where fields are almost completely excluded from the metal, bound EM surface states can be induced.

This concept was first extensively studied around the 1950s [7–11] and later by Culter [12]. More recently, Pendry and his co-workers [3, 4] revisited the study of surface waves on corrugated metals by connecting the earlier work of radar engineers in the mid-20^{th} century with the study of surface waves in the optical regime (known as surface plasmon polaritons (SPPs)), thus opening up the field of plasmonics to the low frequency domain. Pendry *et. al* proposed that a perforated surface of a highly conducting substrate can support surface plasmon polariton (SPP)-like modes, the dispersion of which can almost arbitrarily be scaled to any frequency through structure rather than material composition. The 2D version of which is similar to, but much thicker than, that analysed by Ulrich and Tacke [13] in earlier work, with the addition of a lossless dielectric material inside the cavities which acts to reduce the cutoff frequency for light propagating in the holes. The experimental verification of the concept introduced by Pendry *et al.* soon followed [2], thus igniting the interest these geometrically induced surface modes supported at low frequencies, commonly referred to as 'designer' or 'spoof' surface plasmons. Subsequently a wealth of studies followed, the details of which will be discussed throughout this thesis.

The work presented in this thesis focuses on the experimental investigation of structurally-dictated or 'designer' surface waves supported by periodically textured metallic (pseudo-plasmonic) structures in the microwave regime. It is from the study of Hibbins *et al.* [2] that the work in this thesis follows, however, the concept of pseudo-plasmonic surfaces

at microwave frequencies is extended to include structures with a high degree of surface anisotropy. Through the work discussed in this thesis, it has been shown that increasing the anisotropy of a structure through the modification of the shape and/or arrangement of the constituent subwavelength elements allows access to modes and phenomena unavailable in structures with higher symmetry.

1.2 Thesis Outline

The work presented in this thesis details the experimental investigation in the microwave regime of structurally-dictated surface waves supported by periodically textured metallic substrates, the properties of which, are determined by the geometry of the structure.

With the primary focus on surface waves supported by near-perfectly conducting substrates perforated with arrays of holes, three different geometries are considered. Initially an array of square cross-section holes are investigated, however the concept of structurally-dictated surface waves is extended to include structures with a higher degree of surface anisotropy; arrays comprising holes with a rectangular cross-section and a novel 'zigzag' geometry are also characterised. Finally, the anisotropy arising from the rectangular geometry of a low-profile structure commonly referred to as the Sievenpiper 'mushroom' structure, is explored.

The background theory for surface waves is presented in Chapter 2; where a brief summary of the properties of surface plasmons polaritons (SPPs) supported by metals at optical frequencies is presented, before 'spoof' surface plasmons supported by textured metallic structures at microwave frequencies are discussed.

Details of the method used to simulate the electromagnetic response of the structures under investigation in this thesis are presented in Chapter 3, together with the techniques employed to obtain the experimental data. The apparatus upon which free-space microwave reflection and transmission measurements are performed is discussed, as well as details of the blade-coupling and phase-resolved measurement techniques employed to directly record the dispersion of surface modes.

In Chapter 4, a thorough study of diffractively coupled surface waves supported by a close-packed array of square cross-section close-ended holes is presented. This study is particularly concerned with the limit where the wavelength of incident radiation and periodicity of the hole array are comparable. An additional grating, which has a periodicity comparable to the hole array, is used to control the strength of diffractive coupling to the mode. Information about the dispersion of the modes supported by the structure is obtained by recording the reflection from the structure using a free-space measurement technique. It is found that the relative positions of the hole array and 'coupling-in' grating is significant, a key issue not addressed in the literature when

investigating grating-coupling to surface modes.

Structurally-dictated surface waves on a metallic substrate pierced by a close-packed array of deep, rectangular holes is characterised in Chapter 5. In this arrangement, the fundamental resonance in the holes in the orthogonal directions is different and the frequency therefore to which the dispersion of the surface waves supported by the structure is limited, varies with sample orientation. The anisotropic dispersion, resulting from an ellipsoid of limiting frequencies, is directly mapped. Blade-coupling techniques are used to excite the modes and phase resolved measurements to determine their dispersion. Furthermore, by exploiting the anisotropy of the unit cell, a family of higher order surface waves associated with the quantisation of the electromagnetic fields within the holes is also explored in this chapter.

In Chapter 6 the 'enhanced transmission' recorded through a 'zigzag' hole array attributed to the excitation of diffractively coupled surface waves is explored. Due to the specific symmetry of the unit cell of the zigzag hole array it is shown that coupling to these surface waves can be achieved with both transverse magnetic and transverse electric polarised incident radiation. Further, incident radiation can directly couple to the surface modes supported by the zigzag hole array, via scattering from its inherent *in-plane* periodicity. Of particular interest in this chapter however, is the observed polarisation-selective excitation of individual surface wave bands, the behaviour of which is shown to be a direct consequence of the reduced symmetry of the system.

The final experimental results are presented in Chapter 7. In this chapter the dispersion of the modes supported by an ultra-thin, high-impedance surface in the form of a Sievenpiper 'mushroom' structure, with rectangular geometry are directly recorded using the same techniques as in Chapter 5. The behaviour of the Sievenpiper structure is rather complex and to aid understanding of the electromagnetic response of the structure, the results are compared with the modes supported by a simpler patch array structure. The anisotropy arising from the rectangular geometry is characterised and an in-depth discussion of the origin of the modes presented.

Finally in Chapter 8 conclusions are made and suggestions for future study are presented.

Chapter 2

Background Theory

2.1 Introduction

The electromagnetic (EM) response of metals at low frequencies is dominated by their high conductivities, such that in general, they can be regarded as near-perfect electrical conductors and cannot support bound surface modes. However, adding texture to the surface of a near-perfect conductor can greatly alter the electromagnetic boundary conditions at the surface, such that, even in the region of the EM spectrum where fields are almost completely excluded from the metal, bound EM surface states can be induced.

The focus of the work presented in this thesis is exclusively that of surface waves supported by periodically textured structures in the microwave regime. Recently Pendry [3] revisited the study of surface waves on corrugated metals by connecting the work of radar engineers in the mid-20^{th} century [9, 11] with the study of surface waves in the optical regime (known as surface plasmon polaritons (SPPs)). In doing so, these geometrically induced surface modes have since become known as 'designer' or 'spoof' surface plasmons modes, the dispersion of which can almost arbitrarily be scaled to any frequency through structure rather than material composition.

A general understanding of surface waves supported at the interface between a metal and dielectric is required before looking into the specifics of the surface waves supported by structures at low frequencies. An overview of surface waves is presented in Section 2.2, whilst a discussion of 'spoof' surface plasmons and an overview of waveguide modes is presented in Section 2.3.

2.2 Surface Waves

Surface waves are electromagnetic modes with fields localised at the interface between a metal and dielectric. In 1941 Fano [14] investigated a trapped EM wave travelling by total internal reflection within a glass overlayer of finite thickness on a metallic substrate, he derived an equation relating the thickness of the glass overlayer to the

normal and tangential components of the wavevector of the trapped wave solution. Upon studying the system in the limit of the thickness of the glass overlayer tending to zero, he discovered that a single valid solution for Maxwell's equations remained, in which a wave travelled along the surface, bound with fields that decay exponentially into the bounding media (what later became known as a 'surface plasmon polariton' (SPP) [15]). From this, the study of SPPs has progressed to the point where the phenomenon is well understood [16].

A surface plasmon is a longitudinal oscillation of surface charge at the interface between a metal and a dielectric, which when coupled to by incident radiation is known as a surface plasmon polariton. The mode is a 'trapped' surface wave which decays exponentially away from the interface into the bounding media. Transverse magnetic (TM), (or p-polarised) radiation is required to excite a SPP on a planar surface since the incident electric vector needs to have a component normal to the interface in order for the required polarisation charge to be generated.

Due to the frequency-dependence of the dielectric function of the metal, when moving from the visible to GHz regime, the properties of surface waves do not scale with wavelength. At low frequencies, the electromagnetic response of metals is dominated by a large imaginary and large (negative) real part of the permittivity, resulting in long propagation distances of the mode but weak localisation of the field at the surface. In other words, the surface does not serve to localise the energy associated with the phenomena, rather it serves to guide the wave. Early investigations into these guided waves were reported by Zenneck in 1907 [17] who found that Maxwell's equations had a solution corresponding to a wave coupled to an interface bounded by a dielectric (air) and a medium with finite conductivity (salt). Soon after, Sommerfeld published work in which the propagation of radio waves along the surface of the earth were investigated [18].

It was not until the 1940s and the advent of radar development during World War II that microwave theory and technology received substantial interest. From these studies it was shown that surface roughness or dielectric layers could be used to bind a wave propagating at the interface between a metal and dielectric over-layers at low frequencies, decreasing the velocity of the wave [7–12]. The former method (surface roughness) will be discussed exclusively within this thesis. More recently Pendry [3] re-ignighted interest in the field of surface waves supported by periodic structures, introducing the concept of 'spoof' or 'designer' surfaces waves. Pendry *et al.* showed that one can mimic the behaviour of surface plasmon polaritons for frequencies far below the plasma frequency by structuring the surface of perfect conductor (i.e. one with finite conductivity).

Although the focus of the work presented in this thesis is exclusively in the microwave regime, a general understanding of surface plasmons is required before looking into the

specifics of the surface waves supported by periodic structures at low frequencies.

2.2.1 The Dispersion of Surface Plasmon Polaritons Propagating on a Planar Surface

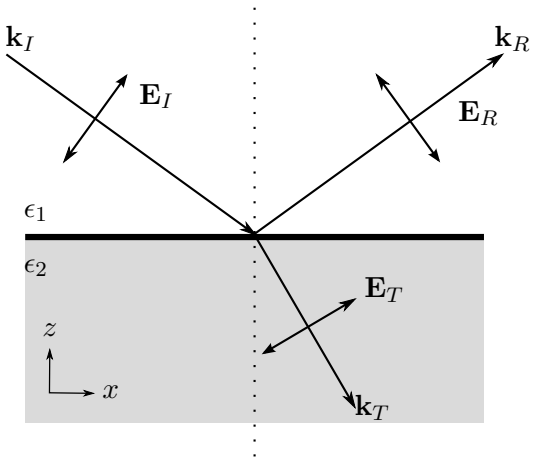

(a)

Figure 2.1: A schematic representation of radiation with wavevector $\mathbf{k}_I$ incident on an interface bounded by two media characterised by permittivites ϵ_1 and ϵ_2.

For a planar interface between two semi-infinite, isotropic non-magnetic media, the normal component of the electric displacement $\mathbf{D}$ must be continuous across the interface. The electric displacement $\mathbf{D}$ is related to the electric field $\mathbf{E}$ via the following expression

$$\mathbf{D} = \epsilon_r \epsilon_0 \mathbf{E}, \tag{2.2.1}$$

where ϵ_r and ϵ_0 are the dielectric constant and permittivity of free space, respectively. Hence if the lower medium (grey shaded region Fig. 2.1) is metal (i.e. ϵ_r is negative at visible frequencies) and the upper medium (unshaded region Fig. 2.1) is a dielectric (i.e. ϵ_r is positive), the normal component of $\mathbf{E}$ must change direction at the interface to fulfill the continuity requirement of $\mathbf{D}$. It is this discontinuity in the normal component of $\mathbf{E}$ that 'traps' the polarisation charge at the surface.

Figure 2.1 shows the reflected and transmitted beam for TM propagating light with wavevector $\mathbf{k} = (k_x, k_y, 0)$ incident upon the interface. The electric and magnetic fields have the forms

$$\mathbf{E} = [E_x, 0, E_z]\exp(i(k_x\hat{x} + k_z\hat{z} - \omega t)), \tag{2.2.2}$$

and

$$\mathbf{H} = [0, H_y, 0]\exp(i(k_x\hat{z} + k_z\hat{z} - \omega t)), \tag{2.2.3}$$

where ω is the angular frequency and t is time.

Applying Maxwell's equation

$$\nabla \times \mathbf{H} = \epsilon\frac{\partial \mathbf{E}}{\partial t}, \tag{2.2.4}$$

results in

$$H_y = \frac{\epsilon\omega E_x}{k_z} = \frac{-\epsilon\omega E_z}{k_x}. \tag{2.2.5}$$

Combining equation 2.2.5 with the field equations 2.2.2 and 2.2.3 results in the following equations for the incident, reflected and transmitted field.

$$\mathbf{E}^I = E_x^I[1, 0, -\frac{k_{x1}}{k_{z1}}]\exp(i(k_{x1}\hat{x} + k_{z1}\hat{z} - \omega t)) \tag{2.2.6}$$

$$\mathbf{E}^R = E_x^R[1, 0, +\frac{k_{x1}}{k_{z1}}]\exp(i(k_{1x}\hat{x} - k_{z1}\hat{z} - \omega t)) \tag{2.2.7}$$

$$\mathbf{E}^T = E_x^T[1, 0, -\frac{k_{x2}}{k_{z2}}, 0]\exp(i(k_{x2}\hat{x} + k_{z2}\hat{z} - \omega t)) \tag{2.2.8}$$

$$\mathbf{H}^I = E_x^I[0, +\frac{\omega\epsilon_1}{k_{z1}}, 0]\exp(i(k_{x1}\hat{x} + k_{z1}\hat{z} - \omega t)) \tag{2.2.9}$$

$$\mathbf{H}^R = E_x^R[0, -\frac{\omega\epsilon_1}{k_{z1}}, 0]\exp(i(k_{x1}\hat{x} - k_{z1}\hat{z} - \omega t)) \tag{2.2.10}$$

$$\mathbf{H}^T = E_x^T[0, \frac{\omega\epsilon_2}{k_{z2}}, 0]\exp(i(k_{x2}\hat{x} + k_{z2}\hat{z} - \omega t)) \tag{2.2.11}$$

The SPP is a non-radiative mode, i.e. a 'trapped' surface wave, it is therefore possible for the incident field to be set to zero. Further, the tangential boundary condition state that the tangential components of both the electric and magnetic fields must be continuous across the interface.

$$E_x^R = -E_x^T \tag{2.2.12}$$

and

$$H_y = E_x^R\frac{\epsilon_1\omega}{k_{z1}} = -E_x^T\frac{\epsilon_2\omega}{k_{z2}} \tag{2.2.13}$$

Combining equations 2.2.12 and 2.2.13 results in

$$\frac{\epsilon_1}{k_{z1}} = -\frac{\epsilon_2}{k_{z2}}. \tag{2.2.14}$$

Conservation of tangential momentum requires the in-plane wavevector to be conserved at a planar boundary $k_{x1} = k_{x2} = k_x$. Therefore the z-component of the wavevector in medium m may be expressed as

$$k_{zm} = \sqrt{\epsilon_m k_0^2 - k_x^2}, \tag{2.2.15}$$

where $k_0 = \omega/c$. The dispersion relation relating the angular frequency of the field, ω, to the wavevector along the interface is obtained by substituting equation 2.2.14 into equation 2.2.15

$$k_{\mathrm{SPP}} = k_x = k_0\sqrt{\frac{\epsilon_1\epsilon_2}{\epsilon_1 + \epsilon_2}}. \tag{2.2.16}$$

2.2.2 The Properties of Surface Plasmon Polaritons on Planar Surfaces

The response of a metal is characterised by its frequency-dependent permittivity or 'dielectric function'. Hence equation 2.2.16 becomes

$$k_{\mathrm{SPP}} = k_x = k_0\sqrt{\frac{\epsilon_1\epsilon_2(\omega)}{\epsilon_1 + \epsilon_2(\omega)}}, \tag{2.2.17}$$

where $\epsilon_2(\omega)$ is the frequency-dependent dielectric function of the metal and ϵ_1 is the permittivity of the bounding non-conducting media. The permittivity of the metal $\epsilon_2(\omega)$ can be approximated by the Drude model [19] for the free electron gas as shown in the following expression

$$\epsilon_2(\omega) = 1 - \frac{\omega_p^2}{\omega^2 + i\omega\gamma}, \tag{2.2.18}$$

where ω is the angular frequency, γ is the average rate of collision of free electrons with the lattice, and ω_p is the natural frequency of the bulk conducting electrons, i.e. the 'plasma frequency.' The bulk plasma frequency for metals typically occurs in the ultraviolet part of the spectrum, below which the permittivity is negative.

Using the Drude model to examine the frequency-dependence of the real (ϵ') and imaginary (ϵ'') parts of the permittivity [20] for the metal, it can be seen that the negative real part of the permittivity increases with wavelength. Whilst at visible frequencies, both the real and imaginary part of the permittivity are small, both increase (the negative real part and the positive imaginary part) through the THz frequencies to approach $\sim 10^4$ for the real part and increasing to $\sim 10^9$ for the imaginary part at

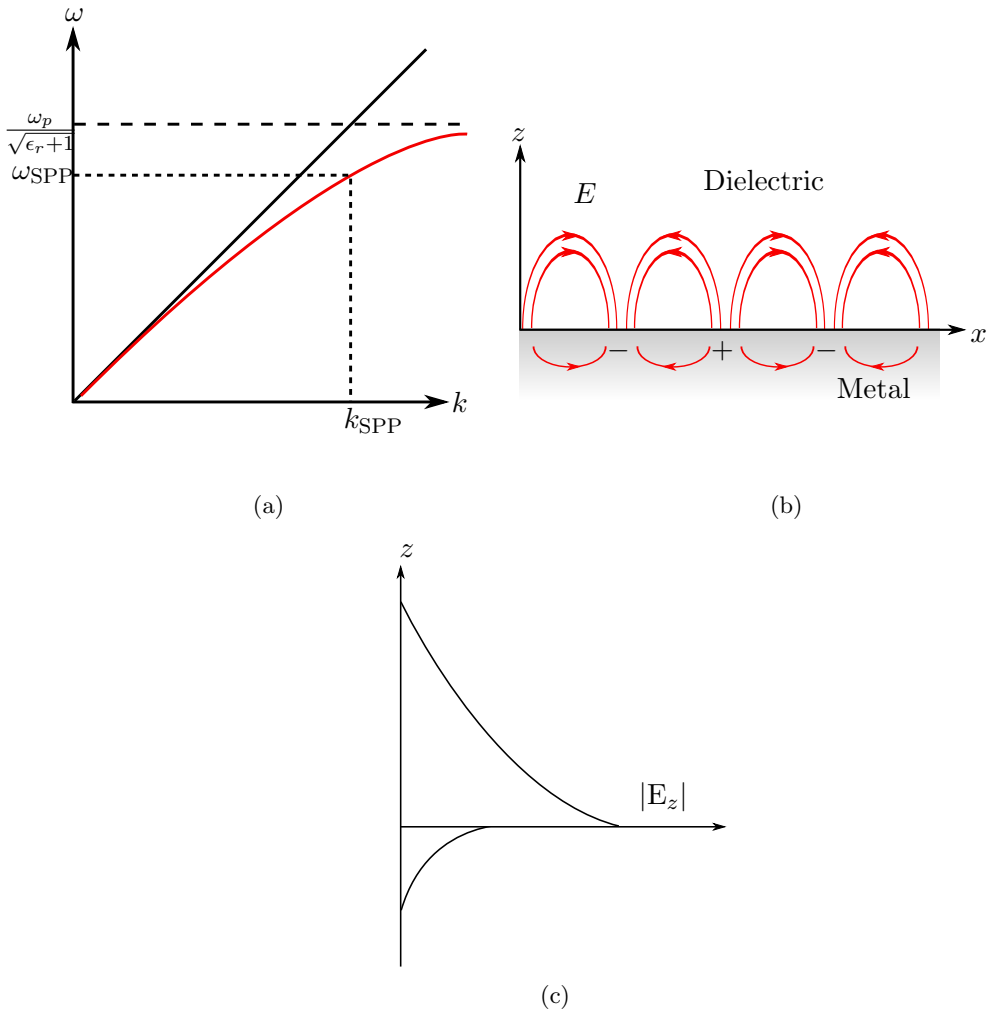

Figure 2.2: (a) Schematic representation of the dispersion curve of a SPP (red line), supported at the interface between air and a Drude-like metal, illustrating the nature of the mode as a function of angular frequency (ω) and in-plane momentum (k_x) parallel to the interface at which the surface wave propagates. (b) Schematic representation of the electric field vectors of a SPP at the interface between a Drude-like metal and a dielectric. (c) The exponential decay of the E_z component away from the surface.

microwave frequencies.

Substituting equation 2.2.18 into equation 2.2.17 yields the dispersion relation for a SPP, a schematic representation of which is shown in Figure 2.2 (a). Assuming the dielectric medium is air, the frequency at which the real part of the dielectric function of the metal is equal but opposite in sign to the real part of the dielectric function of the dielectric, occurs when the limiting frequency of the dispersion of the mode is obtained, i.e. the surface plasma frequency at $\omega_{\mathrm{SPP}} = \omega_p/\sqrt{\epsilon_r + 1}$ (where ω_p is the bulk plasma frequency of the material). The dispersion of the SPP closely follows the light line at low frequencies and is said to be 'photon' like, i.e. it mimics the behaviour of a grazing

photon, whilst at higher frequencies it asymptotically approaches its limiting frequency defined by ω_{SPP}. Note the light line is actually at light cone, a slice through which has been shown in Figure 2.2.

Since $k_{\mathrm{SPP}} > k_0$ (as illustrated in Fig. 2.2 (a)) to couple radiation to this surface oscillation additional momentum is required. A general review of momentum matching techniques can be found in Ref [1]. Additionally, grating coupling to surface waves will be discussed in more detail in Section 2.2.3 of this thesis.

The permittivity of the metal can be related to the real (σ') and imaginary (σ'') parts of the conductivity via the following equations

$$\sigma^{'} = \omega\epsilon_0\epsilon^{''}, \tag{2.2.19}$$

$$\sigma^{''} = \omega\epsilon_0(\epsilon^{'} - 1). \tag{2.2.20}$$

From equations 2.2.19 and 2.2.20, it can be seen that the real part of the conductivity is large (positive) at microwave frequencies, whilst the imaginary part is almost zero, hence metals can be approximated as near-perfect electrical conductors (PEC) in this regime.

2.2.2.1 Penetration Depth

The fields associated with a SPP excited at the interface between a dielectric and metal will decay exponentially away from the surface into both bounding media. A useful measure of this decay is the skin depth, L_z, defined as the distance at which the amplitude of the field has decayed to 1/e of its maximum value at the surface.

It has been shown that the momentum of the SPP is greater then the maximum available momentum from an incident photon. From equation 2.2.15 therefore it can be concluded that k_{zm} for SPPs must be purely imaginary. Substituting equation 2.2.16 in to equation 2.2.15 yields the following expression for k_z

$$k_{zm} = \pm k_0 \sqrt{\frac{\epsilon_m^2}{\epsilon_1 + \epsilon_2}}, \tag{2.2.21}$$

where the subscript m denotes the medium in which k_{zm} is being determined ($m = 1, 2$).

This expression may be simplified for the case under consideration with medium $m = 1$ being a non-absorbing dielectric, $\mathrm{Re}(\epsilon_1) > 0$ and $\mathrm{Im}(\epsilon_1) = 0$, and medium $m = 2$ a lossy metal, $\mathrm{Re}(\epsilon_2) < 0$ and $\mathrm{Im}(\epsilon_2) > 0$. In the case where the metal is highly conducting we also have the considerations $|\mathrm{Re}(\epsilon_2)| >> 1$ and $|\mathrm{Re}(\epsilon_2)| >> \mathrm{Im}(\epsilon_2)$. Under these conditions, equation 2.2.21 simplifies to,

$$k_{zm} = \pm k_0 \sqrt{\frac{\mathrm{Re}(\epsilon_m)^2}{\mathrm{Re}(\epsilon_2)}}. \tag{2.2.22}$$

The penetration depth is then given by:

$$L_{zm} = 1/k_{zm} = \frac{\lambda_0}{2\pi} \sqrt{\frac{|\mathrm{Re}(\epsilon_2)|}{|\mathrm{Re}(\epsilon_m)^2|}}. \tag{2.2.23}$$

The field at the surface, and this associated exponential decay of the SPP fields in the z direction, is shown schematically in Figure 2.2 (b) and (c) for an SPP in the visible regime. In the limit of $\epsilon_2 \to \infty$, i.e. a perfect metal, equation 2.2.23 shows that the penetration depth into the dielectric becomes infinite, and penetration into the metal becomes zero. As such, at microwave frequencies, there is no localisation of the fields at the interface between the metal and dielectric, therefore the surface mode resembles a grazing photon.

2.2.2.2 Propagation Length

The propagation length of the SPP along the surface is defined in a similar manner to the penetration depth of the SPP into the bounding media, as in the previous section. The propagation length is defined as the length at which the field intensity falls to $1/e$ of its maximum value. The imaginary part of k_x is given by:

$$\mathrm{Im}(k_x) = \frac{k_0 \,\mathrm{Im}(\epsilon_2)}{2\mathrm{Re}(\epsilon_2)^2} \left(\frac{\epsilon_1 \mathrm{Re}(\epsilon_2)}{\epsilon_1 + \mathrm{Re}(\epsilon_2)} \right)^{3/2}. \tag{2.2.24}$$

The propagation length, L_x is given by:

$$L_x = \lambda_0 \frac{\mathrm{Re}(\epsilon_2)^2}{2\pi \mathrm{Im}(\epsilon_2)} \left(\frac{\epsilon_1 + \mathrm{Re}(\epsilon_2)}{\epsilon_1 \mathrm{Re}(\epsilon_2)} \right)^{3/2}. \tag{2.2.25}$$

2.2.3 Grating Coupling to Surface Waves

Direct coupling of free space radiation to a SPP on a planar surface is not possible due to the momentum mismatch between an incident photon and that of the mode i.e. $k_{\mathrm{SPP}} > k_0$. In this section, grating coupling to surface modes supported by periodic structures will be presented. Whilst only scattering from a singularly periodic structure will be discussed, the concept is easily extended to include the effect of a dual period grating, a full discussion of which is presented in Chapter 6 of this thesis, and in Refs. [21–23].

A schematic representation of the periodic structure, the scattering of radiation from which is discussed in this section, is shown in Figure 2.3. The polar angle (θ) of an incident wave is measured from the normal (dotted line) to the plane of the grating,

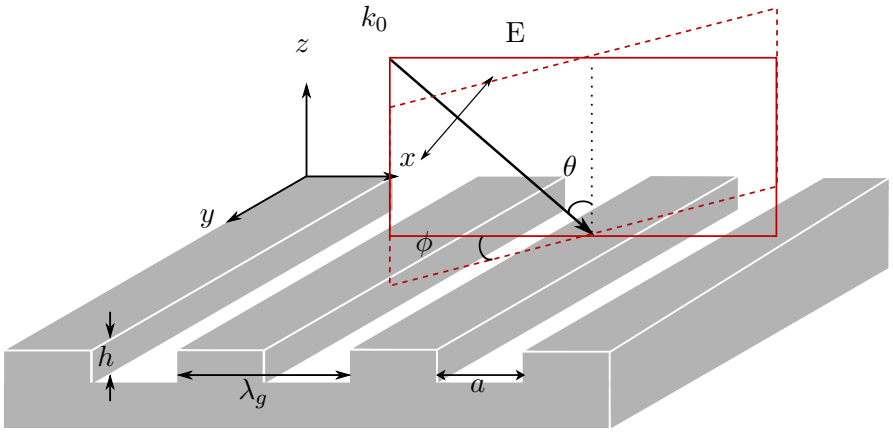

Figure 2.3: A schematic representation of the periodic structure (of pitch λ_g) under consideration, were h defines the depth of the grooves. The co-ordinate system is also shown.

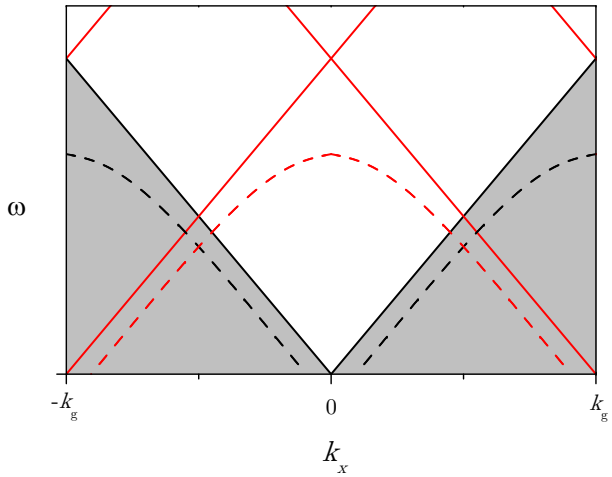

Figure 2.4: The surface wave dispersion curve for a periodic structure of pitch λ_g. The solid and dashed black lines represent the non-diffracted light lines and surface wave dispersion, respectively. The solid and dashed red lines represent the light lines and surface wave dispersion curve scattered from $\pm k_g$.

whilst the azimuthal angle (ϕ) is defined between the plane of incidence and the grating vector. The polarisation of the incident radiation is defined with respect to the plane of incidence; when the electric vector of the incident radiation is contained within the plane of incidence (i.e. the plane containing in the incident wavevector), the wave is described as being p-polarised or transverse magnetic (TM), whilst a s-polarised or transverse electric (TE) wave is characterised by an electric vector perpendicular to the plane of incidence.

The mechanism for diffractive coupling to surface modes supported by the periodic structure can best be understood by considering the effect that the corrugation has on

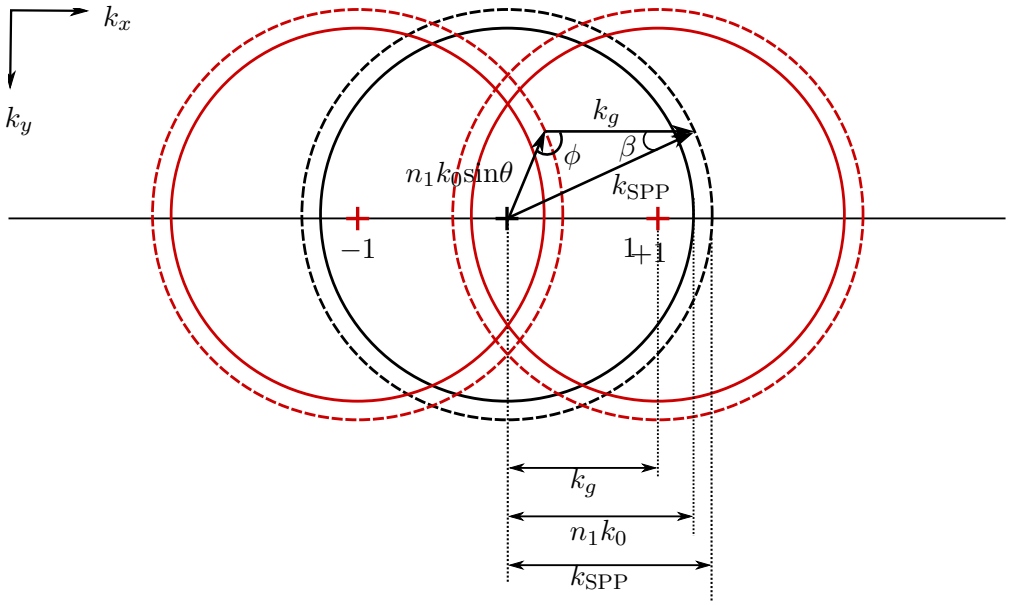

Figure 2.5: A two dimensional representation in reciprocal space of the surface modes and light circles produced by a periodically textured surface. The solid and dashed black lines represent the maximum momentum available to an incident photon, and the dispersion of the non-diffracted surface mode, respectively. The solid and dashed red lines represent the diffracted light circles and surface wave dispersion scattered from $\pm k_g$. The arrows represent the coupling between a photon incident at polar angle θ and azimuthal angle ϕ to a surface wave that propagates at angle β to the grooves of the grating (reproduced from [1]).

the dispersion of the surface mode. A schematic representation of which is shown in Fig. 2.4 for when the plane of incidence contains the grating vector (i.e. $\phi = 0°$). The light lines (solid black lines) represent the maximum momentum available to an incident photon, and the low wavevector region which they bound (non-shaded region Fig. 2.4) is commonly referred to as the 'radiative region'. The radiative region is one in which freely propagating radiation can directly couple to modes supported in this region, i.e. modes in this region may be radiatively coupled to, or may radiatively decay. However, as discussed previously, the momentum of a SPP supported at optical frequencies at the interface between a metal and dielectric, is greater than that of an incident photon ($k_{\mathrm{SPP}} > k_0$), the dispersion of which is represented by the black dashed lines in Fig. 6.11. This lies to the high wavevector side of the light line in the 'non-radiative' region i.e. one in which freely propagating radiation cannot directly couple to modes supported in this region (shaded region Fig. 6.11).

The periodicity of the surface allows scattering of the incident light in a direction normal to the surface modulation at integer numbers of the grating vector $\mathbf{k}_g$ (where $\mathbf{k}_g = 2\pi/\lambda_g$ and λ_g is the pitch of the grating). These scattered waves are the diffracted orders produced by the surface. If the momentum of a diffracted order is greater than the

maximum allowed momentum in the incident medium, the order will not propagate and instead will become evanescent. The evanescent fields have greater in-plane momentum than the incident photons and are able to excite the surface modes beyond the light line, giving the following condition when the grating is in classical mount (i.e. $\phi = 0°$):

$$k_{\mathrm{SPP}} = nk_0 \sin\theta \pm Nk_g, \tag{2.2.26}$$

where $\mathbf{k}_{\mathrm{SPP}}$ is the wavevector of the surface mode, θ is the angle of incidence as defined previously, hence $k_0 \sin\theta$ is the in-plane wavevector of the incident light, n is the refractive index of the incident medium and N is an integer.

The periodicity of the structure can be represented by a line of points in reciprocal space (Fig. 6.11), the spacing between which is governed by the grating wavevector $\mathbf{k}_g$. The surface mode and light lines are scattered from the series of points representing integer numbers of the grating vector. The surface modes and light lines scattered from $\pm k_g$ are represented by the dashed and solid red lines respectively. Since the dispersion curve of the scattered surface mode (red dashed line) lies to the low wavevector side of the light line, the surface mode may be directly radiatively coupled to by incident radiation.

Unlike for the surface mode supported by a planar system, the periodic structure in the x-direction breaks the symmetry, and the dispersion of the mode is no longer identical in all directions of reciprocal space. However, radiation incident at non-zero azimuthal angles can still be coupled to by diffraction caused by scattering from the periodicity in the x-direction. For azimuthal angles other than $\phi = 0°$, $\mathbf{k}_{\mathrm{SPP}}$, $\mathbf{k}_0$ and $\mathbf{k}_g$ are no longer co-linear. The momentum matching condition becomes

$$k_{\mathrm{SPP}}^2 - k_g^2 = k_0^2 \sin^2\theta - 2k_0 k_g \sin\theta \cos\phi. \tag{2.2.27}$$

Schematically this is represented in Fig. 2.5, which shows a slice through the dispersion curve in the $k_x - k_y$ plane for a constant ω. The solid black circle, of radius $n_1 k_0$, represents the maximum momentum available to an incident photon, whilst the dashed black line, defining a circle of radius k_{SPP}, is indicative of the momentum of the surface mode. Since $k_{\mathrm{SPP}} > n_1 k_0$, radiative coupling to the surface mode can not be achieved. The solid and red curves, centred at $\pm k_g$ represent the scattered light circle and surface mode respectively. The scattered surface mode now lies within the radiative region (white region bounded by the circle with solid black outline) and can be coupled to by incident radiation.

Note however, an important consequence of using a periodic grating is that for azimuthal angles between 0° and 90°, both TM and TE polarised radiation can excite a surface wave as it is possible for both polarisations to have a component of the electric

vector normal to the interface.

2.2.3.1 Band Gaps

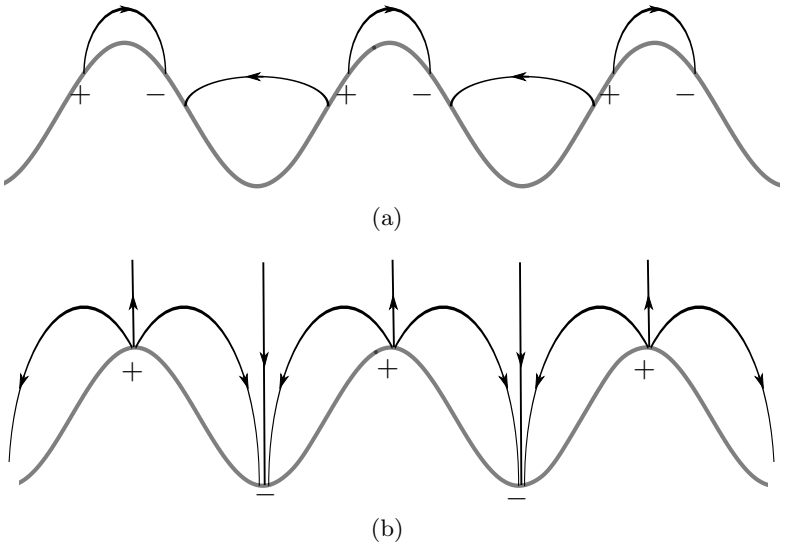

Figure 2.6: Schematic representation of standing wave field solution for (a) low frequency solution and (b) high frequency solution on a sinusoidal gratings. The field lines in (b) are more distorted therefore correspond to the higher energy mode.

Analogous to the electron standing waves formed at Brillouin zone boundaries or vibrational modes of a solid rod, a corrugated metallic surface can support SPP standing waves [24, 25]. Consider a SPP propagating on a corrugated surface with the direction of propagation being normal to the grooves; when the SPP encounters a counter-propagating SPP with equal energy but equal and opposite momentum, two different SPP standing waves typically occur, the nodes and anti-nodes of which are shifted spatially by $\lambda/4$ in space with respect to each other.

An example of the field distributions of the two different standing wave solutions of period λ_g is shown in Fig. 2.6. The field lines are more distorted in Fig. 2.6 (b) with respect to those in Fig. 2.6 (a), therefore Fig. 2.6 (b) corresponds to the higher energy solution and Fig. 2.6 (a) the lower energy solution. Due to the different field distributions (energies) of the two standing wave solutions, an energy band in which the propagation of surface waves is forbidden will open up in the dispersion relation of the modes, whenever two modes intersect, i.e. every $k_g/2$. The size of the band gap is determined by the grating profile and curvature of the modes dispersion. A purely sinusoidal grating that has no higher order harmonics (i.e. second periodicity) will still exhibit a band gap at $k_x = 0$, however the gap will be much smaller because the process requires two consecutive k_g scattering events which is less probable than a single $2k_g$

scatter. Further discussion of band gaps in the dispersion of surface waves is presented in Chapter 4, Chapter 5 and Chapter 6).

2.3 'Spoof' Surface Plasmons

As discussed previously, in the low frequency limit metals behave as near perfect conductors and an air/metal interface cannot support a mode with a dispersion of the plasma form. Adding subwavelength texture to a near-perfect conductor can greatly alter the electromagnetic boundary conditions at the surface, to the extent that a bound surface mode can be supported even in the limit where the PEC condition is assumed to be valid. This concept was first extensively studied in the 1950s by Barlow and Cullen [9] and later by Cutler [12]. More recently Pendry, and his co-workers [3, 4] opened up the field of plasmonics to the low frequency domain, proposing that a perforated surface of a highly conducting substrate can support surface plasmon polariton (SPP)-like modes. The 2D version of which is similar to, but much thicker than, that analysed by Ulrich and Tacke [13] in earlier work, with the addition of a lossless dielectric material inside the cavities which acts to reduce the cutoff frequency for light propagating in the holes.

The field of 'spoof' or 'designer' surface plasmons has advanced significantly since Pendry's original proposal, with the first experimental verification of the concept at microwave [2] and terahertz [26] frequencies soon following. The early studies analysing spoof SPPs considered simple planar geometries [4–6, 27–31], with more complex waveguiding schemes exploiting these surface EM modes being subsequentially proposed theoretically [32–36]and realised experimentally [37–47]. In the aforementioned studies, the design of the structures is such that deep subwavelength transverse confinement of microwaves or THz are observed, whilst long propagation distances are maintained; modal characteristics unobtainable using untextured structures at these wavelengths. More recently the spoof plasmon concept has been proposed as a route to achieve directional beaming [48], broadband transparency [49] and nonreciprocal transmission of EM radiation [50].

2.3.1 Effective Surface Plasma Frequency

In the limit of the incident radiation being insensitive to the details of the structure, the structured layer can be described using an effective medium approximation; the layer is assigned an effective permittivity ϵ_{eff} [51, 52]. The effective frequency-dependent dielectric function behaves as a metal described by a Drude-like response with a significantly reduced plasma frequency. The limiting frequency of these geometrically-induced surface modes is often referred to as the 'effective surface plasma' frequency. In the effective medium picture, an evanescent field penetrates into the structured material,

i.e. the voids or hollows of the structure, thus creating an effective penetration depth, binding the mode to the surface of the structure. The effective medium approximation of the response of a 1D array of grooves, Sievenpiper 'mushroom' structure, and 2D array of holes will be discussed in Sections 2.3.2, 2.3.3 and 2.3.4 respectively.

2.3.2 1D Array of Grooves

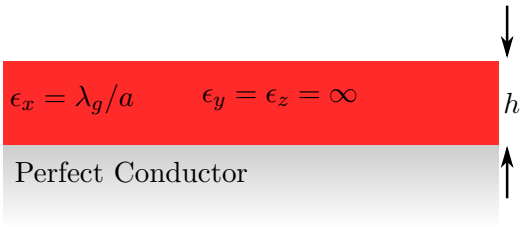

Figure 2.7: In the effective medium approximation, the structure displayed in 2.3 behaves as a homogeneous but anisotropic layer of thickness h on top of a perfect conductor.

Firstly consider a one-dimensional array of grooves (Fig. 2.3), of width a, depth h and periodicity λ_g. Using the effective medium description, the dispersion relation can be obtained by approximating the array of grooves as a homogeneous but anisotropic layer of thickness h on the top surface of a perfect conductor (Fig. 2.7) [4]. The homogeneous layer has the following parameters:

$$\epsilon_x = \frac{\lambda_g}{a}, \quad \epsilon_y = \epsilon_z = \infty \tag{2.3.1}$$

where ϵ_x, ϵ_y and ϵ_z are the permittivities in the x, y and z direction respectively. As light propagates in the grooves in the y-or z-direction with the velocity of light,

$$\sqrt{\epsilon_x \mu_y} = \sqrt{\epsilon_x \mu_z} = 1 \tag{2.3.2}$$

and hence,

$$\mu_y = \mu_z = \frac{1}{\epsilon_x} \quad \mu_x = 1, \tag{2.3.3}$$

where ϵ_x, ϵ_y and ϵ_z are the permeabilities in the x, y and z direction respectively. The effective plasma frequency for this 1D structure is given by

$$\omega_{p_{eff}} = \frac{\pi c}{2h}, \tag{2.3.4}$$

where c is the speed of light. Note equation 2.3.4 corresponds to the frequency at which the fundamental cavity waveguide mode in the grooves is supported.

2.3.3 Sievenpiper 'Mushroom' Structure

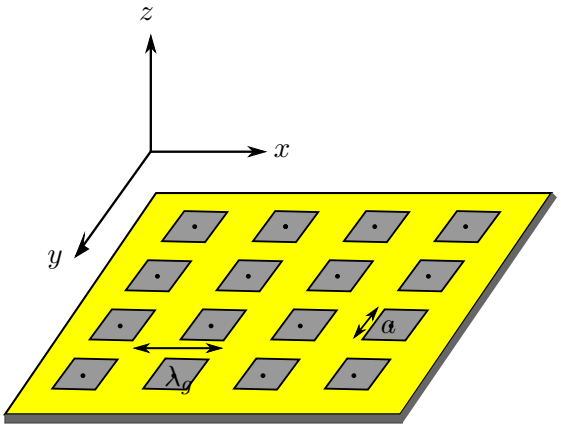

Figure 2.8: A schematic representation of the Sievenpiper 'mushroom' structure. The patches are of length a and the pitch of the structure is λ_g.

Next consider the Sievenpiper 'mushroom' structure [53], i.e. an array of disconnected patches separated from a continuous ground plane by a 'via-array layer' (dielectric slab embedded with an array of pins), a schematic representation of which is shown in Fig. 2.8. Adopting an effective medium approach, Clavijo *et al.* [54] modelled the response of the structure by considering it as a two-layer anisotropic uniaxial material in both permittivity and permeability, with the top layer representing the array of patches and the bottom layer the via array substrate. It was shown that the via array layer is highly anisotropic; the effective permittivity in the direction normal to the surface (ϵ_z) is given by:

$$\epsilon_z(\omega) = \epsilon_D - \frac{1}{\omega^2 \epsilon_0 \frac{\mu_D \mu_0 A}{4\pi} [\mathrm{In}\frac{1}{\alpha} + \alpha - 1]}, \tag{2.3.5}$$

where ϵ_D and μ_D are the permittivity and permeability of the host medium and ϵ_0 and μ_0 are the permittivity and permeability of free space, A is the area of the patches and α is the ratio of the via's cross-sectional area to the unit cell. It is characterised by a Drude-like dispersion with a negative real part up to a cutoff 'plasma' frequency, in other words ϵ_z exhibits a 'plasmonic'-like response.

The transverse permittivity of the via array layers is given by the 2D Clausius-Mossotti equation

$$\epsilon_x = \epsilon_y = \epsilon_D = \left(\frac{1+\alpha}{1-\alpha}\right). \tag{2.3.6}$$

With the transverse permeabilities given by

$$\mu_x = \mu_y = \left(\frac{\epsilon_D}{\epsilon_x}\right)\mu_D. \tag{2.3.7}$$

2.3.4 2D Array of Holes

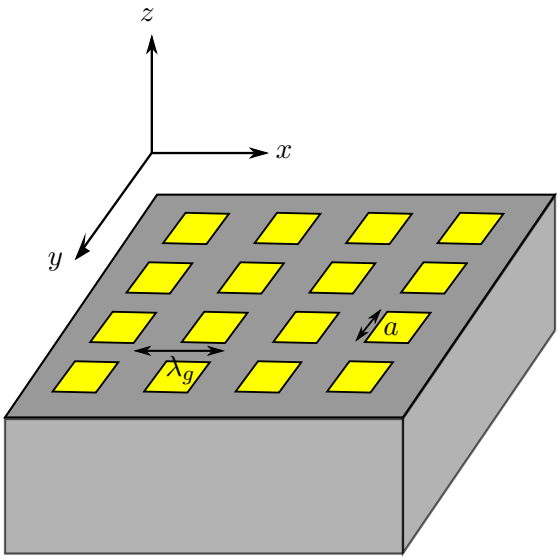

Figure 2.9: A two-dimensional square array ($\lambda_g \times \lambda_g$) of square holes (side a) perforated on a semi-infinite perfect conductor.

In this section it will be shown that a near-perfectly conducting substrate pierced by a 2D array of subwavelength holes (a schematic representation of which is shown in Figure 2.9) can support a bound SPP-like mode. The array of holes can be considered as equivalent to an array of waveguides. The confinement of electromagnetic waves in a hollow pipe or waveguide will result in series of modes supported from the quantisation of the EM fields within the geometry, a full description of which can be found in Ref. [55].

Three different types of waves can be supported by a waveguide of arbitrary cross-section. They are categorised by their axial (longitudinal) and transverse field compo-

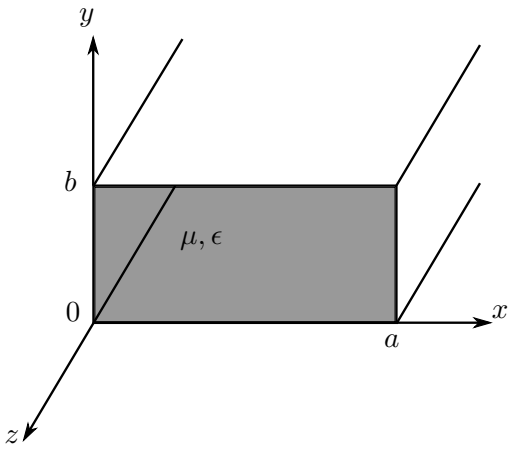

Figure 2.10: Geometry of rectangular waveguide.

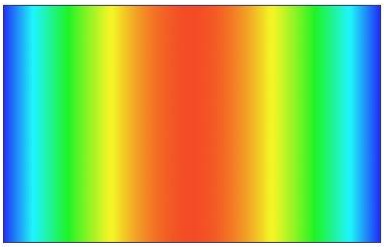

Figure 2.11: Electric field profile plotted in the xy-plane of the eigensolutions associated with the TE_{10} mode supported by an air filled perfectly conducting metal waveguide, with uniform rectangular cross-section and infinite in the z-direction. Red and blue regions correspond to high and zero field magnitude respectively.

nents. Considering z to be in the propagation direction, TE (transverse electric) waves are supported by the waveguide when $E_z = 0$ ($H_z \neq 0$), i.e. when there is no longitudinal component of the electrical field but there is of the magnetic field. Further TM (transverse magnetic) waves are characterised by $H_z = 0$ ($E_z \neq 0$), i.e. the magnetic field is entirely in the transverse direction, no longitudinal magnetic field component exists. Finally if both E_z and $H_z = 0$, that is the magnetic and electric fields are entirely transverse, transverse electro magnetic (TEM) waves can be supported.

The response of the hole array structures discussed in Chapters 4, 5 and 6 of this thesis, will in general be investigated at frequencies close to where the dominant (lowest order) waveguide mode is supported by holes. This mode is transverse electric in type. For holes of infinite depth, at frequencies below the dominant waveguide mode, only evanescent modes are supported by the guide, which is precisely the condition that is required to support a bound surface mode.

Whilst each hole array discussed in this thesis will comprise holes of different geometries, as an example, the conditions for which a waveguide of rectangular cross-section of side length $a \times b$ (Fig. 2.10) supports an evanescent and a propagating mode is discussed below. The guide is formed from PEC and assumed to be filled with a material of permittivity ϵ and permeability μ. Note that $a > b$.

The propagation constant for a TE mode supported by this geometry is

$$k_z = \sqrt{k_0^2 - k_c^2} = \sqrt{k_0^2 - \left(\frac{m\pi}{a}\right)^2 - \left(\frac{n\pi}{b}\right)^2}, \tag{2.3.8}$$

where m and n are integer numbers which represent the mode number, i.e. the number of quantisations in the x and y directions, $k_0 = 2\pi/\lambda_0$, and k_c is the cutoff wavenumber. Equation 2.3.8 is real, corresponding to a propagating mode, when

$$k_0 > k_c = \sqrt{\left(\frac{m\pi}{a}\right)^2 + \left(\frac{n\pi}{b}\right)^2}. \tag{2.3.9}$$

Each mode supported by the guide (i.e. each combination of m and n) has a cutoff frequency $f_{c_{mn}}$ given by

$$f_{c_{mn}} = \frac{1}{2\pi\sqrt{\mu\epsilon}}\sqrt{\left(\frac{m\pi}{a}\right)^2 - \left(\frac{n\pi}{b}\right)^2}. \tag{2.3.10}$$

The mode with the lowest cutoff frequency is called the dominant or fundamental mode. Since $a > b$, the lowest order cutoff frequency occurs for the TE_{10} ($m = 1$, $n = 0$) mode;

$$f_{c_{10}} = \frac{1}{2a\sqrt{\mu\epsilon}}. \tag{2.3.11}$$

The time-averaged electric field profile of the TE_{10} modes is shown in Figure 2.11. Red and blue regions correspond to high and zero field magnitude respectively. For a given frequency, f, only those modes having $f > f_c$ will propagate; modes with $f < f_c$ will lead to an imaginary k_z and the guide will support an evanescent mode. Hence an array of holes (guides) can support a surface mode at frequencies below their fundamental resonance which for an infinitely long guide will be the cutoff frequency of the guide.

For a two-dimensional structure comprised of an array of infinitely deep holes (waveguides), of size a, period λ_g, (Fig. 2.9 (a)) a similar analysis to that discussed for a 1D structure yields the following equations for the effective permittivity and permeabilities [3, 4] in the x and y directions (which are equal due to the symmetry of the structure):

$$\epsilon_{x_{eff}} = \epsilon_{y_{eff}} = \frac{\epsilon_h}{S^2}\left(1 - \frac{\pi^2 c^2}{a^2\epsilon_h\omega^2}\right), \tag{2.3.12}$$

$$\mu_{x_{eff}} = \mu_{y_{eff}} = S^2 \tag{2.3.13}$$

where $S = 2\sqrt{2a}/\pi\lambda_g$ and ϵ_h is the dielectric constant of the material inside the hole.

Since the dispersion of the waveguide mode inside the hole is unaffected by parallel momentum, the permittivity and permeability in the z-direction is given by:

$$\epsilon_{z_{eff}} = \mu_{z_{eff}} = \infty. \tag{2.3.14}$$

The effective plasma frequency for this 2D structure is defined as:

$$\omega_{p_{eff}} = \frac{\pi c}{2a\sqrt{\epsilon_h}}. \tag{2.3.15}$$

Note equation 2.3.15 defines exactly the cutoff frequency of the waveguide that forms the hole as discussed previously.

2.3.4.1 Importance of Diffraction

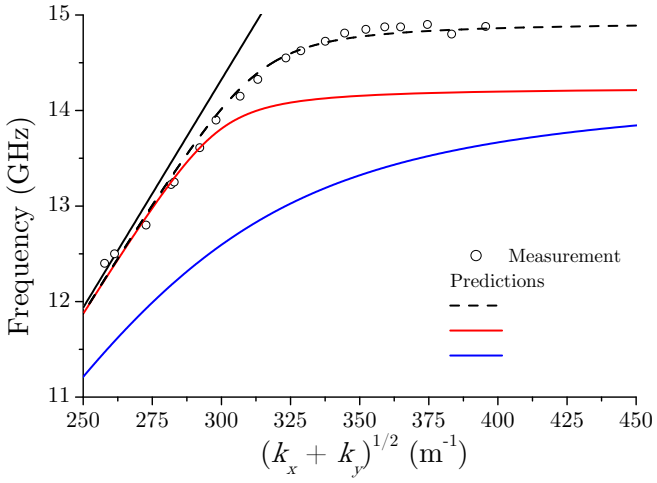

Figure 2.12: Real component of the dispersion relation in the diagonal direction (i.e, $k_y = k_x$) for a sample defined by $a = 6.96$ mm, $\lambda_g = 9.53$mm, with holes of depth 15mm, filled with a dielectric characterised by a relative permittivity of 2.29. The circles represent the dispersion measured in a prism-coupling experiment [2]. The lines represent the dispersion predicted by Pendry *et al.* [3] and Garcia-Vidal *et al.* [4] (blue curve), Garcia de Abajo and Saenz [5] (red curve) and Hendry *et al.* [6] (black dashed curve). Reproduced from [6].

The dispersion relation of the surface waves supported by the structures discussed in Sections 2.3.2, 2.3.3 and 2.3.4 exhibit asymptotic behaviour at frequencies close to the cutoff frequency or 'effective surface plasma frequency'. However the simple models in Refs [3], [4] and [54] neglect the effects of diffraction, leading to a modification of the dispersion curve. Further discussion on considering the effects that the periodicity has on the dispersion of the mode supported by the Sievenpiper structure will be presented in Chapter 7, and by the 2D structure will be discussed below.

A series of studies proceeded Pendry and his co-workers seminal work on 'spoof' or 'designer' surface plasmons [5, 6, 56–58] which provided corrections to Pendry's analytical dispersion equation for the SPP-like mode supported by the array of holes. However it was Hendry's 2008 [6] study which provided an explicit analytical expression relating frequency to in-plane wavevector for an electromagnetic surface mode at the interface between a vacuum and a periodically perforated perfect conductor; the effects of evanescent diffraction and the finite depth of the holes were considered. An expression for the limiting frequency of the surface mode was obtained which accounted for the finite depth

of the hole. Equation 2.3.15 now becomes

$$\omega_{p_{eff}} = \frac{\pi c}{\sqrt{\epsilon_h}} \sqrt{\frac{1}{a^2} + \frac{1}{4h^2}}, \tag{2.3.16}$$

for holes of finite depth (h) terminated by a PEC. Note this equation does not take in to account end effects at the top of the holes. Note a discussion of the limiting frequencies of the surface modes supported by open ended holes can be found in Ref [59].

The findings of Hendry's study [6] is summarised in Figure 2.12, which has been reproduced with the authors permission. Excellent agreement between Hendry's predicted (dashed black line) and the experimentally measured dispersion relation (circles) [2] is shown. Note that the inclusion of higher order waveguide modes [5] generates a dispersion relation (red curve) that is accurate only in the long wavelength limit, whilst when neither the higher order waveguide modes nor evanescent diffraction are considered [3, 4], both the curvature and asymptote of the dispersion of the mode are incorrectly predicted (blue curve). Hence Hendry's study showed that it is invalid to employ an effective medium approach to obtain the dispersion relation of the surface mode supported by a 2D array of holes in a PEC substrate. In other words, simply considering the frequency-dependence of the effective permittivity is not sufficient, the wavevector-dependence of these values is also important, i.e. they are spatially dispersive.

2.4 Conclusions

In this chapter an overview of surface waves supported at the interface between a metal/dielectric boundary has been discussed. It has been shown that surface waves at microwave frequencies, often referred to as 'spoof' or 'designer' surface waves can be supported by periodically textured near-perfectly conducting substrates. The dispersion of these 'spoof' surface waves have a 'plasmonic' form, i.e. the dispersion of the mode asymptotically approaches a limiting frequency at high wavevector. The limiting frequency of these structurally-induced surface waves is dictated by the geometry of the structure. Note that a key difference between surface waves supported at the interface between a metal/dielectric boundary at optical frequencies (SPPs) and surface waves supported by corrugated surfaces at microwave frequencies is as follows; whilst for an 2D array of infinitely deep holes, for frequencies below the cutoff of the holes, the decay of the fields of the surface mode are purely evanescent into the pseudo-plasmonic media (hole array), thus mimicking the behaviour of a SPP. For finite depth holes or grooves however, or indeed for the Sievenpiper structure, this is not the case, since the finite depth of the structure imposes an constraint on the decay of the evanescent fields

associated with the surface mode.

Chapter 3

Experimental Methods and Modelling

3.1 Introduction

In this chapter details of the experimental methods and numerical techniques used to investigate the structures discussed in this thesis are presented. All experimental work has been conducted at microwave frequencies. Free-space measurement techniques are employed to record the transmission through and reflection from the structures discussed in Chapters 6 and 4 respectively, details of which can be found in Sections 3.2.1.2 and 3.2.1.3 respectively, whilst details of the blade-coupling and free-space measurement technique utilised in Chapters 5 and 7 can be found in Section 3.2.3. Methods for sample fabrication will be presented in Section 3.3. Finally, a brief overview of the numerically modelling techniques used to produce the majority of the modelling results presented within this thesis, is discussed in Section 3.4.

3.2 Experimental Measurement Techniques

3.2.1 Free-Space Measurements

Free-space measurement techniques have been used in this thesis to obtain the reflection intensity from, and transmission intensity through structures as a function of incident angle and frequency (wavelength). A schematic representation of the typical experimental arrangements for conducting transmission and reflection experiments is shown in Figures 3.1 and 3.2, respectively. Note that these experiments have been conducted within a large laboratory, as such there is no requirement for them to be housed in an anechoic chamber since the nearest reflecting boundary is $> 50\lambda$ from the experimental setup (where λ is the longest operating wavelength). Specific details of the setup for performing transmission and reflection measurements can be found in Sections 3.2.1.2

and 3.2.1.3, respectively. First however, a description of the apparatus common to both experimental arrangements is presented.

3.2.1.1 Experimental Apparatus for Free Space Measurement Techniques

Microwave radiation, generated by a combined source and swept frequency oscillator (*Agilent PSG CW Signal Generator E8247C*) is fed via a waveguide coaxial adaptor through a directional waveguide coupler. The waveguide coupler splits the signal; a portion of the signal is fed to a waveguide crystal detector which transmits an electrical signal to the scalar network analyser (SNA) (*Agilent 8757 D*), this is the reference signal. The other portion of the signal is fed to a horn, from which, the signal is emitted into free space. The horn is placed at the focal point of a 4 m radius of curvature spherical mirror (physical radius 22cm), thus producing a plane wave (in the assumption that the horn is acting as a point source). The specular reflected (transmitted) beam from (through) the sample is collected by a second spherical mirror and focused into a second horn, which is also connected to a waveguide-crystal detector. The microwave signal collected by the horn is converted into an electrical signal by the crystal detector and transmitted to the SNA as the detected signal. The sample can be placed on a computer controlled stepper motor driven rotating table, in order to vary the azimuthal (ϕ) and polar (θ) angle (dependent on whether the apparatus is set-up for transmission or reflection measurements). The spectrum analyser and the table are interfaced with a PC via a *LabView* programme.

The mirrors are mounted in wooden frames that lie between a pair of parallel wooden tracks which extend the length of the wooden bench upon which the experimental setup is constructed upon (Fig. 3.1 and Fig. 3.2). This allows for the angle and position of the mirrors, relative to other experimental apparatus to be easily changed. Square pyramidal and planar graded carbon loaded foam acts as a good absorber and can be used to reduce undesirable reflections within the system. The foam is used as an aperture in front of the sample in the transmission experiments to help reduce, particularly at high polar (θ) angles, possible interference effects due to the edge of the sample, since the size of the beam and sample are comparable. To further minimise the size of the beam spot on the sample, absorber can be placed on the 'source' mirror i.e. the mirror upon which the radiation is incident.

The polarisation of the wave emitted through the waveguide horns is dependent on the orientation of the dipole at the back of the horn. Therefore the polarisation of the incident beam can simply be changed by rotating the orientation of the waveguide horn apparatus, a trivial task since they are mounted together. R_{pp}, R_{ss}, R_{ps} and R_{sp}, i.e. the reflection intensities, and the equivalent transmission intensity measurements can be obtained, where the subscript corresponds to the polarisation of the incident and

detected polarisations respectively.

Two type of horns have been used. Standard gain 'narrow band' horns operate at frequency ranges split into European waveguide bands [60], whereas the broadband horns (*Flann DP241-AC*) operate over a much larger frequency range, strictly from $18 - 50$ GHz, but experimentation has shown them to operate successfully down to 8 GHz. Advantageously, it is possible to complete an experiment without changing the horns (five different sets of standard gain horns would be required to cover the frequency range $18 - 50$ GHz,) thus avoiding the possibility of discontinuities in the data. Further the broadband horns contain two coaxial ports, so to change the polarisation of the wave emitted from the horn, the coaxial cable and crystal detector is simply switched from one port to the other one. However, there is a compromise in performance, when compared to using the broadband horns, arising from two factors; firstly, it is not possible to take a reference from the source waveguide horn antenna, since it it not connected to a waveguide coupler. Therefore it is not possible to account for fluctuations in power from the source. Secondly, the broadband horns are not optimised for all frequencies at which they operate, a larger loss in the system with respect to that obtained using standard gain horns is observed, resulting in an increase in the required power.

3.2.1.2 Transmission Experiment Setup

A schematic representation of the setup for transmission experiments is shown in Figure 3.1 (a). As can be seen, the centre of the mirrors align with the centre of the sample and an aperture formed from microwave absorbing material is placed in front of the sample. The horns are placed at the focal point of the mirrors which are tilted such that the beam propagates parallel to the bench. The sample is placed on a computer-controlled rotating table such that a variation in the incident angle (θ) can be easily achieved. From this, by scanning the frequency (wavelength), variation of the magnitude of the in-plane wavevector at the surface of the sample is possible. A variation in ϕ is achieved by manually rotating the sample and securing within a wooden holder.

Figure 3.1 (b) defines the orientation and co-ordinate system used to describe the system. The polarisation of the incident field must be defined. When the electric vector of the incident field is contained in the xz-plane, the field is TM (or p-) polarised. Whilst a TE polarised wave is defined by an electric vector perpendicular to the xz-plane.

3.2.1.3 Reflection Experiment Setup

A schematic representation of the setup for reflection experiments is shown in Figure 3.2. For reflection experiments the sample is placed on a computer controlled rotating table which allows the azimuthal (ϕ) to be easily changed. The position of the mirrors

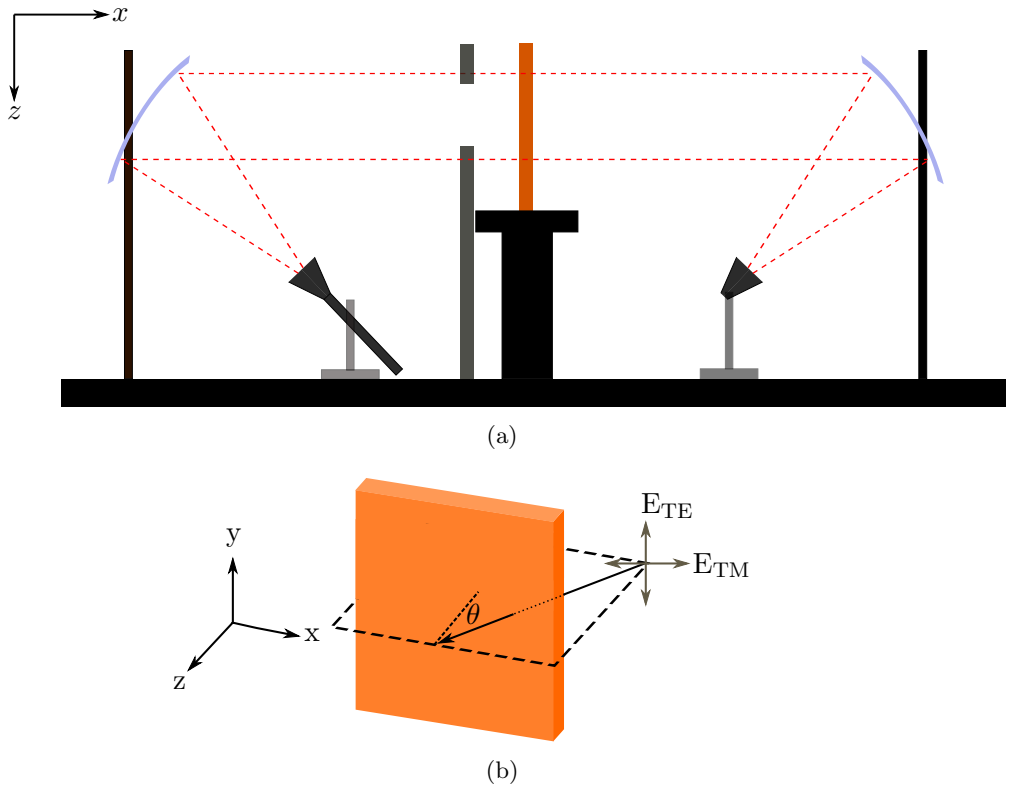

Figure 3.1: (a) Schematic representation of the experimental arrangement for transmission at normal incidence, where the emitter is on the left, and the detector on the right. (b) Diagram showing the direction of the electric field vector to define TE and TM polarised radiation when the sample is rotated by θ.

determine the angle of incidence, θ, which is measured from the normal of the sample.

3.2.1.4 Recording Measurements

Details of the process whereby the measurements are recorded are as follows. The SNA measures the received reference and transmitted signal on a logarithmic scale. The detected signal corresponds to the signal received by the detecting waveguide horn, whilst the reference signal is measured at the emitter as described previously. The detected signal is normalised by the SNA using the reference signal, hence removing the effect of power fluctuation from the source.

Each set of measurements recorded from a sample are required to be normalised against a reference sample, in order to obtain absolute transmission and reflection values. For transmission measurements, the recorded transmission through the sample is normalised against free space (i.e. no sample in the setup). Normalised values of $< 100\%$ for a test sample are indicative of loss in the system. For reflection experiments, the reflection from the experimental sample is normalised against a flat metallic plate, which

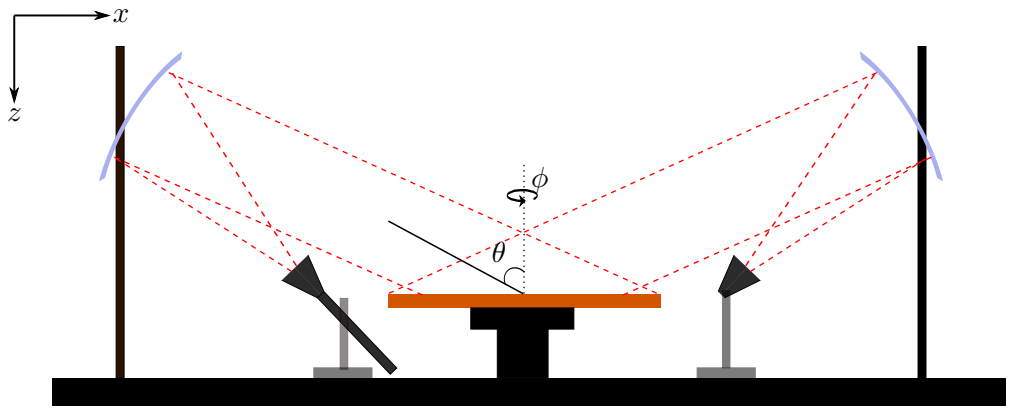

Figure 3.2: Schematic representation of the experimental arrangement for reflection experiments, where the emitter is on the left, and the detector on the right.

will reflect 100% of the incident beam.

Values for the absolute normalised transmission and reflection coefficient (T and R in decibels (dBs)) respectively are obtained using equations 3.2.1 and 3.2.2 respectively,

$$T = 10^{\frac{\Delta t}{10}} \tag{3.2.1}$$

$$R = 10^{\frac{\Delta r}{10}} \tag{3.2.2}$$

where Δt and Δr are the difference between the 'reference' signal and the transmission and reflection signal, respectively.

3.2.2 Vector Network Analyser (VNA)

A Vector Network Analyser (VNA) can be used to measure the magnitude and phase characteristics of for instance, networks, amplifiers, components, cables and antennas. The *VectorStar MS4640A* VNA has been used to record the phase information associated with the surface modes supported by the structures discussed in Chapter 5 and 7 of this thesis. From this information the dispersion of the modes can been obtained (as discussed in the following Section). When only measurement of the intensity of the signal is required, as in Chapter 4 and 6 of this thesis, a Scalar Network Analyser (SNA) has been used, as discussed in Section 3.2.1.1. In the VNA, the coupler providing the reference signal and crystal detectors are incorporated in the assembly of the instrument and therefore no external coupler or crystal detectors are required [61].

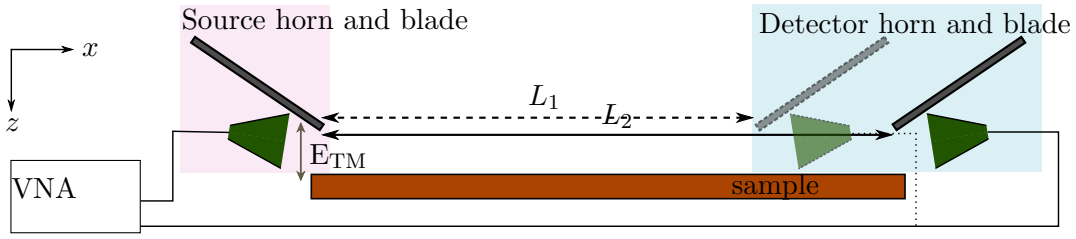

(a)

Figure 3.3: Schematic representation of the blade-coupling set up.

3.2.3 Blade-coupling techniques and Phase-resolved measurements

As discussed in Chapter 2, a suitable mechanism for wavevector matching to free space radiation is required for the excitation of the non-radiative surface modes. One simply method, as used in Chapters 5 and 7, is edge or blade coupling through a subwavelength gap between a perpendicular screen (blade) and the planar surface. This technique was first extensively used by the Terahertz community, for instance in the generation of surface modes by coupling THz radiation into thin dielectric films [62], and to investigate subwavelength confinement of electromagnetic energy using a patterned perfect conductor substrate [63]. This geometry leads to scattering of incident radiation and the generation of evanescent waves comprising a continuum of wave vectors, with the outcoupling from the surface mode performed by an equivalent second blade. Combined with phase resolved measurements (recorded using the VNA), this technique allows for the direct measurement of the dispersion of the supported surface waves in the non-radiative regime.

Radiation emitted from a microwave horn (which is connected to port 1 of the VNA) is coupled into a surface mode via diffraction at a 0.5 mm parallel-sided aperture formed between the sample and an aluminium blade. Using a second aperture placed at a distance L_1 along the surface from the first, the surface mode is coupled back to free propagating radiation, which is then collected and detected via a second microwave horn antenna (also connected to a VNA, but to a different port). The phase of the recorded signal can be used to obtain information about the dispersion of the surface modes supported by the structure. However in order to obtain an absolute phase measurement, it is necessary to record the data at two different values of L (the separation between the blades), hence the dispersion of the mode can be calculated using the following equation

$$k_x = \left(\frac{\phi_2 - \phi_1}{\Delta L} + \frac{\omega}{c} \right), \tag{3.2.3}$$

(for when radiation is incident in the plane containing the x-axis) where ϕ_1 and ϕ_2 correspond to the phase of the measured signal when the blades are at L_1 and L_2

respectively (where $L_2 > L_1$), $\Delta L = L_2 - L_1$. Note the ω/c term i.e. k_0 corresponds to the addition of the momentum associated with the light line. Note this analysis was developed from the work undertaken in [44].

A sheet of aluminised mylar was placed underneath the blade on the surface of the sample to ensure that equivalent boundaries conditions on the aperture (defined by the edge of the blade and the sample) were maintained. This also had the effect of enhancing the strength of the signal associated with the surface mode when TM-polarised radiation was incident on the aperture. However when TE-polarised radiation is incident on the sample through this aperture, there is no component of the incident E-field vertical to the sample, as such the radiation is insensitive to the presence of the aluminised mylar on the sample.

Whilst it can be advantageous to maximise the strength signal, it is actually only the phase information that is used to calculate the dispersion of the mode, therefore it is most useful to optimise the setup to obtain 'clean' phase information for as wide a frequency range as possible, resulting in characterising the dispersion of the mode at the highest wave vector values as possible. Further discussion on this will be presented in Chapter 5.

3.3 Sample Fabrication

3.3.1 Brass Tube Hole Arrays

The experimental samples investigated in Chapter 4 and 6 were constructed from close-packed arrays of brass tubes. The tubing was sourced is long lengths that were cut down to the required size, placed on a metal plate and clamped in place by four pieces of metal placed around the edge of the sample. It was necessary to fill the tubes for both samples with wax. Molten wax was poured into the each of the samples, ensuring any air bubbles were removed. The samples were overfilled to allow for any 'shrinking' of the wax upon cooling. Once cooled, the excess wax was removed from the top interface of the sample.

3.3.2 Zigzag Hole Array

The zigzag sample in Chapter 6 was fabricated using a Rapid Prototyping 3D printing machine (*Project*^{TM} *HD 3000*). 3D printers are a versatile tool often used by designers and engineers, as well as hobbiest, capable of physically realising computer designed complex 3D geometries into a 3D part using an additive layer-by-layer process. In addition to the build material (that has a plastic-type appearance) from which the part is formed, a wax support material, designed to melt away in the post-processing of

the build, is used to provide structural support to the part during the build process and ensure a good surface quality. Two levels of build quality are available, HD (high definition) and UHD (ultra high definition), each has a different restriction on the build size, with the maximum x, y and z dimensions of the HD and UHD build $298 \times 185 \times 203$ mm and $127 \times 178 \times 152$ mm respectively. Typically UHD is used for when high precision, detailed features are desired.

The zigzag sample was designed using HFSS, where the software was simply utilised as a 3D drawing tool. It was then imported into Solidworks, a 3D CAD software package, as a .SAT file to generate the required file format for the software used by the 3D printer. (Equally it is possible to produce the design solely using Solidworks.) Since, the features of the zigzag sample were not particularly fine, initially the test sample was printed on HD mode, as advantageously it is possible to produce larger build parts on a single build when printing in this mode. However it was found that the surface quality was not sufficiently high, given that the part was to metallised. The zigzag sample therefore was constructed from nine different parts, produced from nine different UHD builds, each build took several hours to complete.

Before the individual parts were slotted together to form the complete sample in preparisation for metallisation, they had to undergo post-processing to remove the support material to leave only the build material, i.e. the computer designed part. The post processing technique has either two or three stages, depending on the amount of material used. For builds with a large amount of support material, the sample is first placed in a tray of melted wax (approximate temperature 65^{o}C) and then in hot oil, to remove the last of the support material. For builds with only a small amount of support material to remove, the melted wax step is not necessary. The timings of these steps are highly dependent on the geometry of the parts, sometimes taking only a few minutes to complete. Finally the 'de-waxed' part is placed in a degreasing agent to remove the excess oil. The structures can be slightly weakened and deformed due to thermal stress from exposure to the hot/oil, followed by quick cooling. In order to reduce the possibility of permanent deformation, where possible the part must be clamped. Exposure to these temperatures for a period of time can also cause some shrinkage in the size of the structure, this must be taken into account in the calculations of the design.

The subsections of the sample was sent to an external company (Morganics [64]) for metallisation. This technique involves coating each surface with an nanocrystalline layer of copper, approximately 0.15 mm thick. Due to it's ultra-fine crystalline structure, it is found to be significantly stronger than natural copper. The final sample can be approximated as a near-perfectly conducting substrate perforated by an array of holes.

3.4 Finite Element Method (FEM) Modelling

The electromagnetic response of the structures discussed in this thesis have been simulated using a numerical technique called Finite Element Method (FEM) modelling. The software package used for FEM modelling is the High Frequency Structure Simulator (HFSS) from Ansys, Inc. [65]. All structures considered in this thesis are periodic, this allows the structures to be represented by a single unit cell, with repeat boundary conditions, to be solved using the FEM modelling approach. Advantageously this reduces the computational time required to solve the model, which allows the EM simulation of complex systems with high precision. Before Maxwell's equations are solved the structure geometry first rendered with a 3D CAD user interface, and materials are assigned to the constituent elements within the unit cell. This rendered representation of the structure is then approximated by many tetrahedral elements to form a mesh. The elements of the mesh are the 'finite elements' in which the EM field is later solved. Within each finite element, a solution is found for the EM fields, which are interpolated so that Maxwell's equations are satisfied across the boundaries between the elements. This process is performed to generate a solution for the whole geometry. Once the field solution has been found, the generalised-S matrix solution is determined.

3.4.1 Solving Maxwell's Equations in the Mesh

Mathematically, HFSS solves for the electric field **E** using equation 3.4.1, subject to excitation and boundary conditions.

$$\nabla \times \left(\frac{1}{\mu}\nabla \times \mathbf{E}\right) - k_0^2 \epsilon \mathbf{E} = 0, \tag{3.4.1}$$

where k_0 is the free space wavenumber and ϵ and μ are the relative permittivity and relative permeability, respectively. The magnitude of the magnetic field **H** is calculated using the following equation:

$$\mathbf{H} = \frac{1}{\omega\mu}\nabla \times \mathbf{E} \tag{3.4.2}$$

Solutions for **E** and **H** must be found for all the elements from which the mesh is formed. The resulting differential equations, that are in the form of equation 3.4.1, are combined into a matrix and solved for **E** numerically. Once the fields have been determined, a generalised scattering matrix (S-Matrix) is derived for the system, from which optical properties such as transmission or reflectivity can be extracted. Further, it is also possible for the software to calculate the eigenmodes of the system, and their associated fields, by finding the frequencies at which the poles of the S-Matrix occur [66].

3.4.2 CAD Modelling Tools and Assigning Materials

The 3D modeller (integrated CAD package) in HFSS is used to create the physical model that is required to be analysed. The 3D modeller is fully parametric, that is each variable, including geometric dimensions and materials properties may be assigned parameters, allowing for the easy scaling or 'tuning' of the structure. A library of commercially available, and commonly used materials are stored within HFSS. Additionally it is possible to include user-defined materials within the model, which can have either fixed or frequency dependent variables.

3.4.3 Assigning Boundary Conditions

Boundaries are applied to specific surfaces of the 3D object. They have two main purposes, to create an open/closed model or to reduce the geometry, or secondly to reduce the electromagnetic complexity of the modal. The most common boundary used in the modelling work in this thesis is the master-slave boundary. It is a periodic boundary condition that allows infinitely periodic structures to be modelled as a single unit cell. The master and slave conditions must be applied as a pair of boundaries (as shown in Figure 3.4 (a) and (b)), such that the E-field on one 'slave' surface is forced to matched the E-field on the 'opposite' slave surface. The pair must be assigned to identical surfaces, which are planar and are on the outside of the model.

Perfectly Matched Layers (PMLs) boundaries have also be used in the modelling work in this thesis. PMLs are a type of radiation boundary that are used to terminate models. They are made from fictitious material that is designed to be absorbing in the direction to the surface. Due to their highly anisotropic material they are designed to effectively absorbs waves that strike the boundary at non-normal incidence i.e. diffracted waves or for non-normal incident or reflected waves.

3.4.4 Excitation

There are several types of excitation in HFSS, however much of the modelling results presented in this thesis has been calculated with Floquet port excitations. Floquet ports are typically used for large periodic planar structure such as frequency selective surfaces or photonic bandgap structure. These are used as they allow the calculation of the intensities of each diffracted mode, using the Floquet-Bloch theorem. The Floquet ports are defined on the incident and exit face (which for a reflection model would be the same as shown in Figure 3.4 (d)). Radiation is injected into the model as plane waves that comprise a series of Floquet modes. The ports are defined by unit vectors which dictate the electric field of the mode.

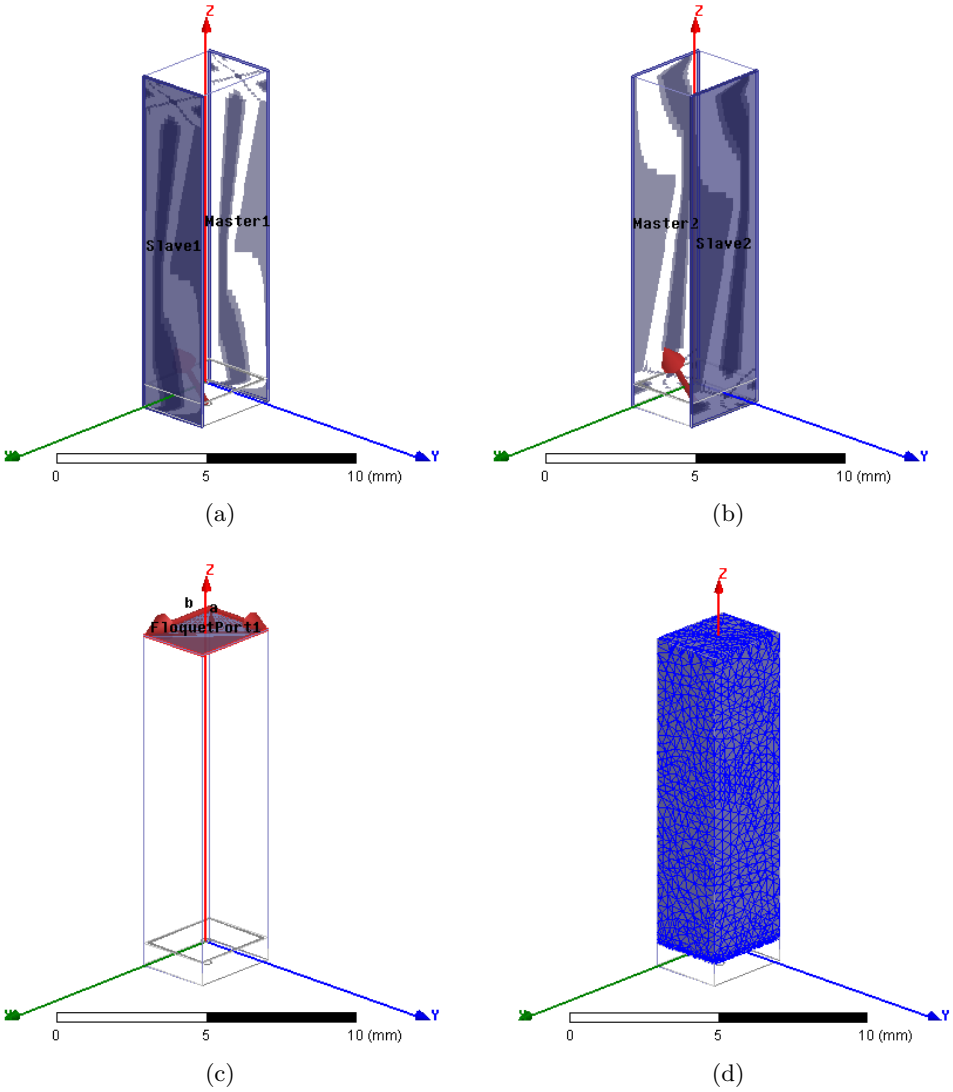

Figure 3.4: Unit cell of Sievenpiper structure. Highlighted faces show the position of (a) the first pair of master-slave boundary conditions, (b) the second pair of master-slave boundary conditions and (c) the Floquet ports. An example of the tetrahedral mesh is shown in (d).

3.4.5 Meshing

For an accurate solution to be obtained for the EM response of a structure, HFSS uses an adaptive iterative solution process, where the mesh is refined iteratively in regions where the electric field solution error is high. Initially, a coarse mesh is created in the unit cell (an example of which is shown in Figure 3.4 (d)). With that initial mesh, HFSS computes the electromagnetic fields at the user-defined solution frequency.

The solution frequency is the frequency at which HFSS explicitly solves a given solution and it is also the frequency that the adaptive solution operates to determine whether a model has converged or not. The solution frequency is generally chosen to

correspond to the largest frequency considered in a spectral sweep. This is because HFSS attempts to generate a refined mesh with maximum tetrahedral side length of 0.33 of the corresponding solution frequency wavelength. The delta-S parameter is the main criterion used by HFSS to determine whether the model has converged.

Due to the relationship between the calculated S-matrix and the electric field in the simulations, a useful number is the delta-S value, it is a change in magnitude between two consecutive passes, or change in electric field distributions between successive solutions. The delta-S number should be set between 0.005 and 0.01 for a majority of the models. From these results HFSS determines the regions where the exact solution has a high degree of accuracy. Tetrahedra are refined by creating a number of smaller tetrahedral that replace the original larger element. Another solution is generated with the new mesh, the error is computed and the process is repeated until the convergence criteria are satisfied, or the number of user defined adaptive passes are completed.

3.5 Conclusions

In this chapter an overview of the experimental methods and numerical techniques used to investigate the structures discussed in this thesis is presented. The free-space measurement techniques employed to record the transmission and reflections from structures have been discussed, as well as the blade-coupling and phase-resolved measurement technique used to directly measure the dispersion of modes. The methods for fabricating the hole array structures are discussed and finally a brief overview of the numerically modelling techniques used to produce the majority of the modelling results presented within this thesis is presented.

Chapter 4

Square Hole Array

4.1 Introduction

In this chapter a thorough study of diffractively coupled surface waves supported by a pseudo-plasmonic structure formed from a close-packed array of square cross-section, close-ended holes in a metallic substrate is presented. A periodic 'coupling-in' grating, comprising metallic rods of circular cross-section is used to control the strength of diffractive coupling of incident radiation to the surface waves supported by the hole array. However, a key issue not previously discussed in the literature is addressed by the work in this chapter; it is shown that the response of the structure is highly dependent on the position of the coupling-in grating relative to the hole array, a direct consequence of the pitch of the structure and the wavelength of the probing radiation being comparable. Not only is the position of the metallic rods comprising the grating relative to the hole array significant in determining the dispersion of the supported surface modes, it is also found that the response of the structure can be strongly perturbed by breaking electrical contact between the grating and substrate. Information about the modes supported by the hole array is obtained by experimentally characterising the azimuthal-dependent reflectivity response of the structure at a fixed polar angle, using free-space measurement techniques. For comparison, the surface modes diffractively coupled by a dielectric grating formed from glass rods is also presented.

4.2 Background

As discussed in Chapter 2, drawing analogies between the behaviour of surface plasmon polaritons (SPPs) at optical frequencies, it was Pendry and his co-workers who first introduced the concept of 'spoof' or 'designer' surface plasmons [3, 4]. They demonstrated the confinement of electromagnetic surface waves at the interface between a perfect electrical conductor (PEC) and vacuum, in the long wavelength limit via subwavelength structuring. However unlike conventional SPPs the behaviour of these 'spoof' SPPs, is

purely governed by the geometry of the structure. Advantageously the geometrically induced nature of these surface waves leads to the possibility of tailoring their properties to achieve almost arbitrary dispersion, simply through design. For instance, Pendry proposed [3] that the frequency of the fundamental localised resonance supported by an array of infinitely deep subwavelength holes in a PEC substrate, i.e. the cutoff frequency of the holes, defined the asymptotic limit or 'effective surface plasma frequency' for the dispersion of the surface wave supported by the substrate.

The assumptions intrinsic to Pendry and his co-worker's analytical description of the dispersion of these 'spoof' surface waves however were later found to be inadequate. Adopting an effective medium approach, they only considered the response of these substrates in the long wavelength limit where it was assumed incident radiation was insensitive to the subwavelength structuring, i.e. could not resolve the detail of the holey structure. Further, they only considered the specular field outside the hole and the fundamental waveguide mode (TE_{10}) when describing the field inside the cavity. This information was later proven to be insufficient to provide a precise description of the surface wave dispersion relation and a series of studies followed [5, 6, 56–58] which provided corrections to Pendry and his co-workers studies. In particular Hendry *et al.* [6] discussed how the inclusion of evanescent diffracted orders associated with the periodicity of the lattice, was of the utmost importance to accurately describe the surface wave dispersion relation in this region. The effect of the finite depth of the holes was also included in Hendry and his co-workers analysis, thus providing a full analytical description of the surface modes supported by a metallic substrate patterned with a two-dimensional square array of square holes in the low frequency limit (i.e. microwave regime). Excellent agreement with experimental data was shown. In addition to the aforementioned studies, which provided numerical corrections to Pendry's original surface wave dispersion relation for periodic structures in the long wavelength limit, the existence of these structurally-dictated surface modes was later confirmed by a wealth of experimental and indeed further numerical studies, as discussed within Chapter 2.

As discussed in Section 2.2.2 it is necessary to match the momentum of the surface waves to incident radiation and in the literature a variety of methods have been employed to experimentally characterise and couple incident radiation to the bound surface modes supported by these structures. For instance, prism-coupling techniques have been used to characterise the transverse-electric (TE) and transverse-electric (TM) mode supported by an ultra-thin metasurface [67], as well as excite surface waves on a three-dimensional brass wire medium metamaterial in the microwave regime [68]. Near field measurement techniques utilising a stripped coaxial antenna have been employed to demonstrate the lateral confinement of a 'domino plasmon' on a periodic chain of metallic cuboids [44] and when combined with a collimating beam apparatus, to excite and

detect the surface modes supported by an array of pillars on a conducting substrate [69]. In conjunction with phase-resolved measurements, microwave radiation incident through wedge waveguides and a slit aperture have been utilised to obtain the dispersion of the symmetric and anti-symmetric surface modes supported by a highly conducting sheet perforated with a two-dimensional array of subwavelength holes [59], as well as the family of structurally-dictated anisotropic surface modes on an array of close-ended square holes [70], respectively. Further, direct measurement of the confinement and propagation of terahertz electromagnetic surface modes bound to a metal surface perforated with a 2D subwavelength array of holes, have been performed using a subwavelength aperture defined by a razor blade and the sample [26, 71]. A high-efficiency surface wave coupler at microwave frequencies using a gradient metasurface (GM) formed from a thin super cell of six split-ring resonators (SRRs) has also been demonstrated [72]; in this system normally incident radiation can directly couple to the bound modes supported by the GM surface.

However, it was grating-coupling techniques that were utilised in the first experimental study verifying these 'designer' surface waves in the long-wavelength limit [2] following Pendry's original proposal [3]. Hibbins and his co-workers placed an additional coupling-in grating on top of a hole array to provide the necessary momentum enhancement to couple incident radiation to the surface modes supported by the substrate. Note that unlike the alternative methods described previously, this momentum-matching technique allows for the experimental characterisation of the surface mode within the radiative region (i.e. the region of momentum space in which incident radiation can directly couple to modes supported). A sinusoidal diffraction grating [73] was an early realisation of a structure upon which surface plasmon-like modes at microwave frequencies were experimentally observed; the periodicity of the structure was used directly to couple incident radiation to the supported surface modes. More recently the transmission enhancement through a metamaterial slab in the microwave region has been attributed to the excitation of surface waves by placing a diffraction grating either side of the slab [68]. The diffraction grating, as in Hibbins *et al.* study and the work in this chapter, simply provided a mechanism to couple radiation into and out of the surface modes supported by a pseudo-plasmonic structure i.e. the metamaterial slab or hole array.

There is a key issue not addressed however by Hibbins *et. al* [2] or previous studies reported in the literature, which provides the motivation for the work in this chapter. In Pendry *et. al's* seminal work they assumed the pitch of the structure and the size of the holes to be ultra-subwavelength. However the periodicity of the hole array and coupling-in grating *are* comparable to the wavelength of the probing radiation in Hibbins *et al.* study. Furthermore it is shown in this chapter that the position of the coupling-in

grating with respect to the hole array can greatly distort the dispersion of the surface mode supported by the hole array. However this perturbation could be considered advantageous, as it introduces a further degree of freedom in tailoring the response of the structure. Note it is difficult to characterise artificial materials whose feature size whilst less than the wavelength of the incident radiation, are only marginally so. In these structures the periodicity of the structure is significant, but not wholey responsible for the observed effects. True metamaterials can be described with homogenized material parameters and are often based on periodically arranged resonant elements, with periodicities typically smaller than the wavelength of the incident radiation by a factor of 5 or 10 times [51]. This is not the case for the sample in this Chapter, nor for those in Refs [3–6, 56, 58]. For these examples it is not possible to describe their surface wave dispersion relation by obtaining local frequency-dependent optical constants, their response is influenced by near-field diffractive effects.

In this chapter, a rigorous investigation into grating-coupling to surface modes supported by an array of close-packed, close-ended square cross-section holes in a near-perfectly conducting, is presented. The structure under investigation can be considered analogous to a shallow monograting in the optical regime formed from periodically corrugating a plasmonic metal, which supports surface plasmon polaritons [74]. However, rather than corrugating the plasmonic metal directly, the structure discussed in this chapter can be essentially considered as being comprised from two elements; the hole array which creates the necessary boundary conditions to support a bound surface mode (analogous to the plasmonic metal) which has a limiting frequency defined by the fundamental resonance of the hole (analogous to the surface plasma frequency), and an additional coupling-in grating placed on top of the hole array to enable diffractive coupling to the supported surface modes. Since it was with a similar structure that Hibbins *et. al* [2] provided the first experimental verification of these engineered surface waves inside the light cone at microwave frequencies in 2005, it is useful to present a brief overview of the study to provide a context for the work in this chapter.

The coupling-in grating, formed from metallic rods with a uniform circular cross-section of radius $r = 1.6\,\mathrm{mm}$, which extended the length of the hole array, was placed on top of the metal regions of the substrate at a periodicity twice that associated with hole array. Information about the dispersion of the modes supported by the structure was obtained by recording the frequency of the reflection minima as a function of the polar angle (θ). The experimentally measured (crosses) and predicted (solid black curve) dispersion of the surface modes excited by a TM-polarised field incident in the plane containing ($\phi = 0°$) and perpendicular ($\phi = 90°$) to the grating vector are shown in Figure 4.1 (a) and (b) respectively. The voids (holes) were filled with wax to reduce the fundamental resonance of the structure, defined approximately by the cutoff frequency

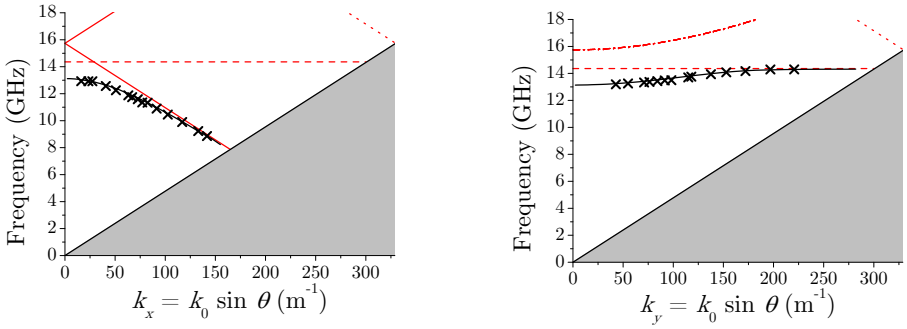

(a) (b)

Figure 4.1: Predicted (black line) and measured (crosses) dispersion of surface wave excited by a TM-polarised field incident in the plane (a) containing ($\phi = 0°$) and (b) perpendicular ($\phi = 90°$) to the grating vector. The solid and dotted red lines correspond to the first and second order in-plane diffracted light lines respectively and the dashed-dotted line the first-order out-of-plane diffracted light line. The horizontal dashed line corresponds to the cutoff frequency for a wax-filled infinitely long hole of square cross-section, side length $a = 6.96$ mm. The grey shaded area corresponds to region of momentum space not available to an incident photon. Reproduced with permission from [2].

of the hole (red horizontal dashed line Fig. 4.1 for a hole of infinite length) below the onset of diffraction. The sample was rotated by $\phi = 90°$, such that diffraction due to the coupling-in grating was in the plane orthogonal to the rods. Since the light line associated with this diffraction (dashed-dotted curve Fig. 4.1 (b)) increases hyperbolically with increasing wavevector, the surface mode therefore could approach its limiting frequency purely defined by the fundamental resonance of the system.

In this chapter, the azimuthal (ϕ)-dependent reflection from the structure has been recorded at a fixed polar angle ($\theta = 30°$). From this data, information about how the position of the coupling-in grating, relative to the hole array, perturbs the dispersion of the surface modes supported by the structure can be obtained.

4.3 Experimental Sample and Techniques

A schematic representation of the hole array structure, which is formed from a close-packed array of finite-depth, wax-filled, close-ended square cross-section brass tubes, can be seen in Figure 4.2 (a), together with a photograph of the sample in Figure 4.2 (b) (note for clarity, in the photograph the metallic plate forming the base of the structure is not shown and holes are air-filled.) The hole array can be characterised by the following parameters; the width of the hole, a, the pitch of the structure, d, the relative permittivity and permeability of the material filling the hole, ϵ_h and μ_h, respectively,

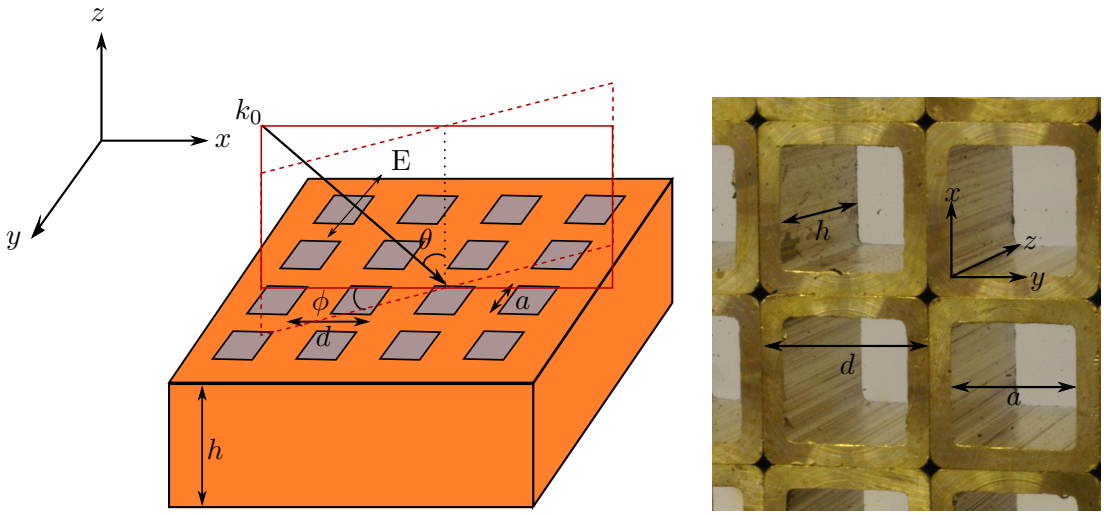

(a) (b)

Figure 4.2: (a) Schematic representation of square hole array. The holes (shaded purple) are of size a and the pitch of the structure is labelled d. (b) Photograph of square hole array sample. Note the coupling-in grating is not shown.

and finally the hole depth, h. In this study the aforementioned parameters have the following values $a = 6.96$ mm, $d = 9.525$ mm, $\epsilon_h = 2.25$ ($\mu_h = 1$) and $h = 45$ mm.

The fundamental localised resonance of an infinitely long guide is dictated by the lowest order waveguide mode (TE_{01}) supported by each hole. For a single, isolated square guide of infinite length, this frequency is defined by the cutoff (ν) of the hole and is given by equation 4.3.1

$$\nu = \frac{c}{2a\sqrt{\epsilon_h \mu_h}} \tag{4.3.1}$$

where a, ϵ_h and μ_h are as defined previously. The frequency of the fundamental mode supported by a finite length guide will be perturbed upwards in frequency from that of the cutoff of an infinite length guide, due to the additional momentum contribution from the longitudinally quantised field associated with its finite depth. As discussed in Chapter 2, it is this fundamental localised resonance that the first order surface mode is limited in frequency by. Note, as will be shown in this chapter, this frequency will be further perturbed by the addition of the coupling-in grating to the system.

Microwave radiation is incident on the sample in the xz-plane at the fixed polar angle $\theta = 30°$. A free-space measurement technique, full details of which can be found in Section 3.2.1.1, is used to record the azimuthally (ϕ)- dependent reflectivity response of the hole array together with coupling-in grating. From this, information about the dispersion of the surface modes supported by the hole array is obtained.

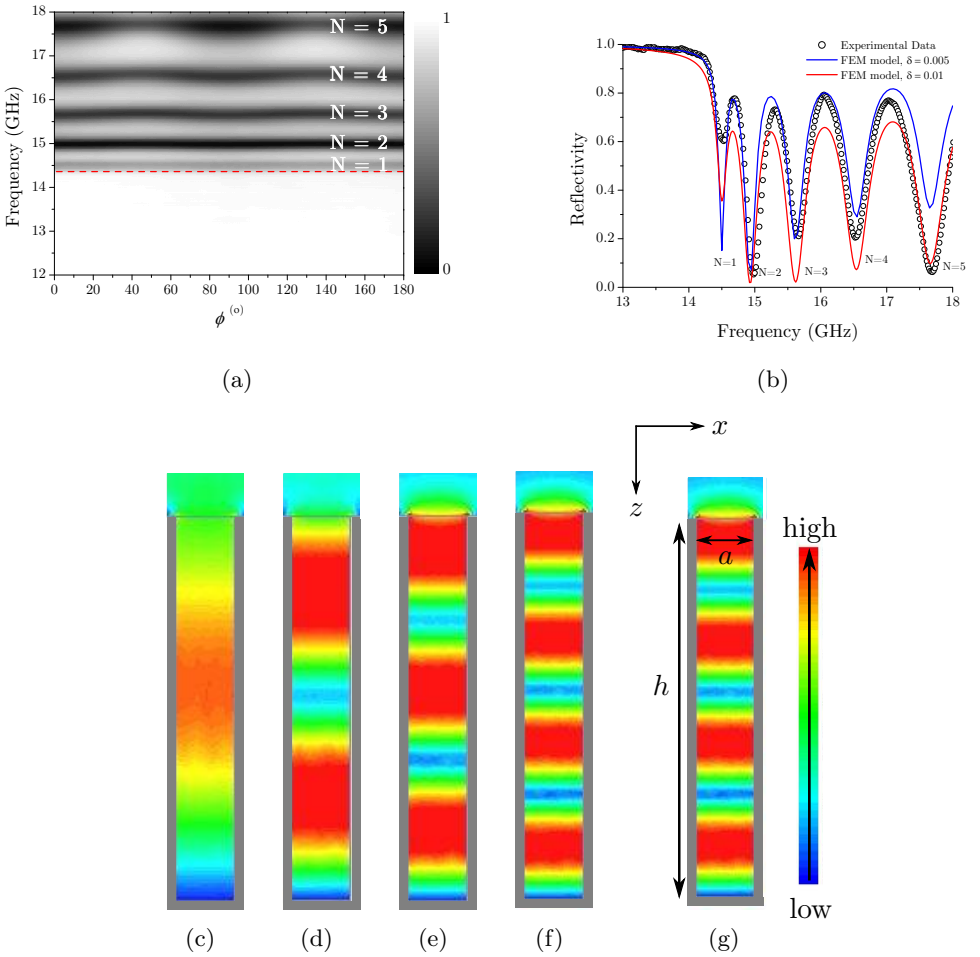

Figure 4.3: (a) Experimentally measured azimuthal ϕ-dependent reflectivity response (grey scale) of hole array structure to TM-polarised radiation incident at $\theta = 30°$, plotted on a linear scale from 0 to 1. Light and dark regions correspond to high and low reflection, respectively. The red dashed line represents the cutoff frequency of a single, isolated guide of infinite length. (b) Experimentally measured (circles) and predicted (curves) reflectivity response of the hole array to TM-polarised radiation incident on the sample at $\phi = 90°$ and $\theta = 30°$. A dielectric loss tangent, δ, (where $\tan\delta = \mathrm{Re}(\epsilon)/\mathrm{Im}(\epsilon)$) of 0.005 (blue curve) and 0.01 (red curve) have been used in the calculations. (c) Predicted time-averaged electric-field profiles associated with the first five modes supported by the hole array structure. Red and blue regions correspond to a high and zero field magnitude, respectively.

4.4 Experimental Results

4.4.1 Response of Hole Array

Before investigating the diffractively coupled surface waves supported by the hole array, it is first useful to understand the modes supported by simply the bare substrate, i.e. the

locally resonant modes of the holes. The azimuthal (ϕ)- dependent reflectivity response of the hole array to TM-polarised radiation incident on the structure at the fixed polar angle of $\theta = 30°$, is shown in Fig. 4.3 (a). Here dark and light regions correspond to low and high reflectivity, respectively. A series of relatively flat-banded modes (dark bands), labelled $N = 1 - 5$, are observed above the cutoff frequency for a hole of infinite length (red dashed line Fig. 4.3). These modes have been coupled to incident radiation via near-field diffraction.

In order to confirm the expected properties of the wax filling the holes, the predicted reflectivity response of the hole array to TM-polarised radiation incident on the sample at $\phi = 90°$ ($\theta = 30°$) calculated with wax characterised by a real permittivity (ϵ_h) of 2.25 and dielectric loss tangent (δ) of 0.005 and 0.01 (blue and red curves respectively, Fig. 4.3 (b)), is compared to the experimental data (circles Fig. 4.3 (b)). Excellent agreement in terms of the position of the reflectivity minima is shown, thus implying the correct value of the real part of ϵ_h (and the hole depth) has been used in the calculation. However, the frequency-dependent discrepancies between the width and depth of the measured modes and the predicted response are clear. This behaviour is understandable since the depth and width of a mode is determined by the ratio of the radiative and non-radiative losses in a system [75], and the dielectric loss tangent is a frequency-dependent non-radiative loss channel. Whilst good agreement is shown at low frequencies between the measured data with the simulations when a value of 0.005 is used for the dielectric loss tangent in the calculations (blue curve Fig. 4.3 (b)), at higher frequencies the response is more accurately described by a dielectric loss tangent of 0.01 (red curve Fig. 4.3 (b)). Since the primary focus of the work in this chapter is the mode supported below the fundamental resonance of the hole, a dielectric loss tangent of 0.005 is used to obtain the predicted response from here on.

The predicted time-averaged electric-field profiles, plotted at frequencies corresponding to the reflection minima associated with the first five modes supported by the hole array (labelled $N = 1 - 5$ Fig. 4.3 (a) and (b)) when TM-polarised radiation is incident on the sample at $\phi = 90°$ ($\theta = 30°$), plotted in the xz-plane, are shown in Fig. 4.3 (c)-(g). Here red regions correspond to high field enhancement and blue a field magnitude of zero. It can be seen close to the bottom of the guide, which experimentally has been terminated by a flat metal sheet, the magnitude of the E-field falls to zero, as required for a PEC boundary. At the top of the guide, the magnitude of the E-field is high. Each one of these resonances therefore can be approximated as an odd integer quarter wavelength quantisation of the field along the length of the holes. Obviously with increasing frequency, the wavelength reduces such that higher order quantisations are supported. Note that as expected, no surface mode is observed below the fundamental resonance of the hole array ($N = 1$) and the reflectivity is close to unity for frequencies below this.

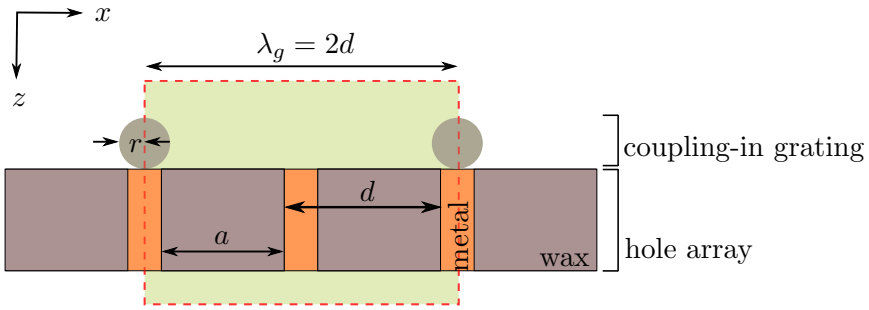

Figure 4.4: Schematic representation of a cross-section of the hole array and coupling-in grating. The coupling-in grating is formed from metallic rods of uniform circular cross-section, radius $r = 1.6$ mm, and is placed on top of the hole array on the metal regions at a periodicity $\lambda_g = 2d$.

4.4.2 Metallic Coupling-In Grating on Metallic Regions of Hole Array

In Section 4.4.1 the azimuthal (ϕ)-dependent reflectivity response of the hole array to TM-polarised radiation incident on the sample at a fixed polar angle ($\theta = 30°$) was shown. Without the addition of the coupling-in grating in the system, a family of flat-banded modes were observed, each associated with the fundamental localised resonance (TE_{10} waveguide mode) supported by the cavities. However as expected, no surface mode was observed. The role of the coupling-in grating is therefore to control the strength of diffractive coupling to the surface modes supported by the hole array which exists outside the light cone; the additional perturbation introduced by the coupling-in grating (which has a periodicity (λ_g) twice that of the hole array (as shown in Fig. 4.4) significantly alters the dispersion of the surface mode supported by the hole array. The momentum available to incident radiation can now be increased or decreased by integer multiples of the grating wavevector k_g (where $k_g = 2\pi/\lambda_g$), resulting in originally non-radiative modes being scattered or 'band-folded into the radiative region of momentum-space. A full description of this grating-coupling technique can be found in Chapter 2 whilst further examples of structures utilising their dual periodicity to induce 'band-folding' effects can be found in Refs [22, 23], as well as in Chapter 6 of this thesis. By recording the azimuthal (ϕ)-dependent reflectivity response of the hole array with the coupling-in grating placed on top, it is possible to obtain information about the dispersion of the surface modes supported by this structure.

Initially, as in the study of Hibbins *et al.* [2], the coupling-in grating is placed on top of the hole array on the metal regions in between the voids (holes), at a periodicity twice that of the hole array beneath ($\lambda_g = 2d$, where d is the periodicity of the hole array). A schematic cross-section of the hole array and coupling-in grating is shown in Figure. 4.4. The grating is formed from metallic rods of uniform circular cross-section of radius

$r = 1.6$ mm, which extend the full length of the sample. The experimental azimuthal (ϕ)-dependent reflectivity response of the structure to TM-polarised radiation incident at $\theta = 30°$ is shown in Figure 4.5 (a). Here dark and light regions correspond to low and high reflectivity, respectively. Note $\phi = 0°$ is defined to be when the grating vector is contained in the plane of incidence (i.e. perpendicular to the plane containing the metallic rods), commonly referred to as classical mount. It is possible to achieve radiative coupling to the surface modes supported by the structure with both linear polarisations (dependent on the orientation of the grating with respect to the plane of incidence); an electric field normal to the surface of the coupling-in grating can be achieved with either polarisation. Therefore for comparison with the data shown in Figure 4.5 (a), the corresponding TE-polarised response is shown in Fig. 4.5 (b). In addition to the series of flat-banded localised resonances, a dark band (reflection minima) is observed following the first-order parabolic diffracted light lines (solid red curves Fig. 4.5) and limited in frequency by the fundamental localised resonance in both the TM- and TE-polarised response. This band is associated with the fundamental surface mode supported by the hole array and it is clear that its coupling strength is highly dependent on the azimuthal angle (ϕ), as well as the polarisation of the incident field.

First consider the response of the structure when $\phi = 0°$. In this orientation the coupling-in rods lie perpendicular to the plane of incidence i.e. the plane of incidence contains the grating vector. TM-polarised radiation incident on the sample in this orientation is sensitive to the periodicity of the grating, since there is a component of the incident electric-field normal to the surface of the coupling-in grating. On examining the measured reflectivity data (Fig. 4.5 (a)) a dark band (reflection minima) is observed below the diffraction edge (solid red curve). However, as expected there is an absence of coupling to this mode with TE-polarised radiation when $\phi = 0°$ (Fig. 4.5 (b)), since there is no normal component of the incident electric-field to the grating structure.

Next consider the response of the structure to radiation incident in the plane that is perpendicular to the grating vector (i.e. parallel to the rods), corresponding to an azimuthal angle of $\phi = 90°$. It can be seen that the surface mode is weakly coupled to with TM-polarised radiation (Fig. 4.5 (a)), whilst there is an absence of coupling to this mode when the structure is illuminated with TE-polarised radiation (Fig. 4.5 (b)). The experimental response (circles) of the structure to TM-polarised radiation incident at $\phi = 90°$ ($\theta = 30°$) is shown in Figure 4.6 (a), together with the predicted reflectivity response (red curve Fig. 4.6 (a)). The first reflection minima is associated with the surface mode, and the five higher order modes with the localised resonances (waveguides modes) discussed in the previous section. Note that an angle of $\theta = 33°$ has been used in the calculations of the predicted reflectivity spectrum. Further modelling revealed (not shown) that whilst the position and depth of the localised resonances

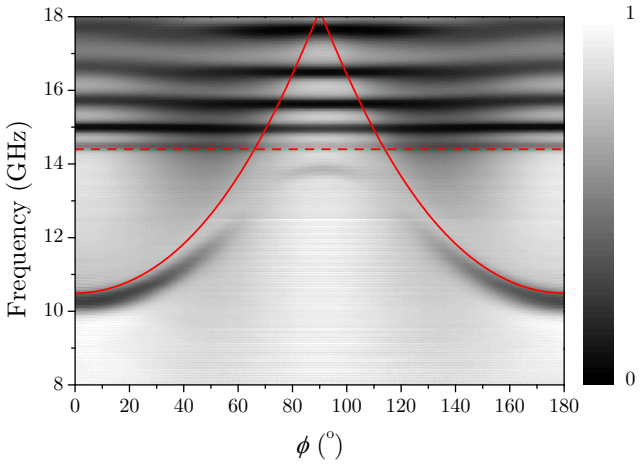

(a)

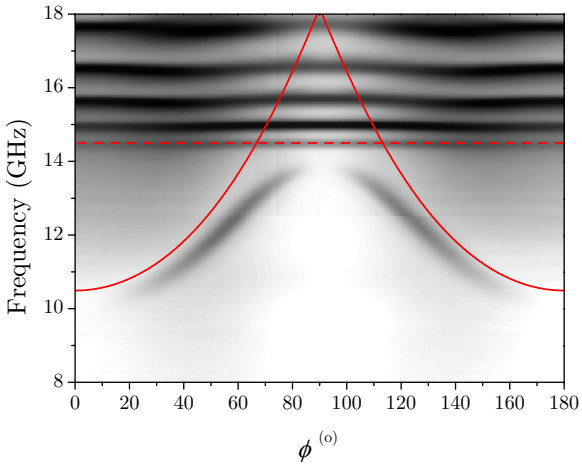

(b)

Figure 4.5: (a) TM- and (b) TE- polarised experimental azimuthal (ϕ)-dependent reflectivity response (grey scale) of the structure, when metallic rods are placed on the metallic regions of the hole array, to radiation incident at $\theta = 30°$, plotted on a linear scale from 0 to 1. Light and dark regions correspond to high and low reflectivity, respectively. The red dashed line represents the cutoff frequency of a single, isolated guide of infinite length and the solid red lines the first order diffracted light lines.

(waveguide modes) are insensitive to a variation in θ, the frequency of the reflectivity minima associated with the surface mode is highly sensitive to the angle of incidence (θ), as shown in Figure 4.1. It is found that a value of $\theta = 33°$ in the calculations provides the best fit to the experimental data. The broadening and shallowing of the experimentally characterised surface mode compared to the predicted response can be attributed to a spread in θ which is present in the experimental setup, as well as imperfections in the sample. The instantaneous vector electric field plotted at the frequency corresponding to the lowest frequency reflection minima associated with the surface mode (when $\phi = 0°$) is shown in Figure 4.6 (b). Here red regions correspond to high field enhancement and blue to a field magnitude of zero. It can be seen that high fields exist over the metal regions of the surface and the looping E-fields are typical of a surface plasmon-like mode (as discussed in Chapter 2).

For non-zero polar angles ($\theta \neq 0°$), a TM-polarised field will contain a component of electric field normal to the surface of the coupling-in grating. Therefore one would expect that it is possible to couple TM-polarised radiation incident at any azimuthal angle (except when $\phi = 90°$ and $\theta = 0°$) to the surface mode supported by the hole array. However, whilst a dark band (reflection minima) associated with the surface mode is observed following the first order diffracted light line in Fig. 4.5 (a), it is of note that the strength (depth) of this mode decreases dramatically within a small frequency band, centred around 13 GHz. The reason for the lack of coupling within this frequency window can be established by considering the geometrical constraint under which direct coupling of incident radiation to this mode is prohibited. This condition is met when the wavevector of the incident radiation of momentum $\mathbf{k}_0 \sin\theta$ and the wavevector of the surface wave ($\mathbf{k}_{\mathrm{SW}}$) are perpendicular. For a fixed θ, using simple trigonometry, at a particular frequency and for a particular value of ϕ, it will not be possible to achieve coupling between the incident radiation and the surface mode. Resolving for $\phi = 65°$, the frequency at which these two vectors are perpendicular occurs at $f = 13.1$ GHz. At frequencies close to this, the strength of the mode diminishes rapidly.

It has been noted previously that when TE-polarised radiation is incident on the sample in the plane perpendicular to the grating vector ($\phi = 90°$) despite the incident field containing a component of the electric vector normal to the surface of the coupling-in grating, there is an absence of coupling to the surface mode below the fundamental resonance of the hole array (Fig. 4.5 (b)). This can be attributed to the symmetry of the system, specifically the presence of the mirror plane perpendicular to the incident electric field. For light incident at $\phi = 90°$, the resulting surface wave is the product of two surface waves scattered from $\pm k_g$. But due to the presence of the mirror plane it is not possible to simultaneously excite both surface waves.

A further experiment has been carried out to demonstrate that coupling to the

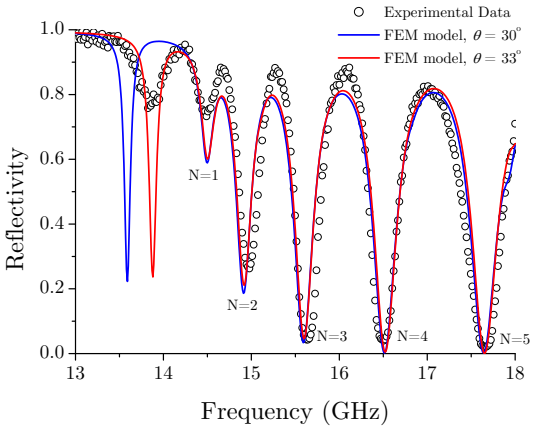

(a)

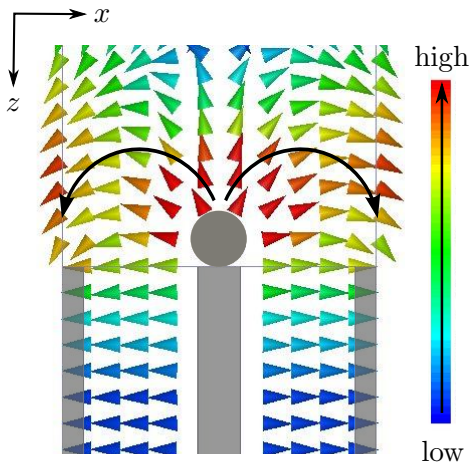

(b)

Figure 4.6: (a) Experimental (circles) and predicted (red curve) reflectivity response of the hole array with the coupling-in grating placed on the metal regions of the hole array (at a periodicity of $2d$) to TM-polarised radiation incident at $\phi = 90°$ ($\theta = 30°$). (b) Predicted instantaneous vector electric field plotted at the reflectivity minima associated with the surface modes excited by a TM-polarised field incident on the sample at $\phi = 0°$. Red and blue regions correspond to high and zero field magnitude, respectively.

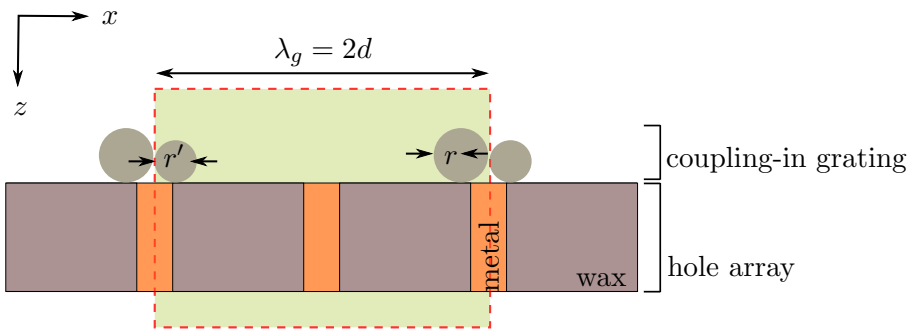

Figure 4.7: Schematic representation of a cross-section of the hole array and coupling-in grating. The coupling-in grating is formed from a pair of metallic rods of uniform circular cross-section, radius $r = 1.6\,\text{mm}$ and $r' = 1\,\text{mm}$, and is placed on top of the hole array on the metal regions at a periodicity $\lambda_g = 2d$.

surface mode with TE-polarised radiation, when the plane of incidence is perpendicular to the grating wavevector, can be achieved by reducing the symmetry of the system. The coupling-in grating, previously formed from periodically positioned single rods (of radius r), is replaced with one comprising paired rods of different cross-sections. Once again each rod has a uniform circular cross-section, which extend the width of the sample, however one of the paired rods has a radius of $r = 1.6\,\text{mm}$ and the second a smaller radius of $r' = 1\,\text{mm}$. Note that pitch of the coupling-in grating is still $2d$. A schematic representation of this dual-rod coupling-in grating and the hole array is shown in Figure 4.7. As can be seen in Figure 4.8 which shows the azimuthal (ϕ)-dependent reflectivity response of the structure to TE-polarised radiation incident on the sample at $\theta = 30°$, coupling to the mode at $\phi = 90°$ is achieved, evidenced by the reflection minima (dark band) at approximately 14 GHz.

4.4.3 Metallic Coupling-In Grating on Dielectric Regions of Hole Array

In this section it will be shown that it is possible to alter the dispersion of the surface modes supported by the hole array by changing the position of the coupling-in grating with respect to the hole array beneath. This is a direct consequence of the pitch of the structure and the wavelength of the incident radiation being comparable. If the pitch of the hole array was ultra-subwavelength ($\lambda_g << \lambda_0$), this structure could be approximated as a homogeneous plasmonic-like material, and the relative position of the coupling-in grating and hole array would not be a consideration in determining the dispersion of the supported surface modes. However, since the wavelength of incident radiation is such that it can resolve the features of the hole array and coupling-in grating,

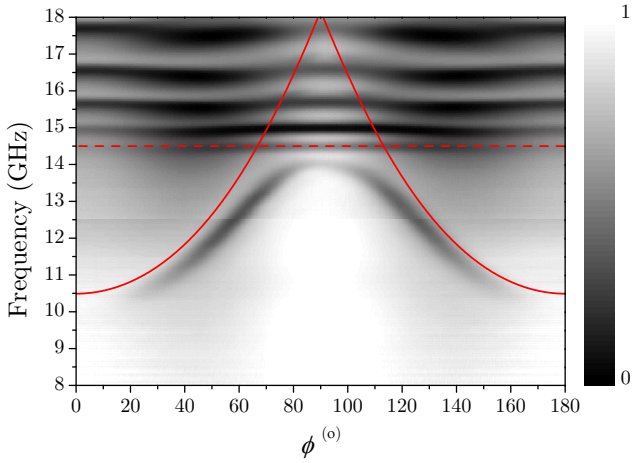

Figure 4.8: Experimental azimuthal (ϕ)-dependent reflectivity response (grey scale) of hole array and metallic coupling-in grating to TE-polarised radiation incident at $\theta = 30°$, plotted on a linear scale from 0 to 1. Light and dark regions correspond to high and low reflectivity respectively. The coupling-in grating is formed from paired rods of uniform circular cross-section, radius $r = 1.6\,\text{mm}$ and $r = 1\,\text{mm}$, placed on top of the metal regions of the sample, at a periodicity $2d$. The red dashed line represents the cutoff frequency of a single, isolated guide of infinite length and the solid red lines the first order diffracted light lines.

a thorough investigation into the effect that their position with respect to each other has on the dispersion of the surface modes supported by the hole array is required.

The coupling-in grating in this section is once again formed from metallic rods with a uniform circular cross-section of radius $r = 1.6\,\text{mm}$, which extend the full width of the hole array. As in the previous section, the rods are arranged such that they lie parallel to each other with a periodicity twice that of the hole array beneath ($\lambda_g = 2d$). However, each rod is now placed on top of the hole array over the voids (holes), rather than the metal regions. To achieve this whilst imposing equivalent boundary conditions on every hole and maintaining a $2d$ periodicity, the rods are placed on the sample at a spacing of $a/3 : 2a/3$, as illustrated in Figure 4.9. (Equally as long as the rods lay over the voids and the $2d$ periodicity is maintained, this could be any ratio except $a/2 : a/2$.) Obviously in this arrangement, the boundary condition on the top surface of the hole array has changed significantly compared to when the coupling-in grating lay on the metal regions of the substrate (in the limit where the diameter of the metallic rods and width of the metal regions are comparable); each void is now partially covered by a metallic rod. It can be predicted therefore that the fields of the surface mode supported by the hole array will be significantly perturbed by the presence of the coupling-in grating when the metallic rods lie over the voids.

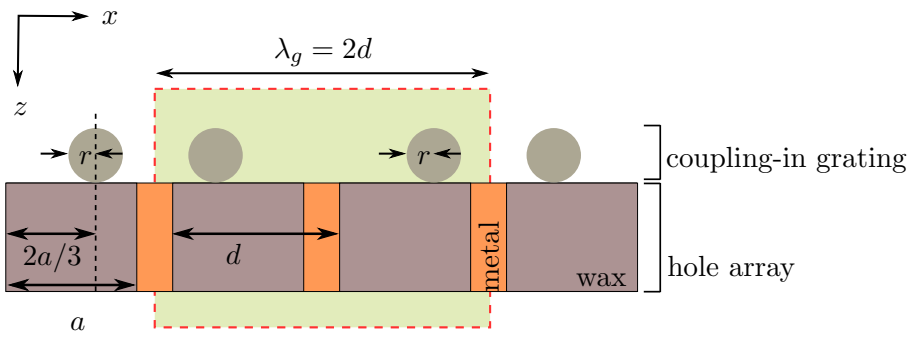

Figure 4.9: Schematic representation of a cross-section of the hole array and coupling-in grating. The coupling-in grating is formed from metallic rods of uniform circular cross-section, radius $r = 1.6$ mm, and is placed on top of the voids of the hole array at a periodicity $\lambda_g = 2d$, at a spacing $a/3 : 2a/3$.

The azimuthal (ϕ)-dependent reflectivity response (grey scale) of the structure to TM- and TE-polarised radiation incident on the sample at $\theta = 30°$ is shown in Figure 4.10 (a) and (b), respectively. Here light regions correspond to a high reflectivity and black a reflectivity of zero. The horizontal dashed line and solid lines represent the cutoff frequency of an infinitely long guide and first-order diffracted light lines, respectively. Perhaps one of the most striking features of these grey scale plots is the lack of coupling, evidenced by the highly reflecting regions (bright bands), observed at all frequencies for a certain range of azimuthal angles. This bright band is centred around $\phi = 90°$ in the TM-polarised response, and $\phi = 0°$ when TE-polarised radiation is incident on the sample. The bands of high reflectivity can be explained by considering the coupling-in grating to be acting in the similar manner as a wire-grid polarizer, i.e. a regular array of parallel metallic wires with a pitch that is subwavelength with respect to the probing radiation. When radiation incident on the structure contains a component of electric-field aligned parallel to the wires, the polariser (or coupling-in grating) behaves in a similar manner to the surface of a metal, reflecting the incident beam. That is, electrons in the metal sheet are free to oscillate in the direction of the incident field. However, the radiation emitted by the electrons is 180° out of phase with the incident radiation, resulting in very small levels of transmission [76].

The most significant result however is revealed on comparing the experimental results to the predicted response of the system. Figure 4.11 shows the experimental response (circles) of the structure to TM-polarised radiation incident on the sample at $\phi = 0°$ ($\theta = 30°$) together with the predicted response when there is a 10 μm gap between the grating and hole array (dashed red curve) and when the grating and hole array are in electrical contact (solid red curve). It can be seen that not only does the lower frequency mode (mode (A)) shift up in frequency by approximately 0.5 GHz when the hole array

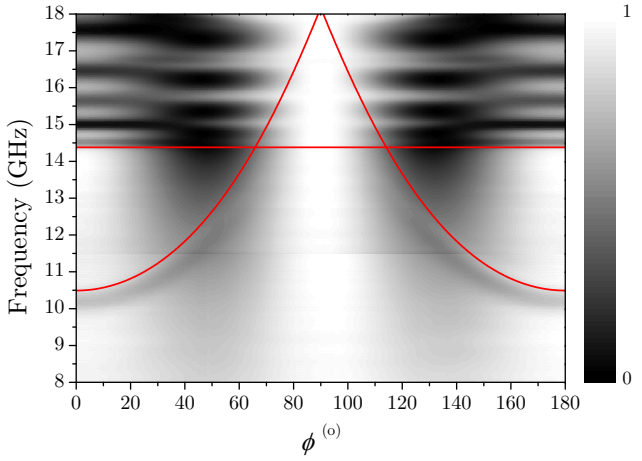

(a)

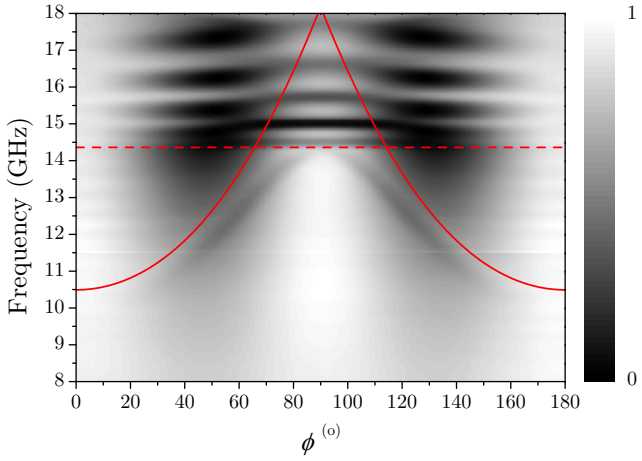

(b)

Figure 4.10: (a) TM- and (b) TE- polarised experimental azimuthal (ϕ)-dependent reflectivity response (grey scale) of the hole array and metallic coupling-in grating to radiation incident on the sample at $\theta = 30°$, plotted on a linear scale from 0 to 1. Light and dark regions correspond to high and low reflectivity respectively. The coupling-in grating is formed from rods of uniform circular cross-section, radius $r = 1.6\,\text{mm}$, placed on top of the voids(holes) of the hole array, at a periodicity $2d$. The red dashed line represents the cutoff frequency of a single, isolated guide of infinite length and the solid red lines the first order diffracted light lines.

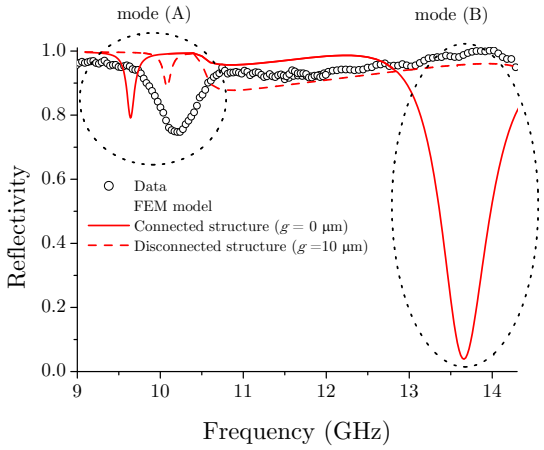

Figure 4.11: The experimental response (circles) of hole array and coupling-in grating (when it is placed over the voids of the hole array) to TM-polarised radiation incident at $\phi = 0°$ ($\theta = 30°$), together with the predicted response when there is a 10 μm gap between the grating and hole array (red dashed curve) and when the grating and hole array are in electrical contact (red solid curve).

and grating are disconnected, but more intriguing is the absence of the deep mode in the experimental data, observed in the predicted response centred at approximately 13.5GHz (labelled mode (B)), when there is a 10 μm gap between the coupling-in grating and hole array. The issue of the absence of this mode in the experimental data will be addressed in due course, first however consider the effect that the gap between the coupling-in grating and the hole array has on the position of mode (A) (i.e. the lower frequency mode in Fig. 4.11).

The frequency-dependence of mode (A) on the height of the coupling-in grating above the hole array, has been explored numerically using a system comprising a coupling-in grating formed from metallic rods of uniform square cross-section (2 mm $\times$ 2 mm), a schematic cross-section of which is shown in Fig. 4.12 (a). The grating has a pitch of $2d$ and is placed on top of the hole array at a spacing of $a/3 : 2a/3$. The system has been modelled with the coupling-in grating placed at different heights, g, above the hole array. Figure 4.12 (b) shows the predicted frequencies of the minima in reflectivity (squares) associated with mode (A), which have been excited by radiation normally incident on the structure in the plane containing the grating vector ($\phi = 0°$), when the coupling-in grating is placed at different heights (g) above the top plane of the hole array. The reflection minima occurs at approximately 12.0 GHz when the hole array and coupling-in grating are electrically connected (i.e. when $g = 0$). As the gap between the grating and hole array is increased, the frequency of the minima in reflectivity increases. This behaviour can be understood with the realisation that mode (A) is actually the lower edge of the band gap that originated from the splitting of two different energy

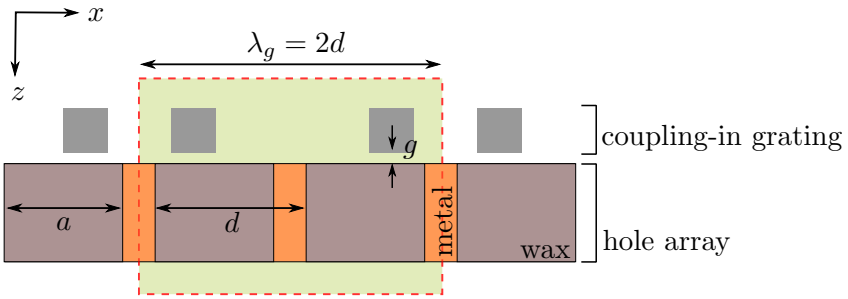

(a)

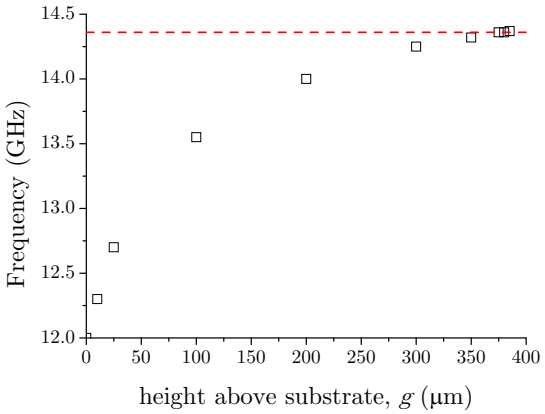

(b)

Figure 4.12: (a) Schematic representation of a cross-section of the hole array and coupling-in grating. The coupling-in grating is formed from metallic rods of uniform square cross-section (2 mm × 2 mm) and is placed on top of the dielectric regions of the hole array at a periodicity $\lambda_g = 2d$, at a spacing of $a/2 : 2a/3$. (b) Predicted minima in reflectivity (squares) associated with mode (A), excited by a normal incident beam in the plane containing the grating vector, as a function of height (g) of the coupling-in grating above the top plane of the hole array structure.

solutions of the surface wave at $k_x = 0$. As discussed in Section 2.2.3.1 a band gap in the dispersion of the mode will occur at a Brillouin zone, the size of which is determined by the difference in energy between the two different standing wave solutions. As expected, the coupling-in rods will perturb the evanescent fields of the surface mode supported by the hole array more when the grating is in closer contact with the substrate, evidenced by the predicted minima in reflectivity associated with mode (A) occurring at the lowest frequency when the rods and hole array are in electrical contact, indicative of a larger band gap. In the limit of large g the mode approaches the limiting frequency of the fundamental resonance of the hole (red dashed curve Fig. 4.12 (b)). Note that in the case when the coupling-in grating is placed over the metal regions of the hole array, only

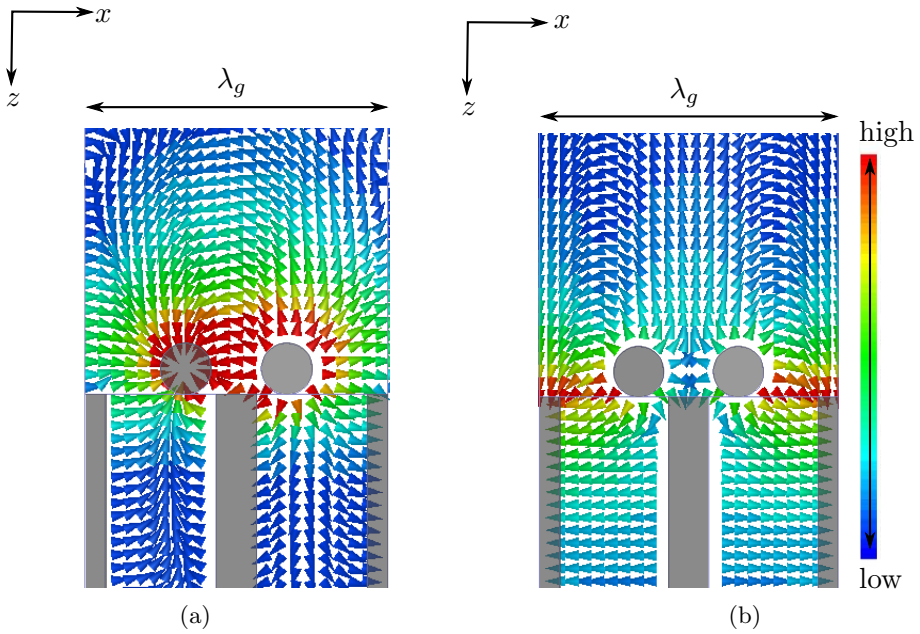

Figure 4.13: Instantaneous vector eclectic-fields of the mode associated with the (a) lowest and (b) highest band edge of band gap in the surface wave dispersion at $k_x = 0$. Red and blue regions correspond to a high and zero field magnitude, respectively.

one of the two energy solutions are possible, as the other standing wave solution would correspond to where the electrical charges would be required to sit on the voids (i.e. dielectric regions) of the hole array.

By observation of the fields it follows that the theoretically predicted higher frequency mode in Fig. 4.11, labelled mode (B), is the upper band edge of the aforementioned band gap in the surface wave dispersion. The instantaneous vector electric field, plotted in the xz-plane, associated with the lower and upper band edge of the surface mode supported when the coupling-in grating and hole array are in electrical contact, when the plane of incidence contains the grating wavevector ($\phi = 0°$), are shown in Figure 4.13 (a) and (b) respectively. It can be seen that high vertical fields are centred on the metal regions for the mode associated with the upper band edge and over the rods (dielectric regions) for the mode associated with the lower band edge. Note that the rods are connected by the ridges in the x-direction.

The question still remains though as to why only the mode associated with the lower band edge (mode (A)) is only slightly sensitive to a gap ($g \neq 0$) between the coupling-in grating and hole array, whilst the highest frequency mode (upper band edge, mode (B)) is supported only when electrical contact between the hole array and coupling-in grating is established. The answer is revealed when the distribution of charges on the coupling-in grating and hole array associated with mode (A) and mode (B) are considered.

Firstly consider the field distribution of the mode associated with the lower band edge (mode (A)) when the coupling-in grating and hole array are in electrical contact. As previously stated Figure 4.13 (a) shows the predicted instantaneous vector electric field plotted in the xz-plane of the mode associated with lowest band edge, excited by a TM-polarised field incident in the plane containing the grating vector. It can be seen that only horizontal E_x fields exist immediately above the metallic regions of the hole array, and high vertical fields (E_z) (red regions) are observed above the rods. Since E_z switches direction in between the rods, neighbouring rods are oppositely charged whilst the substrate is charge neutral; charge flow is from rod to rod through the substrate. Further evidence for this is provided by examining the predicted instantaneous vector electric field in the xy-plane at the top interface of the hole array (Figure 4.14 (a)). The black arrows represent the direction of the electric vector underneath each rod. It can be seen that high vertical fields (red regions) are observed beneath each rod, and the electric vector underneath neighbouring rods is in the opposite direction. A schematic representation of the charges on the rods is shown in the inset of Fig. 4.14 (a), the left hand rod is said to be negatively (-) charged and the right hand one positively charged (+).

Next consider the field distribution of the mode associated with the upper band edge (mode (B)) when the coupling-in grating and hole array in electrical contact. Once again, as previously stated, Figure 4.13 (b) shows the predicted instantaneous vector electric field plotted in the xz-plane of the mode associated with the upper band edge, excited by a TM-polarised field incident in the plane containing the grating vector. High vertical fields are now observed over the metallic regions of the substrate (away from the coupling-in grating) and E_z switches direction over the dielectric regions of the hole array. Each rod now has the same charge and the substrate the opposite charge; charge flow is from rod to substrate. Further evidence for this is revealed on examining the predicted instantaneous vector electric field in the xy-plane at the top interface of the hole array (Figure 4.14 (b)). The black arrows once again represent the direction of the electric vector underneath each rod, the electric vector is in the same direction underneath each rod; neighbouring rods carry the same charge. A schematic representation of the charges on the rods is shown in the inset of Fig. 4.14 (b), each rods carry the same positive (+) charge.

Now consider the effect of raising the coupling-in grating above the substrate on both modes (A) and (B). It is possible for the lower frequency mode (mode (A)) to still be supported when electrical contact between the hole array and sample is broken, since it is possible for the substrate to remain charge neutral. The only difference between the charge distribution associated with the connected and disconnected structure for mode (A) being that high vertical fields are induced in the gap between the metallic regions

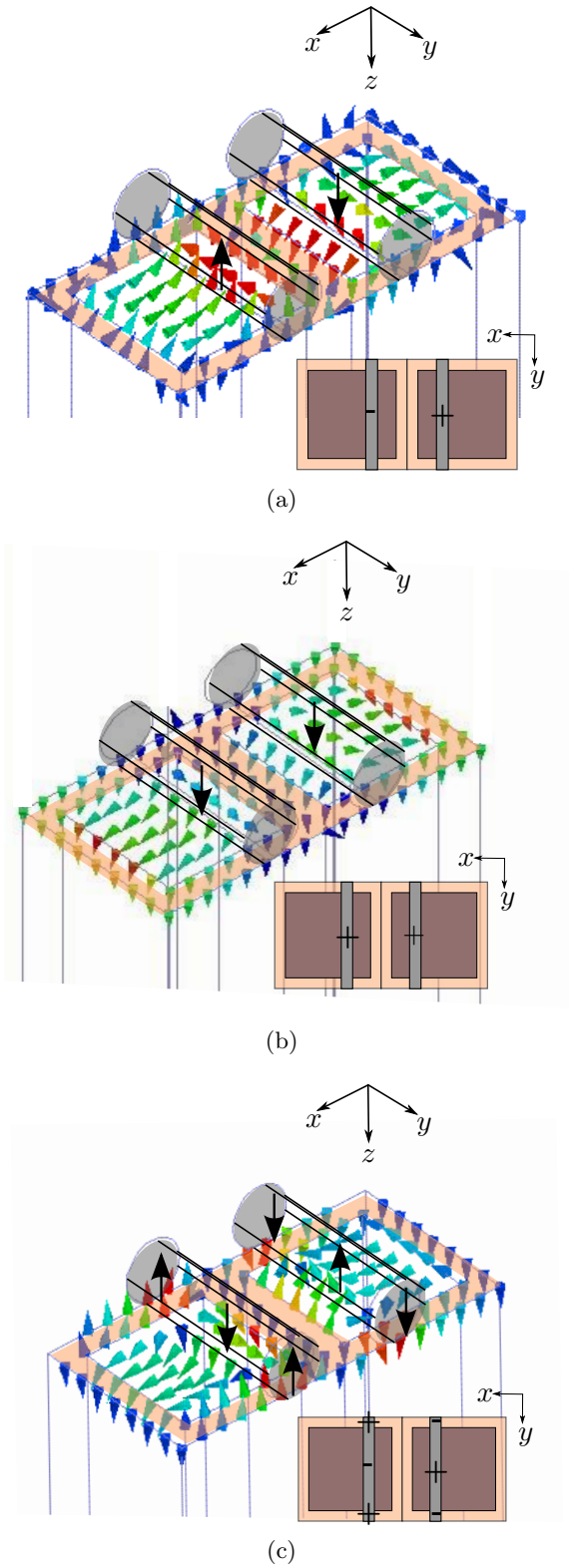

Figure 4.14: Predicted instantaneous vector electric field plotted in the xy-plane at the top interface of the hole array associated with (a) mode (A) and (b) mode (B) when the grating and hole array are connected, and (c) mode (A) when there is a $g = 10\mu$m gap between the grating and hole array. Red and blue regions correspond to a high and field magnitude of zero respectively. The black arrows indicate the direction of the electric vector underneath the rods. The insets show a schematic representation of the charge distribution on the grating.

of the substrate and the hole array, as observed in Fig. 4.14 (c). It is also of note that the field distribution along the rods switch direction (indicated by the black arrows) such as to remain charge neutral, since they are now each isolated electrically from the substrate. Once again a schematic representation of the charges on the grating is shown in the inset of Fig. 4.14 (c). It is not possible for the substrate to keep the same charge beneath the rods when electrical contact between the grating and hole array is broken, a requirement to support mode (B), therefore the upper band edge is not observed in the response of the structure when a gap exists between the substrate and grating.

4.4.4 Experimentally achieving Electrical Connection

Modelling of the system discussed in Section 4.4.3 (i.e. coupling-in grating placed over the dielectric regions of the hole array) showed that it was pertinent to consider the effect that gaps between the hole array and coupling-in grating have on the modes supported by the hole array. The predicted broad deep mode (labelled mode (B) Fig. 4.11 and Fig. 4.15) close to the cutoff of the holes was not experimentally characterised and further modelling revealed that an electrical connection between the hole array and coupling-in grating was necessary to observe this mode. It can be concluded therefore that an alternative method to simply placing the coupling-in grating on the hole array to ensure that the two components of the system are in electrical contact is required.

The experiment was repeated using a conducting paste in between the grating and hole array at each point where the grating lay over a metallic region of the hole array. Not only was the desired position of the rods maintained since the paste acted as an adhesive, but more importantly an electrical connection between the two components was achieved. The resulting azimuthal (ϕ)-dependent reflectivity response of the structure to TM-polarised radiation incident at $\theta = 30^\circ$ is shown in Figure 4.15 (a). Here dark and light regions correspond to low and high reflectivity, respectively. Below the fundamental resonance of the hole (red dashed line for a hole of infinite length), the predicted broad dark band (labelled mode (B)) is now experimentally observed. Note this mode is only observed at low azimuthal angles, since at higher angles the coupling-in grating is acting as a wire-grid polariser. The predicted reflectivity response (solid red curve) together with the new data in which a conducting paste has been used between the grating and hole array (circles) is shown in Figure 4.15 (b). Further modelling reveals that a more accurate fit to the experimental data can be achieved when the coupling-in grating is placed at a position of $3a/10 : 7a/10$ in the calculations (red dashed curve). It is of note that the ability to 'switch off' this broad deep mode simply by creating an ultra-subwavelength gap (10 μm) between the hole array and coupling-in grating is particularly surprising.

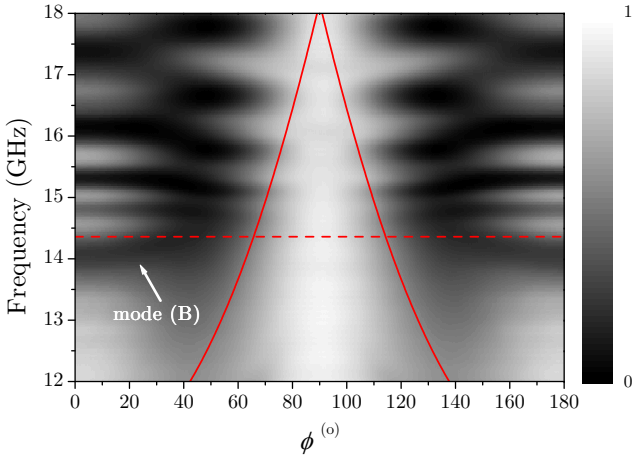

(a)

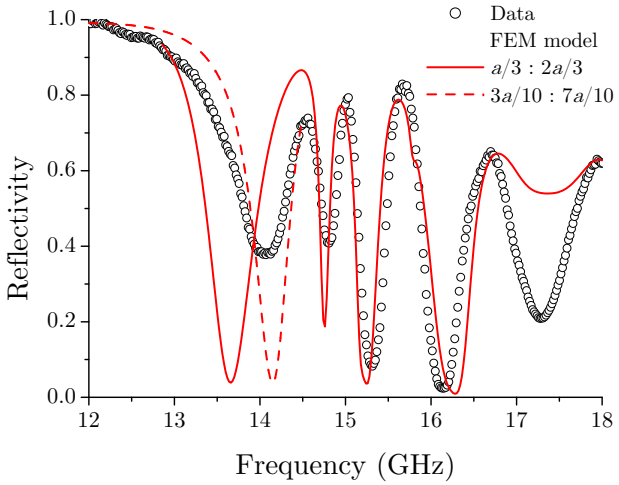

(b)

Figure 4.15: (a) TM-polarised experimental azimuthal (ϕ)-dependent reflectivity response (grey scale) of hole array and metallic coupling-in grating to radiation incident on the sample at $\theta = 30°$, plotted on a linear scale from 0 to 1. Light and dark regions correspond to high and low reflectivity, respectively. The coupling-in grating is formed from rods of uniform circular cross-section, radius $r = 1.6$ mm, and is placed on top of the voids(holes) of the substrate at a periodicity $2d$. The red dashed line represents the cutoff frequency of a single, isolated guide of infinite length and the solid red lines the first order diffracted light lines. (b) Predicted reflectivity response when the rods are positioned at $a/3 : 2a/3$ (solid red curve) and $3a/10 : 7a/10$ (red dashed curve), together with the new data in which a conducting paste has been used between the grating and hole array (circles).

4.5 Predictions to Change the size of the Band Gap

4.5.1 Position of the Coupling-In grating in the xz-plane

In Section 4.4.3 and 4.4.4 it was shown that two modes were observed below the fundamental localised resonance of the holes in the azimuthal(ϕ)-dependent reflectivity response of the structure (i.e. coupling-in grating placed over the dielectric regions of the hole array) to TM-polarised radiation incident at a fixed polar angle ($\theta = 30°$). These were associated with the upper and lower band edges of the band gap in the surface wave dispersion relation. In this section it will be shown that the size of this band gap (at $k_x = 0$) can be controlled by changing the position of the coupling-in grating in the xy-plane at the top interface of the hole array, whilst ensuring that each rod remains over the dielectric regions of the substrate and the $2d$ periodicity of the grating is maintained. Thus far, when investigating the modes supported by the hole array when the coupling-in grating is placed over the dielectric regions of the substrate, the grating has been placed at only a single position, each rod has been centred at $a/3 : 2a/3$ or $33 : 66$ as a percentage of the width of a single hole. However this positioning is arbitrary, as long as the rods are not centred over every hole (i.e. $a/2 : a/2$) such as to destroy the $2d$ periodicity, the position of the rods with respect to the hole array in the xy-plane at the top interface of the hole array can be changed. The predicted dispersion, obtained using the eigenmode solver in HFSS, of the surface modes supported by the hole array below the fundamental resonance of the holes (red dashed line) when the rods (radius $r = 1$ mm) are placed at three different positions over the dielectric regions of the substrate, when radiation is incident in the plane containing the grating vector ($\phi = 0°$) are shown in Figure 4.16. The black and red squares represent the dispersion of the lower and upper band edge respectively. Figure 4.16 (a) shows the predicted dispersion of the surface waves supported by the hole array when the rods are positioned at $25 : 75$, and $30 : 70$ and $40 : 60$ in Figure 4.16 (b) and (c), respectively. The biggest perturbation to the fields associated with the surface mode, i.e. the largest band gap at $k_x = 0$, is achieved when the rods are positioned closest to the centre of the holes. This can be understood by considering that the largest difference in energy between the two energy solutions would occur when the coupling-in grating is placed at a position closest to $50 : 50$.

4.5.2 Radius of Coupling-In Grating

In this section it will be shown that the size of the band gap at normal incidence can also be controlled by selecting the radius of the rods forming the coupling-in grating. It is not too surprising that a larger band gap will be induced by rods with a larger radius since they will act as a greater perturbation to the fields associated with the

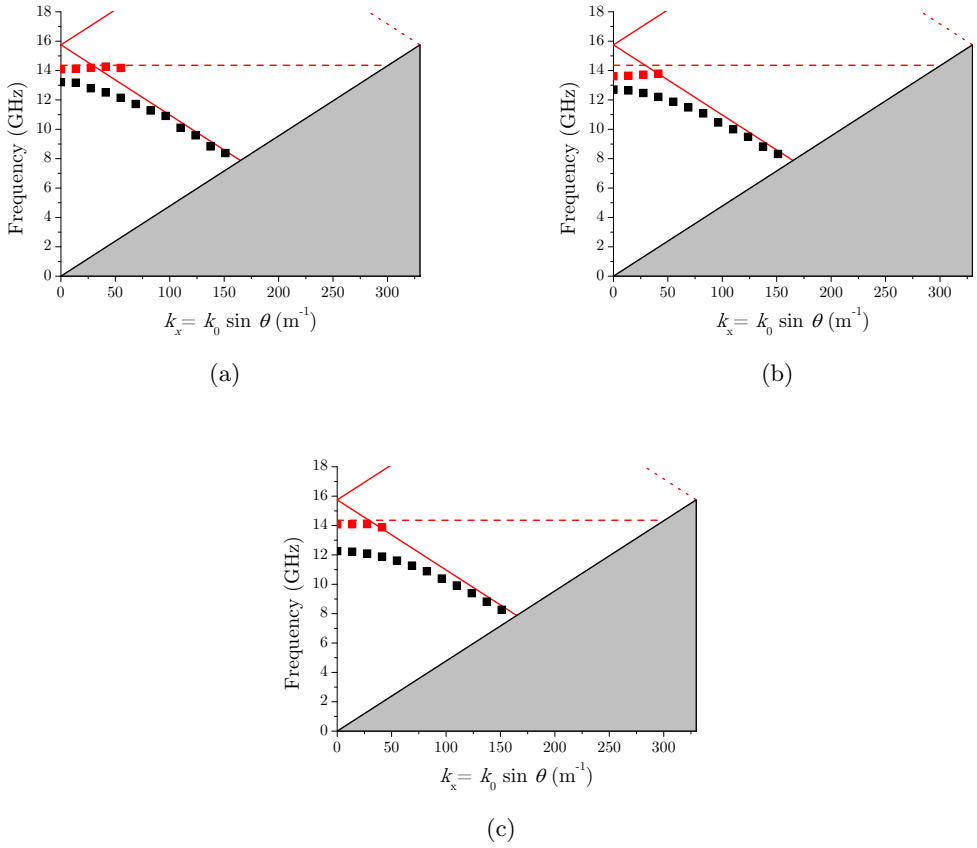

Figure 4.16: Predicted eigenmodes associated with the upper (red squares) and lower (black squares) band edge of the surface supported by the hole array structure when metallic rods of radius $r = 1$ mm, pitch $2d$, are centred at (a) $25:75$ (b) $30:70$ (c) $40:60$ as a percentage of the width of the holes, on the top interface of the hole array. The red dashed and solid curves represents the cutoff frequency of a single, isolated hole of infinite length and first-order diffracted light lines respectively.

surface mode supported by the structure. The predicted dispersion of the surface modes supported by the hole array below the fundamental resonance of the hole (red dashed line), when radiation is incident on the sample in the plane containing the grating vector, when rods of circular cross-section of radius $r = 1$ mm, $r = 2$ mm and $r = 3$ mm are positioned at $a/3 : 2a/3$, are shown in Figure 4.17 (a) - (c) respectively. Of note is the unusually flat-banded nature of the lowest band edge (black squares Fig. 4.17 (c)) when $r = 3$ mm. The dispersion for an equivalent system but with rods formed from glass rods (characterised by a permittivity of 5.5) of radius $r = 1$ mm, $r = 2$ mm and $r = 3$ mm is shown in Figure 4.17 (d) - (f), respectively. The striking difference between the dispersion of the modes in a system comprising a metallic grating compared to a dielectric one, is that no band gap is observed in the dispersion of the modes diffractively

coupled by a dielectric grating. Whilst the upper branch of the band gap remains pinned close to the cutoff frequency of the holes and the lower branch reduces in frequency with increasing radius of the metallic rods, no difference in energy at $k_x = 0$ is predicted between the two modes observed in the system comprising a dielectric grating. Further, the frequency at which these two modes approach the Brillouin zone boundary at $k_x = 0$ decreases in frequency with increasing radius. This can be understood since due to the strong localisation of the fields of the surface wave at the interface between the hole array and grating, the frequency at which the mode is supported is extremely sensitive to the dielectric function of the medium adjacent to the top surface of the hole array. As the radius of the rods increases, effectively the dielectric coupling-in grating acts as a dielectric over-layer with increasing thickness, such as to reduce to frequency at which the surface modes are supported [77–79].

4.5.3 Dielectric Coupling-In Grating

The azimuthal (ϕ)-dependence of the two surface modes diffractively coupled by a dielectric grating placed over the dielectric regions of the hole array, discussed in section 4.5.2 is experimentally characterised. Comprising rods of circular cross-section, radius $r = 1.82$ mm, pitch $\lambda_g = 2d$, which extend the width of the sample, the coupling-in grating is positioned at $a/3 : 2a/3$. Figure 4.18 shows the measured reflectivity response (grey scale) of the structure to TM-polarised radiation incident on the sample at $\theta = 30°$. Light and dark regions correspond to high and low reflectivity, respectively. The coupling strength to the two modes (dark bands) observed below the fundamental localised resonance of the holes (red dashed curve) and following the first order diffracted light line (solid red curve) is shown to be highly dependent on the azimuthal angle at which radiation is incident on the sample. The predicted instantaneous vector electric fields associated with these two modes are shown in Figure 4.18. Note these fields have been obtained using the eigenmode solver in HFSS and corresponds to the modes supported at $\phi = 0°$ and $\theta = 0°$. The field distribution associated with the lower frequency mode (Fig. 4.18 (b)) closely resembles that of the modes observed when metallic rods were placed on the metallic regions of the hole array. Regions of strongest field are located directly above the metal regions (highlighted grey) and the field-line loops are surface plasmon-like in character. The character of the highest frequency mode (Fig. 4.18 (c)) is somewhat different, horizontal fields exist over the metallic regions (highlighted grey), whilst maximum field enhancement is observed above the dielectric rods. Further modelling (not shown) reveals that unlike for a metallic coupling-in grating, the observation of the highest frequency mode is not dependent on ensuring that electrical connection is maintained between the substrate and coupling-in grating, however there is a slight shift up in frequency when the structure is disconnected. This perturbation can be

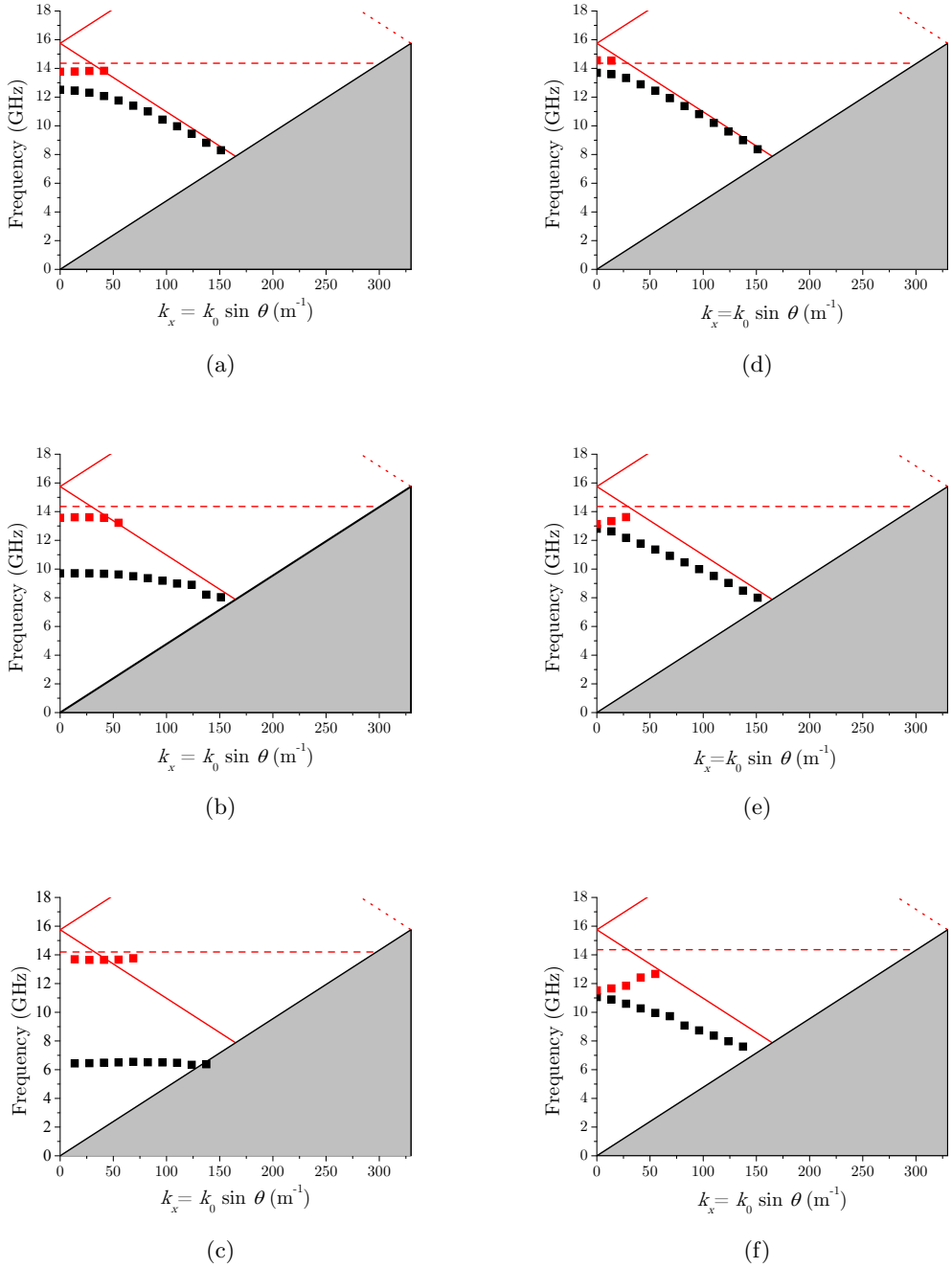

Figure 4.17: Predicted eigenmodes associated with the upper (red squares) and lower (black squares) band edge of the surface supported by the hole array structure when metallic rods of radius (a) $r = 1$ mm, (b) $r = 2$ mm and (c) $r = 3$ mm, pitch $2d$ are centered at $a/3 : 2a/3$ over the dielectric regions on the top interface of the hole array. The equivalent plots but for a coupling-in grating formed from glass rods of radius (d) $r = 1$ mm, (e) $r = 2$ mm and (f) $r = 3$ mm are also shown. The red dashed and solid curves represents the cutoff frequency of a single, isolated hole of infinite length and first-order diffracted light lines respectively.

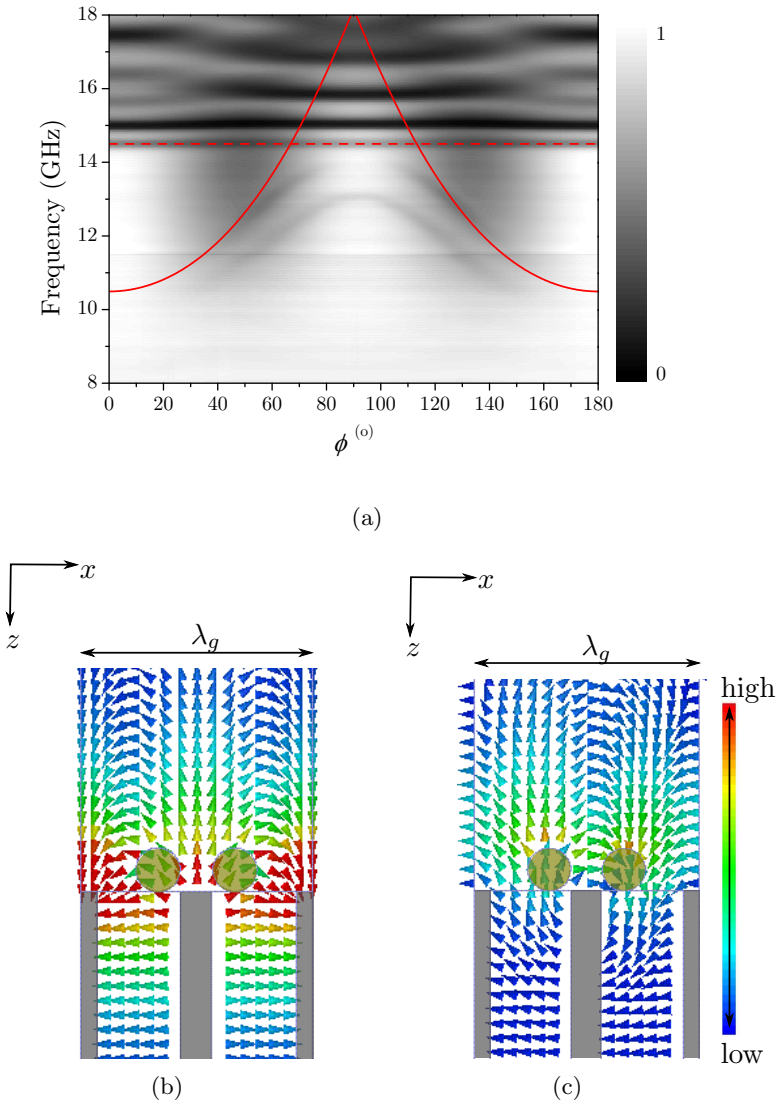

Figure 4.18: Experimental azimuthal (ϕ)-dependent reflectivity response (grey scale) of hole array and metallic coupling-in grating to TM-polarised radiation incident at $\theta = 30°$, plotted on a linear scale from 0 to 1. Light and dark regions correspond to high and low reflection respectively. The coupling-in grating is formed from glass rods of uniform circular cross-section, radius $r = 1.82$ mm, and is placed on top of the voids (holes) of the hole array, at a periodicity $2d$ at the position $a/3 : 2a/3$. The red dashed line represents the cutoff frequency of a single, isolated guide of infinite length and the solid red lines the first order diffracted light lines. Predicted instantaneous vector electric fields plotted in the xz-plane associated with the (b) lower and (c) upper band edge of the band gap in the surface wave dispersion at $k_x = 0$ when $\phi = 0°$. Red and blue regions correspond to a high and field magnitude of zero, respectively.

attributed to the grating having less of a perturbation to the fields associated with the surface mode when the grating and hole array are not in contact.

4.6 Conclusions

In this chapter it has been shown that when using grating-coupling techniques to couple incident radiation to surface waves supported by a structure with a periodicity comparable to the wavelength of the probing radiation, the relative position of the two components is significant; a key issue not discussed in the literature, when investigating pseudo-plasmonic surfaces in the microwave regime. In this chapter, this issue has been addressed by investigating the azimuthal-dependence of the surface modes supported by a hole array structure when a coupling-in grating has been placed at different positions with respect to the hole array. Of particular note is the ability to 'switch off' a broad deep mode in the response of the structure when a metallic grating is placed over the dielectric regions of the hole array, by breaking electrical contact between the substrate and grating. Further it has been shown that a dielectric grating can also be used to diffractively couple incident radiation to the supported surface modes, with a gap between the grating and hole array predicted to be less critical.

Chapter 5

Structurally-Dictated Anisotropic Surface Waves on a Rectangular Hole Array

5.1 Introduction

In this Chapter, structurally-dictated surface waves supported by a near perfectly conducting substrate pierced by a close-packed array of deep, rectangular holes is characterised. In this arrangement, unlike in Chapter 4, the fundamental resonance in the holes in the orthogonal directions is different, and the frequency therefore to which the dispersion of the surface waves supported by the structure is limited, varies with sample orientation. The anisotropic dispersion resulting from an ellipsoid of limiting frequencies, is directly mapped utilising blade-coupling techniques to excite the modes and by phase resolved measurements to determine their dispersion. Furthermore, by exploiting the anisotropy of the unit cell, the family of higher order surface waves associated with the quantisation of the electromagnetic fields within the holes is also explored.

5.2 Background

It is intrinsically difficult to induce an anisotropic response from a naturally occurring planar metallic structure. However, the concept of strongly bound 'spoof' or 'designer' surface waves, introduced by Pendry *et al.* [3] in 2004, and the subsequent wealth of studies confirming their existence such as those reported in [2, 4, 6, 26, 32, 56, 58, 71, 80] suggest it is possible to select specifically designed anisotropic electromagnetic properties, simply by choosing the desired symmetry of the structure.

In this chapter, the concept of pseudo-plasmonic surfaces at microwave frequencies is extended to include structures with a high degree of surface anisotropy. Structurally-

dictated anisotropic 'spoof' or 'designer' surface waves on a near perfectly conducting metal surface pierced by a rectangular array of close-packed, deep rectangular holes is characterised. Due to the rectangular geometry of the holes, the fundamental resonance of the structure in orthogonal directions, and therefore the frequency to which the dispersion of the surface wave is limited (as discussed in Chapter 2) is substantially different. This is in contrast for instance, to the optical study of Feng *et al,* [81] on an anisotropic plasmonic metamaterial which is formed from a periodic two-dimensional array of nanoholes in a thin metal film with differing periodicities in the orthogonal directions. The anisotropy in Feng *et al.'s* study is associated primarily with diffraction (i.e. periodicity of the rectangular lattice) that strongly perturbs the dispersion of the surface mode without any variation of the limiting frequencies. The structure is analogous to an optical birefringent crystal where the optical anisotropy originates from atomic scale dipole moments that vary in space depending on the crystal lattice. The constructed artificial form birefringement metal in Ref. [81] demonstrates different polarisabilties along different optical axes, thus leading to optical anisotropy of excited surface waves (SPPs).

For a hole with rectangular cross-section of side length $a\hat{\mathbf{x}}$ and $b\hat{\mathbf{y}}$, there are *two* distinct cutoff frequencies. These correspond to the TE_{10} waveguide modes, the predicted time-averaged electric field profiles of which are shown in Figure 5.1 (a) and (b), for an electric field polarised along the y- and x- axes respectively. Red regions correspond to high field enhancement and blue to a field magnitude of zero. The surface asymmetry of the rectangular hole array studied in this chapter provides an additional degree of freedom in the manipulation of designer surface waves. Whilst the width of the hole in one direction (i.e. $a\hat{\mathbf{x}}$) dictates the resonant frequency for an incident polarisation (electric vector) directed along the y-direction, the pitch in the orthogonal direction (i.e.$\lambda_b\hat{\mathbf{y}}$) dictates the onset of diffraction. Hence, it is possible to independently control these two frequencies and tailor the geometry of the unit cell to separate these two limits. This allows for the excitation and observation of the higher order surface waves in the non-diffracting region.

Furthermore, in addition to the lateral quantisation of the field within the hole, the field is also quantised along the depth of the hole, and a family of surface modes can be supported, each associated with a depth-quantised hole resonance. Previous investigations into the dispersion of these higher order modes had been purely limited to theoretical studies on periodically structured metal surfaces formed from groove cavities [82], and finite depth square [83] and rectangular cross-section holes [31]. In these studies it was shown that each band is associated with a resonant mode of the cavity, resulting from a quantisation of the field along its length. However, more recently the experimentally measured multi-modal transmission through a square array of circular

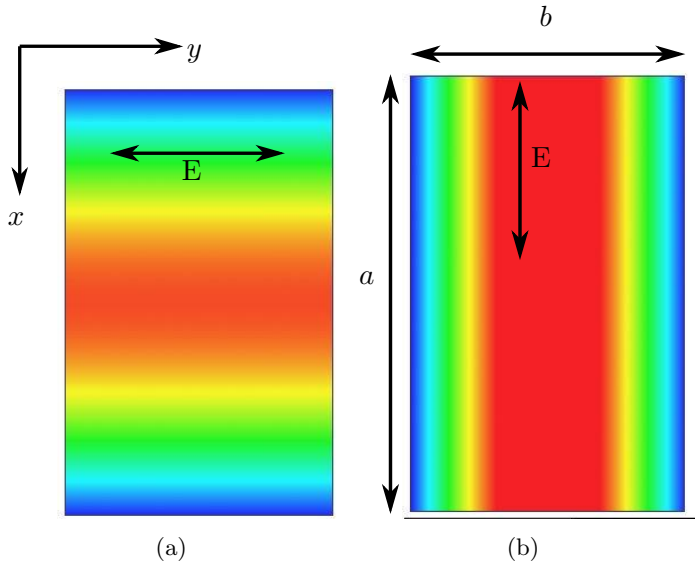

Figure 5.1: Predicted time-averaged electric-field profiles of TE_{10} waveguide modes supported by a waveguide with rectangular cross-section for electric field polarisations directed along the (a) y- and (b) x- axes.

holes [84] has been reported, as well as a family of TM surface waves on a square array of square cross-section pillars [69] which are asymptotic to frequencies defined by the pillar height (slits) and refractive index of material filling the slits. In addition to the anisotropy discussed above, we are able to experimentally report the observation of a similar family of modes.

Due to the non-radiative nature of the surface modes supported by the structure, as discussed in Chapter 2, a suitable mechanism for wave-vector matching to free space radiation is required for the excitation of the aforementioned modes. Whilst in the previous chapter, a grating coupling technique was employed to couple free-space radiation to the surface modes supported by the structure, blade-coupling techniques as described in Section 3.2.3, are utilised in this chapter. When combined with phase-resolved measurements, the technique allows for the direct measurement of the dispersion of the supported surface waves in the *non-radiative* regime.

5.3 Experimental Sample

The experimental sample is comprised from an array, approximately 350×350 mm in size, of wax-filled ($\epsilon_h = 2.25$) closed-ended rectangular brass tubes. The unit cell (Fig. 6.1) is formed from a single rectangular element of size $\lambda_a = 9$ mm and $\lambda_b = 6$ mm in the $\hat{\mathbf{x}}$ and $\hat{\mathbf{y}}$ directions respectively. Whilst the pitch of the structure dictates the frequency of the onset of diffraction, it is the inner dimensions of the tubes, $a = 8$ mm and $b = 5$ mm, together with the refractive index, $n = \sqrt{\mu_h \epsilon_h}$, where μ_h and ϵ_h are

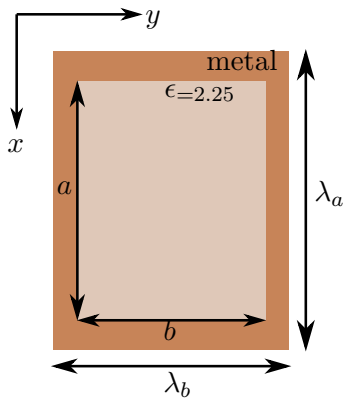

Figure 5.2: Schematic representation of the unit cell. The long pitch of the tube $\lambda_a = 9\,\text{mm}$ and the orthogonal shorter pitch $\lambda_b = 6\,\text{mm}$ the inner dimension of the hole are $a = 8\,\text{mm}$ and $b = 5\,\text{mm}$.

the relative permeability and permittivity respectively) of the material filling the hole, which determine the fundamental resonances of the system. For a guide of infinite length this resonance is determined by the cross-section of the hole. This cutoff frequency is determined by equations 5.3.1 and 5.3.2 for electric field polarisations directed along the y- and x- axis respectively.

$$\nu_a = \frac{c}{2a\sqrt{\epsilon_h \mu_h}} \tag{5.3.1}$$

$$\nu_b = \frac{c}{2b\sqrt{\epsilon_h \mu_h}} \tag{5.3.2}$$

However, in the present work, the tubes are of finite length, $h = 30$ mm, thus the fundamental modes supported by the tubes are shifted upwards in frequency above the cutoff of an infinite length tube due to the additional quantisation (approximately odd-integer quarter-wavelengths) along the tube length in the z-direction [6].

5.4 Experimental Techniques

Blade-coupling techniques and phase resolved measurements are employed to couple TM-polarised radiation (8 GHz $\leq f \leq$ 40GHz) to surface modes in order to directly map out their dispersion (further details can be found in Section 3.2.3). However, in addition to recording the phase information, which is used to characterise the dispersion of the supported modes, it is also useful to measure the magnitude of the signal detected by the microwave horn on the opposite side of the sample. Figure 5.3 (a) shows the magnitude (black curve) plotted on a linear scale and group delay(red curve), which is derived from the measured phase information of the signal (plotted in arbitrary units) measured at the second 'detector' microwave horn when the plane of incidence contains

the short axis ($\phi = 0°$). A series of peaks is observed in both the magnitude and group delay data, which can be attributed to the family of surface modes (labelled N= $0 - 6$ Fig. 5.3) supported by this structure. The magnitude of the signal associated with the fundamental surface mode (N= 0) is initially relatively high in the region where the group delay has a relatively constant gradient and the dispersion of the mode closely follows the light line. The strength of the signal drops sharply within a frequency range defined by the width of the group delay peak. Within the peak of the group delay, the magnitude of the signal is more comparable to the magnitude of the peaks of the higher order surface modes, the strength of which, with increasing order (N), decreases. Note the magnitude of the signal associated with the higher order modes (N $>$ 0) is significantly less than that associated with the fundamental mode, this is due to the dispersion of the higher modes being close to being flat-banded.

On comparison of the position of the peaks in the magnitude and group delay data, it is clear they do not coincide, with the peaks in group delay occurring at a higher frequency than that of the magnitude data. To understand this behavior it is important to establish first what physical mechanism causes a peak in the group delay signal but more fundamentally what group delay (τ) is a measure of. Qualitatively it is the negative slope of the phase response, and is a derived quantity from the phase measurements, formally it can be written as

$$\tau(\omega) = \frac{-\partial\phi(\omega)}{\partial\omega} \tag{5.4.1}$$

where ϕ is the phase in radians and ω the frequency in radians/second. For a non-dispersive system, group delay is not a function of frequency but constant. However dispersive systems (like the one discussed in this chapter) have a non-linear phase versus frequency response. A maximum value of group delay is reached when the phase of the recorded signal is changing most rapidly with respect to frequency. A flat portion of the group delay curve is equivalent to the part of the dispersion curve where the mode has a constant gradient, which in this system would correspond to where the gradient of the mode matches that of the light line. A peak in the group delay curve is indicative of the mode travelling at it's slowest, theoretically this would occur at the Brillouin zone boundary where a standing wave condition is reached and the peak would be of infinite height (as the signal would be infinitely delayed). Experimentally this condition is not met, and the measured peak has a finite height and width (attributable to the width of the mode, due to the losses in the system.)

The phase data (green curve), which is characterised by a saw tooth oscillation and is continuously measured as a function of frequency between $-\pi$ to $+\pi$, together with the magnitude (black curve) and group delay (red curve) is plotted on the same

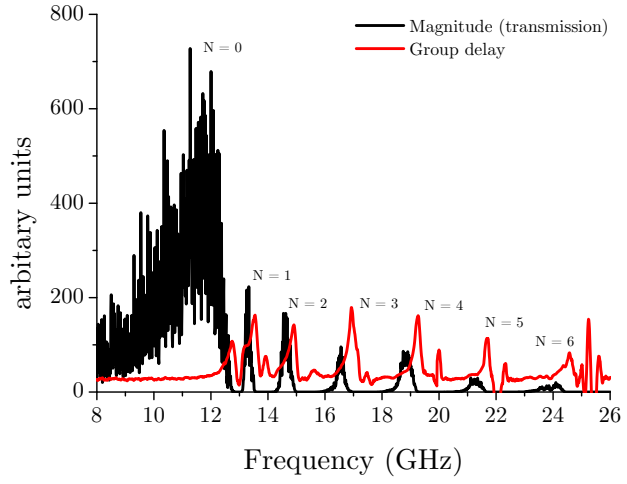

(a)

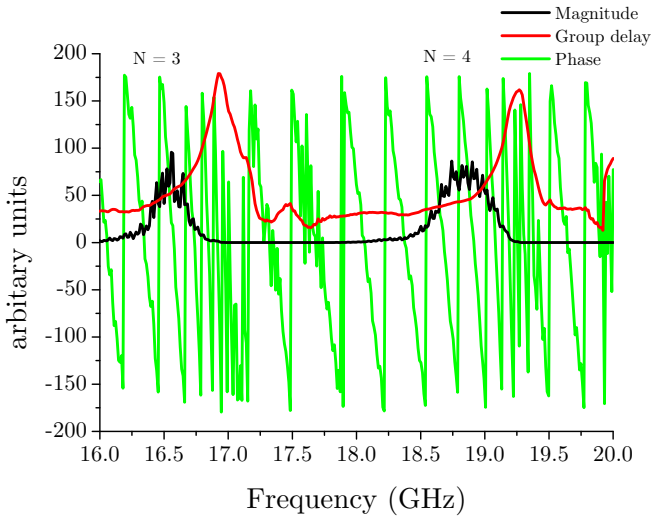

(b)

Figure 5.3: (a) Magnitude (black line) and group delay (red line) of the signal (plotted in arbitrary units) detected by the second microwave horn when radiation is incident on the sample in the plane containing the short axis, λ_b ($\phi = 0°$). (b) Magnitude (black line), group delay (red line) and phase (green line) of the signal detected by the second microwave horn when radiation is incident on the sample in the plane containing the short axis, λ_b ($\phi = 0°$) for the N = 3 and N = 4 order surface mode, plotted in arbitrary units.

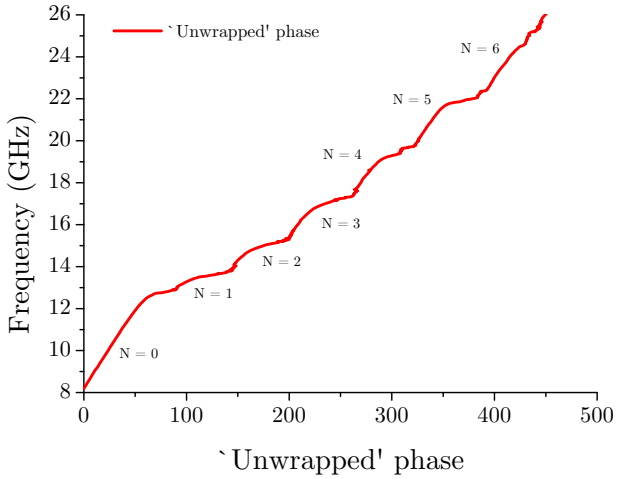

Figure 5.4: 'Unwrapped' phase information as a function frequency associated with the first seven modes (labelled $N = 0 - 6$) supported by the hole array structure when the plane of incidence contains the short axis.

scale for ease of comparison for the N = 3 and N = 4 order surface modes (Figure 5.3 (b)). In between the resonances no surface mode is supported by the sample, therefore the magnitude of the signal detected at the second microwave horn is zero. As such, the phase information recorded in between the frequencies at which surface modes are supported is simply noise, and the data over this frequency range must be discarded. The 'clean' phase information, recorded at frequencies corresponding to where a surface mode is supported by the sample, needs to be extracted. Each time a resonance is passed through, the information about where the dispersion of the mode should commence with respect to the light line is lost, hence the requirement for the phase measurements to be taken at two different values of L, i.e. separation between the blades (as discussed in Section 3.2.3). Note the recorded phase information is 'unwrapped' for use in this analysis; the 2π saw tooth oscillations (as shown by the green curve in Fig. 5.3) are summed when the data is processed. The resulting phase as a function of frequency after this 'unwrapping' process is shown in Figure 5.4. Figure 5.4 also illustrates that the data is measured as a continuous function of frequency.

Since the data is recorded as a continuous function of frequency, it is necessary to establish a method in order to obtain discrete sets of data which uniquely correspond to each mode and a criteria must be established to extract the 'clean' phase information in the final analysis of data which contains multiple modes. By examining the oscillations of the phase of the recorded signal as a function of frequency, the dispersion of each surface mode can be tracked. The frequency of the oscillations associated with the recorded phase information increasing (green curve Fig. 5.3 (b)), is indicative of the velocity of

the surface mode decreasing. The highest frequency oscillation occurs within the peak of the group delay data (red curve Fig. 5.3 (b)). It is noted that this occurs in the high-frequency wings of the peak in magnitude of the signal (black curve Fig. 5.3 (b)), thus showing that as long as there is even a relatively small amount of signal, 'clean' phase information associated with a surface mode can still be recorded. The data is terminated at a frequencies corresponding to the highest frequency oscillation. At frequencies when the recorded phase data becomes 'clean' again, the corresponding signal is associated with the next order mode. This method is applied to each of the surface modes to obtain discrete sets of data that can be used to characterise the dispersion of each individual mode. In order to correctly determine the position of the higher order modes in k-space however, the dispersion is actually calculated using a modified version of equation 3.2.3, which has an additional $2\pi n$ term.

$$k_x = \left(\frac{\Delta\phi + 2\pi n}{\Delta L} + k_0 \right). \tag{5.4.2}$$

This allows the mode to be moved by integer (n) multiples of 2π, since for the higher order modes their position with respect to the light line is unknown.

5.5 Experimental Results

5.5.1 Dispersion of Surface Waves at $\phi = 0°$

Initially, TM-polarised radiation impinges on the sample surface with the incident plane containing the short pitch of the structure λ_b ($\phi = 0°$). In this arrangement the family of surface modes associated with the quantisation of the field within the holes along the x-axis (Fig. 5.1 (a)) can readily be measured in the non-diffracting regime. This is because the onset of diffraction occurs at 25.0 GHz, significantly above the fundamental resonance of the holes, which for a single, isolated guide of infinite length is defined by equation 5.3.1, $\nu_a = 12.5$ GHz, (horizontal red dashed line Fig. 5.5). However this frequency is modified upwards due to the additional quantisation of the field along the length of the guide for a finite length tube. Figure 5.5 shows the measured dispersion (circles), together with the predicted eigenmode solutions associated with each mode from the FEM modelling (crosses), they show excellent agreement. The zeroth order surface mode (N = 0) asymptotically approaches the fundamental resonance of the hole, and six further higher order modes (N = 1-6) are observed in the non-diffracting regime. The predicted electric field profiles of which, plotted at the Brillouin zone boundary ($k_y = \frac{\pi}{\lambda_b} = 525\text{m}^{-1}$), in the yz-plane, are shown in Figure 5.6 (a)-(f) for N = 1-5 respectively. Here red regions correspond to regions of highest field strength. Each surface mode in this family is associated with a quantisation of the fundamental waveguide

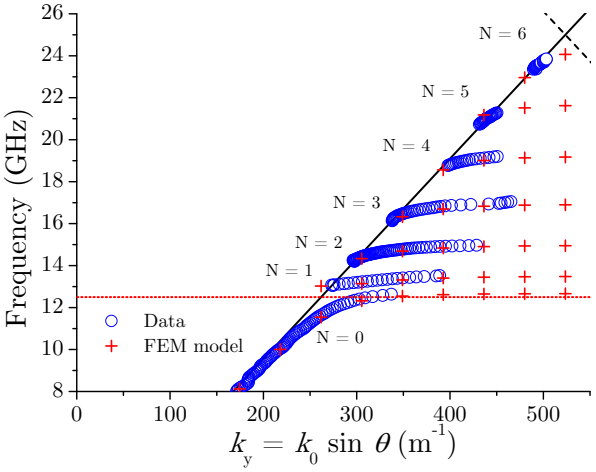

Figure 5.5: Experimentally measured dispersion (circles) together with predicted eigenmode solutions (crosses) of the family of surface modes when the plane of incidence contains the short pitch of the structure ($\phi = 0°$). The black dashed and red dashed lines represent the first-order diffracted light line and cut-off frequency of the single, isolated guide of infinite length, respectively. The solid black line is the light line.

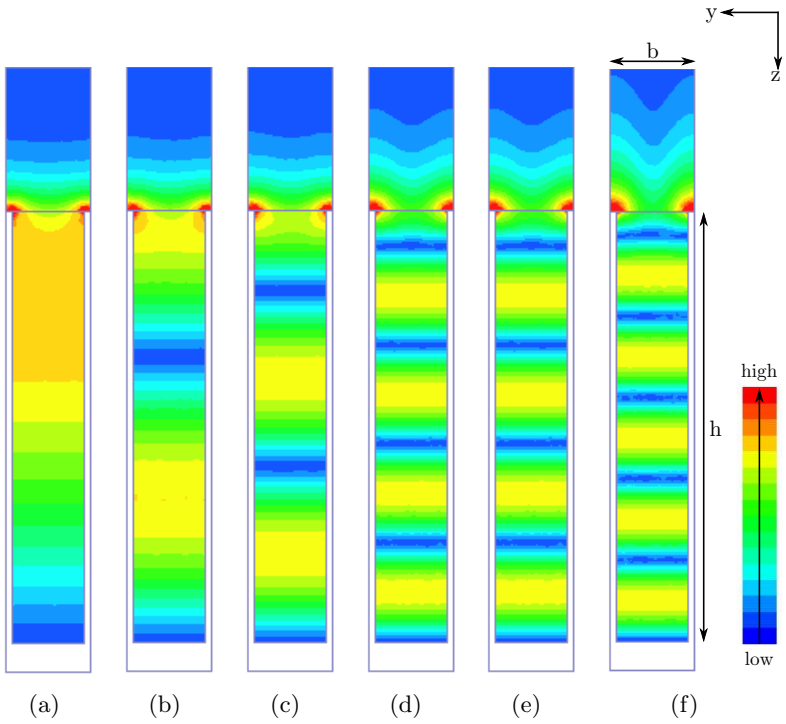

Figure 5.6: Predicted time-averaged electric-field profiles of the (a) N = 0 (b) N = 1 (c) N = 2 (d) N = 3 (e) N = 4 and (f) N = 5 order surface mode associated with the ν_a fundamental resonance of the guide, plotted at the Brillouin zone boundary ($k_y = \frac{\pi}{\lambda_b} = 525\mathrm{m}^{-1}$) in the yz-plane. Red regions correspond to the highest field enhancement and blue to a field magnitude of zero.

mode (TE_{10}) in the $z-$direction, and it is the frequencies of these resonances which define upper limits for the respective bound surface modes, with each mode located in between neighbouring resonant frequencies. The group velocity of each mode diminishes rapidly with increasing wavevector, tending to zero as it asymptotically approaches its limiting frequency. For the majority of modes however (Fig. 5.5), the signal strength at higher wavevectors is sufficiently weak that they cannot be well characterised. In particular higher order modes, where the gradient of the mode is changing most rapidly and are closer to the onset of diffraction are not as well characterised.

5.5.2 Dispersion of Surface Waves at $\phi = 90°$

The fundamental surface mode is characterised by a dramatically different dispersion when the structure is azimuthally rotated by $\phi = 90°$, such that the plane of incidence now contains the long pitch of the structure (λ_a). In this orientation the fundamental resonance of the hole is increased such that the zeroth order (N = 0) surface mode now approaches its limiting frequency (represented by horizontal red dashed line Fig. 5.7 (a) for a single, isolated guide of infinite length) *above* the diffraction edge (16.0 GHz), it does so while displaying rather limited dispersion. The experimentally characterised dispersion (circles) together with the predicted eigenmode solutions associated with this mode (crosses) when radiation is incident in the plane containing the long pitch (λ_a) are shown in Figure 5.7 (a). The surface mode closely follows the light line (solid black line) and its dispersion is only slightly perturbed away from the light line as it approaches the Brillouin zone boundary, f_{bz} ($k_x = \frac{\pi}{\lambda_a} = 349.1$ m^{-1}) i.e. where the light line and first order in-plane diffracted light line (black dashed line) cross, at approximately 16.0 GHz in the measured data, which is the frequency the sample becomes diffracting. To obtain this dispersion, since only the fundamental mode is of interest and its position with respect to the light line is well known, the relative phase measurement technique as described in Section 3.2.3 is not necessary and the signal associated with this mode is therefore compared to a flat metal sheet.

It is necessary to closely examine the eigenmodes of the system in the region where the light line and first-order in-plane diffracted light line cross. On closer examination of the predicted dispersion (crosses Fig. 5.7 (b)), the expected band gap at the Brillouin zone boundary (as discussed in Section 2.2.3.1) is revealed, a feature which it not obvious in the experimental data. (Note the predicted band gap has been omitted from Fig. 5.7 (a) for clarity). First consider the time-averaged electric fields of the eigenmodes associated with the lower band edge (red crosses Fig. 5.7 (b)) Fig. 5.8 (a)-(d). High fields (red regions) are supported on the metal regions and at $f < f_{bz}$ the mode is only weakly confined to the surface due to the proximity to the light line. With increasing wavevector, the confinement increases as the supported surface mode becomes sensitive

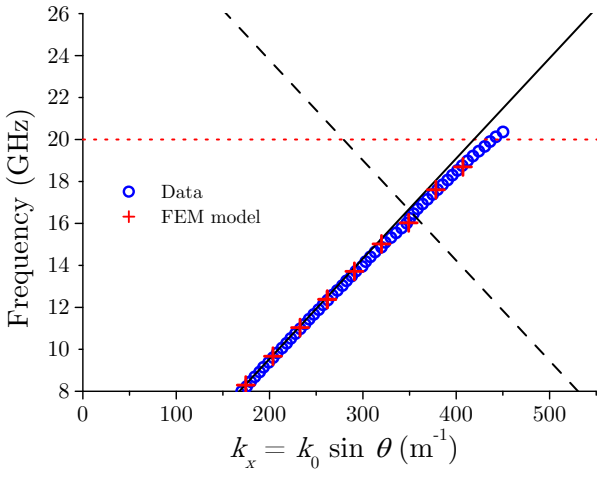

(a)

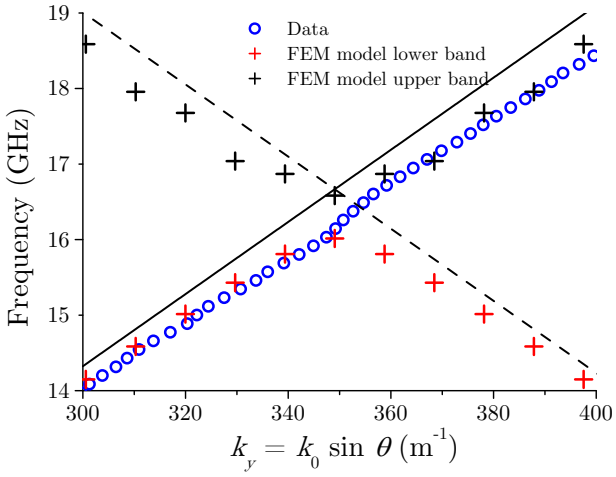

(b)

Figure 5.7: Experimentally measured dispersion (circles) of the fundamental surface mode when the plane of incidence contains the long pitch of the structure ($\phi = 90°$). The black dashed and red dashed lines represent the first-order diffracted light line and cutoff frequency of a single, isolated guide of infinite length, respectively. The solid black line is the light line. The predicted eigenmode solutions for the (a) fundamental surface mode (red crosses) and (b) lower (red crosses) and upper (black crosses) band edge of the fundamental surface mode in the band gap region, are shown.

to the periodicity of the structure and a standing wave condition is reached at the Brillouin zone boundary, f_{bz}. The time-averaged electric fields associated with the two eigenmodes at the Brillouin zone boundary which correspond to the lower and upper band edge are shown in Figure 5.8 (d) and (e) respectively. The two solutions, as

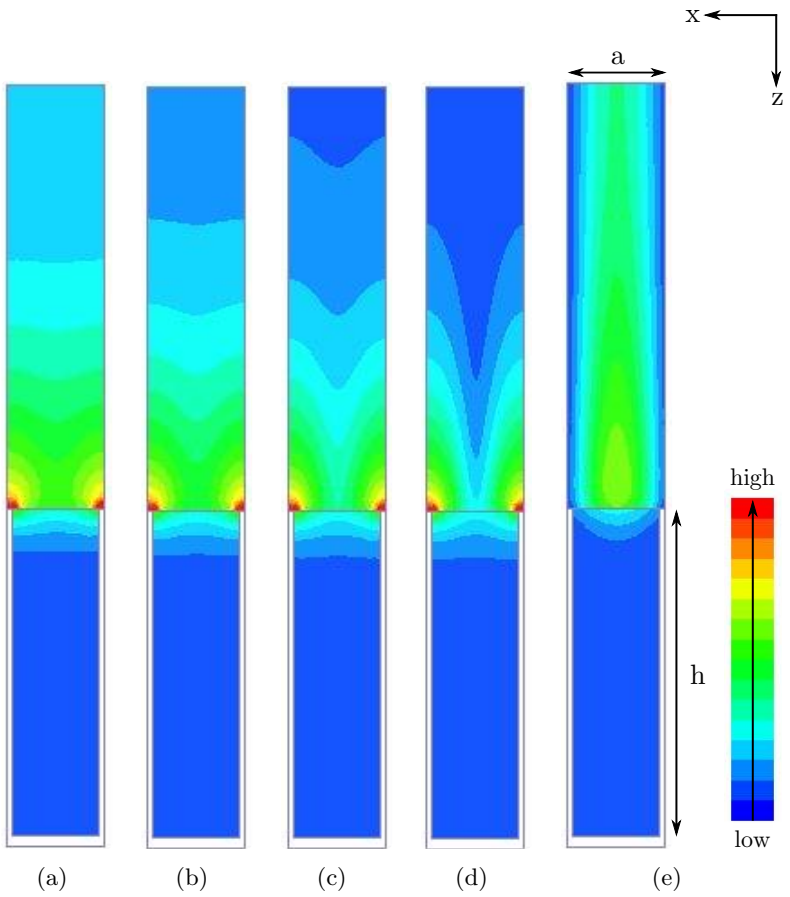

Figure 5.8: Predicted time-averaged electric field profiles of the eigenmode solutions plotted in the xz-plane close to the Brillouin zone boundary $k_x = \frac{\pi}{\lambda_a} = 349.1\text{m}^{-1}$, associated with the lower (a)-(d) (increasing wavector) and upper (e) band edge of the fundamental surface mode in the band gap region. The fields profiles in (d) and (e) correspond to the predicted field profiles at the Brillouin zone boundary for the lower and upper band respectively. Red regions correspond to the highest field strength and blue a field magnitude of zero.

expected are spatially separated by $\lambda_a/2$, with high fields (red regions) predominately over the metal (white regions) for the mode associated with the lower band edge and over the voids (holes) for the higher frequency mode. Also of note is the extent to which the fields extend above the void region for the mode associated with the upper band edge (Fig. 5.8 (e)), a consequence of the proximity of the mode to the diffracting region.

Above, a full description of the eigenmodes in the region of the band gap is presented, it remains to be established though as to why experimentally these features are not fully resolved. Further information can be obtained about the experimentally measured dispersion by examining the magnitude and phase of the signal propagating across the sample. The black and red curves in Figure 5.9 (a) show the magnitude and group delay respectively of the signal detected at the second microwave horn when radiation

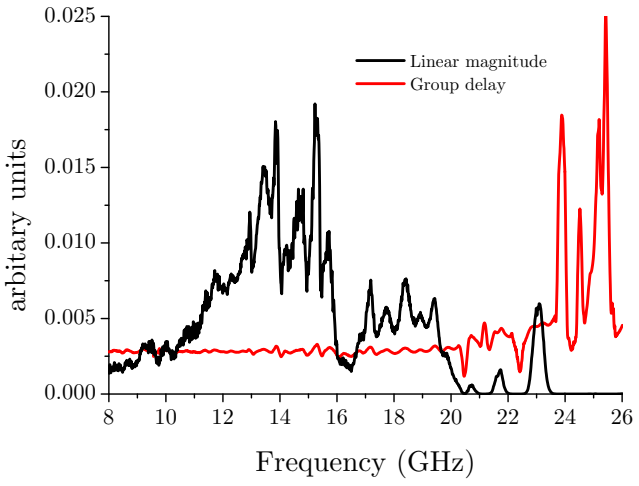

(a)

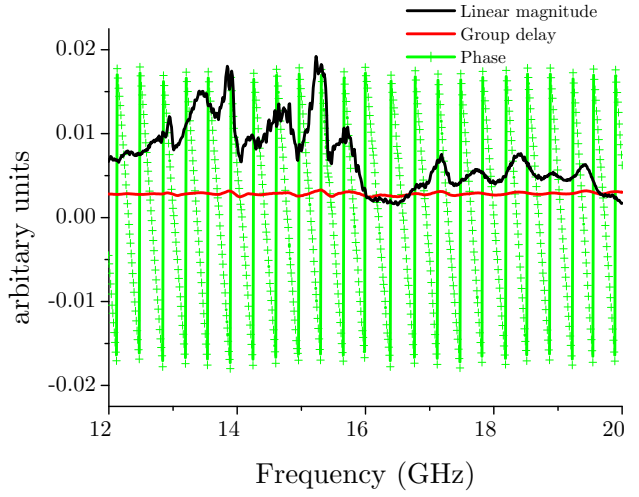

(b)

Figure 5.9: (a) Magnitude (black line) and group delay (red line) of the signal (plotted in arbitrary units) detected at the second microwave horn when radiation is incident on the sample in the plane containing the long axis, λ_a ($\phi = 90°$). (b) Magnitude (black line), group delay (red line) and phase (green line) detected at the second microwave horn when radiation is incident on the sample in the plane containing the long axis, λ_a ($\phi = 90°$) for the N = 0 surface mode, plotted in arbitrary units.

is incident on the sample in the plane containing the long axis (λ_a). It is clear that rather than a single peak, as observed in the magnitude of the signal associated with the fundamental resonance of the system when $\phi = 0°$, in this orientation, a double peak (with peaks centred at approximately 14 GHz and 18 GHz) is observed, caused by a loss of signal around the frequency of the onset of diffraction.

The loss in signal can be attributed to the presence of the band gap at the Brillouin zone boundary ($k_x = \frac{\pi}{\lambda_a}$), however, whilst there is a reduction in signal around 16.0GHz, it does not fall to zero as expected and the phase information (green curve, Fig. 5.9 (b)) is still 'clean' within the forbidden band. Furthermore the gradient of the group delay curve is constant, no peak is observed as expected for a mode approaching the Brillouin zone boundary as described in Section 5.5.1. However, since the width of the mode and the band gap are comparable in magnitude, it is possible that the expected discontinuity in the data would not be observed. Also, if the gradient of the dispersion is changing rapidly, and the step size in frequency (sampling rate) is not sufficiently small, this may also cause the dispersion not to be well characterised in this region. Additionally, as discussed in Section 5.5.1, it is difficult to characterise the flat banded part of the dispersion curves, where the group velocity tends to zero. The strength of the signal does recover at frequencies above the band gap resulting in a secondary peak (which is still associated with the fundamental resonance) however the magnitude of the signal is reduced with respect to the primary peak. This reduction can be attributed to there being another loss channel available for the mode to decay into; since the peak occurs at frequencies above the onset of diffraction, power can be transfered into a diffracted order, and the signal associated with this mode would not be measured by the detecting microwave horn placed directly in line of the emitting horn. Above the fundamental surface mode a series of peaks are observed in the magnitude of the signal (as also seen in the response of the sample to radiation incident on the sample along the orthogonal axis ($\phi = 0°$)) which are associated with the higher order longitudinal quantisations of the fundamental localised resonance supported within each hole.

The group delay data remains relatively featureless across all frequencies associated with the fundamental resonance, no peak is observed at the limiting frequency (dictated by the localised waveguide mode). This behaviour is in contrast to that observed when radiation is incident in the plane that contains the orthogonal shorter pitch, where the frequency of the phase oscillations increase (Fig. 5.3 (b)) and a peak in the group delay signal is observed, indicative of the mode becoming strongly bound to the surface. On closer examination of the phase when $\phi = 90°$ (green curve Fig. 5.9 (b)), this behaviour is not observed and there is no evidence of the group velocity of the mode tending towards zero (as to be expected for a mode approaching the Brillouin zone boundary) it approaches its limiting frequency ($\approx \nu_b = 20.0$ GHz) whilst showing very limited

dispersion.

In addition to the limitations in experimentally characterising the dispersion as described previously, it is important to establish the fundamental differences between the dispersion of the zeroth order surface modes supported by the structure in the two orthogonal directions. When the plane of incidence contains the short pitch of the structure ($\phi = 90°$) the fundamental surface mode approaches its limiting frequency, which is defined by the fundamental localised resonance of the hole at a Brillouin boundary, which is significantly lower in frequency than the onset of diffraction. However, when the plane of incidence is azimuthally rotated so as to contain the long pitch of the structure (λ_a), $\phi = 90°$, the mode approaches the Brillouin zone boundary well below the first localised resonance. In this case the point at which the mode theoretically reaches zero group velocity is now purely defined by the periodicity of the system (as opposed to in addition the first-order localised resonance). Furthermore as it does reach its limiting frequency defined by the fundamental resonance of the system, it does so at a frequency before the next Brillouin zone boundary, the constraint for the mode to be flat banded is simply not there. It is therefore not surprising that the group velocity of the mode does not reach zero at this point.

5.5.3 Azimuthal (ϕ) Dependence of Fundamental Surface Mode

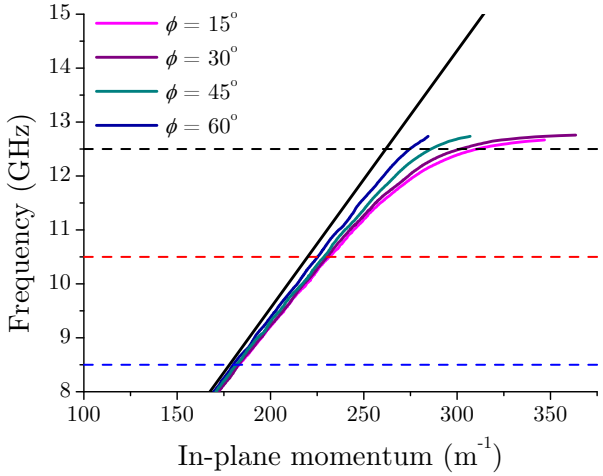

Figure 5.10: Experimentally measured dispersion when the radiation is incident on the sample at the following azimuthal angles $\phi = 15°, 30°, 45°$ and $60°$. The blue, red and black dashed lines correspond to the frequencies of the equi-energy contours in Fig. 5.12.

Recording the azimuthal dependence of the fundamental surface mode by rotating the sample underneath the blade-coupling setup, allows one to generate equi-energy

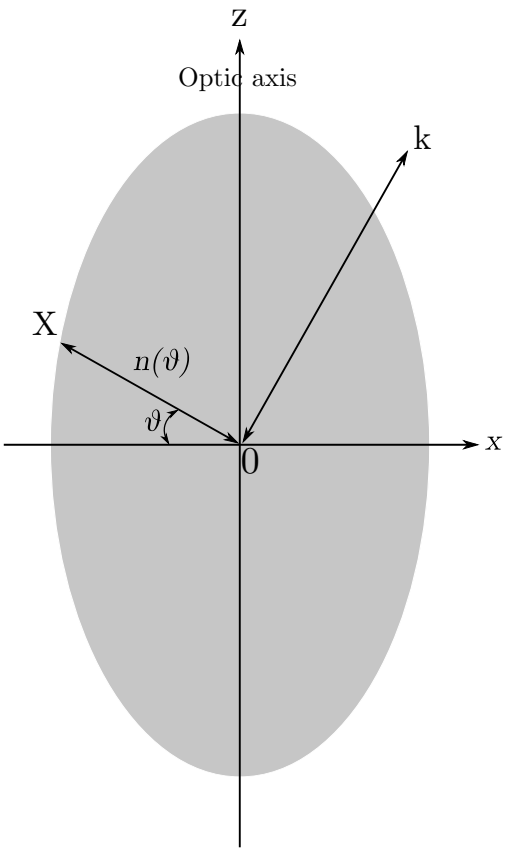

Figure 5.11: Section of uniaxial indicatrix containing the optic axis.

contours which describe the angular dependence of the dispersion of the fundamental surface mode. Since only the fundamental mode is of interest, as its position with respect to the light line is well known and no phase information has been lost by passing through a lower order resonance, the relative phase measurement technique as described in Section3.2.3 is not necessary. The signal propagating across the sample is compared to that from a flat metal sheet. The experimentally measured dispersions when radiation is incident on the sample at the following azimuthal angles $\phi = 15°$ (pink curve), 30°(purple curve), 45° (green curve) and 60° (blue curve), where ϕ is defined with respect to the y- axis measured in the xy-plane, are shown in Figure 5.10. The data had been terminated at frequencies corresponding to where there is no longer 'clean' phase information. The blue, red and black dashed lines at 8.5 GHz, 10.5 GHz and 12.5 GHz respectively represents the frequencies of the equi-energy contours shown in Figure. 5.12, the details of how these plots were obtained is detailed later in this Section.

5.5.3.1 Uniaxial Crystal

A wave travelling through a medium will travel at a fraction of the speed of light, c, dependent on the refractive index, n, of the material through which it is travelling, this relationship, $\nu_p = c/n$, defines the phase velocity of a wave (ν_p). In an anisotropic

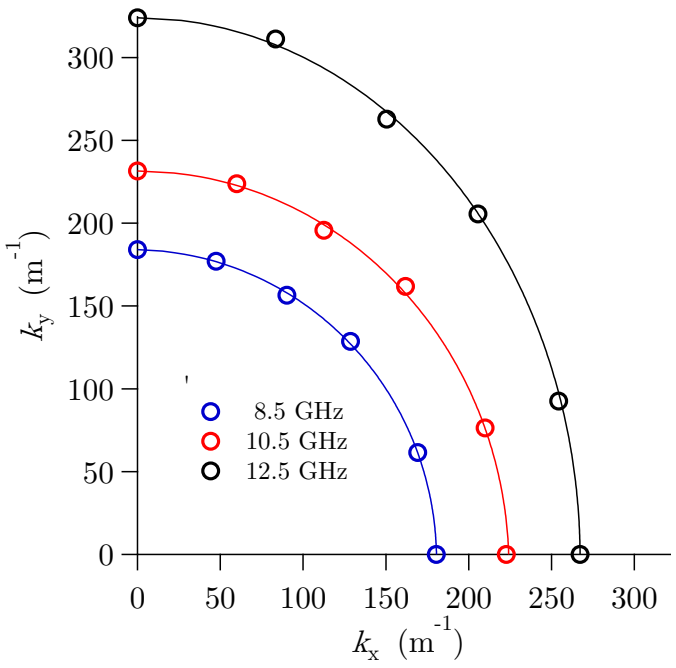

Figure 5.12: Equi-frequency contours which describe the azimuthal dependence of the dispersion of the fundamental surface. The experimental data for 8.5 GHz (blue circles), 10.5GHz (red circles) and 12.5GHz (black circles) and corresponding fits (lines) are shown.

medium, a wave will propagate at a different velocity dependent on the propagation direction i.e. the refractive index that it experiences. For a wave propagation in a given direction through a medium, an ellipsoidal surface called the indicatrix can be used to determine the allowed polarisation directions and corresponding refractive indicies [85]. This is a familiar concept in anisotropic optical media, which are generally crystalline, where the optical properties are closely related to the symmetry of the crystal. In this chapter this concept is extended such that it is possible to characterise the azimuthal dependence of the fundamental surface mode supported by the rectangular hole array, by generating equi-energy contours that describe the surface wave dispersion.

First consider the equation for a general index ellipsoid or indicatrix

$$\frac{x^2}{n_x^2} + \frac{y^2}{n_y^2} + \frac{z^2}{n_z^2} = 1, \tag{5.5.1}$$

where n_x, n_y and n_z are the principal refractive indicies of a crystal. At a given frequency, it is equivalent to, apart from a scale factor, the surface mapped out by the electric displacement vectors $\mathbf{D}$ corresponding to a constant energy density. If $n_x = n_y$, the indicatrix becomes an ellipsoid of revolution, representing a uniaxial crystal. The

equation of the uniaxial indicatrix is

$$\frac{x^2+y^2}{n_o^2}+\frac{z^2}{n_e^2}=1, \tag{5.5.2}$$

where n_o and n_e are the refractive indicies experienced by a wave polarised perpendicular and parallel to the optic axis respectively. The refractive index $n(\theta)$ of a wave propagating at an angle θ with respect to the axis can be calculated with reference to Figure 5.11. For a given wave, the value of $n(\theta)$ is given by the length $0X$. The co-ordinates of the point on the ellipse relative to the origin are

$$x=-n(\theta)\cos\theta \tag{5.5.3}$$

$$z=n(\theta)\sin\theta \tag{5.5.4}$$

$$z=0. \tag{5.5.5}$$

This point lies on indicatrix therefore

$$\frac{1}{n(\theta)}=\frac{\cos^2\theta}{n_o^2}+\frac{\sin^2\theta}{n_e^2}. \tag{5.5.6}$$

.

Using the following relationship for the phase velocity (ν_p) of a wave at a given frequency which relates in-plane momentum (k_x) to the index of fraction (n),

$$\nu_p=\frac{\omega}{k_x}=\frac{c}{n}, \tag{5.5.7}$$

the azimuthal dependent data can be manipulated to obtain the equi-energy contours, here n_o and n_e are the refractive indicies experienced by a wave propagating along the y- and $x-$ axes respectively and ϕ is the azimuthal angle measured with respect to the y- axis in the xy plane.

5.5.3.2 Ellipse of Limiting Frequencies

Each contour (Fig. 5.12) corresponds to a single frequency (horizontal dashed lines Fig. 5.10) where the circles represents the experimental data, and the elliptical line fits to the data. The spacing between these equi-energies contours is dictated by the dispersion of the mode; for instance, contours which are equally spaced are indicative of a mode which has a dispersion characterised by a constant gradient. This behaviour is observed at $k_y=0$, i.e. when the plane of incidence contains the long axis ($\phi=90°$), here the mode closely follows the light line, showing very little dispersion (Fig. 5.7 (a)). At $k_x=0$, which corresponds to when the plane of incidence contains the short pitch of

the structure ($\phi = 0°$), the spacing of the contours increase with frequency (as the mode approaches it limiting frequency at high k values) indicative of a highly dispersive mode (Fig. 5.5). Therefore Figure 5.12 clearly demonstrates the anisotropic response of the rectangular hole array, since at low frequencies (blue curve, 8.5 GHz), the response of the structure is almost isotropic (contour is approximately circular), whilst at higher frequencies (black curve, 12.5 GHz) the anisotropy of the structure becomes apparent, with the azimuthal dependence of the mode now described by an elliptical contour.

5.6 Conclusions

Using structure to control the limiting frequencies of bound surface waves allows one to create a tailored electromagnetic response with the desired surface symmetry. In this chapter, the strong anisotropy arising from a rectangular hole array structure, where the fundamental surface mode has two distinct limiting frequencies in orthogonal directions, has been characterised. Furthermore, because we are able to separate the onset of diffraction from the cutoff frequency of the hole (a consequence of the rectangular unit cell), it has been possible to study the dispersion of the higher order surface modes defined by the quantisation of the field along the length of the hole.

Chapter 6

Polarisation-Dependent Excitation of Surface Waves on a Zigzag Hole Array

6.1 Introduction

The 'enhanced transmission' recorded through the zigzag hole array, presented in this chapter, is attributed to the excitation of diffractively coupled surface waves. Due to the specific symmetry of the unit cell of the zigzag hole array, that is comprised of paired geometrically identical, alternately orientated, rhombic-shaped holes, it is shown this coupling condition can be achieved with both TM- and TE- polarised incident radiation. In Chapter 4 diffractive coupling to the surface modes supported by the structure under investigation was achieved via 'band-folding' effects, induced by the introduction of a second periodicity, in the form of a perturbation *perpendicular* to the plane of the sample, i.e. the 'coupling-in' grating. However, in this chapter it is shown that incident radiation can directly couple to the surface modes supported by the zigzag hole array, via scattering from its inherent *in-plane* periodicity, such that no additional coupling-in mechanism is required.

Of most interest in this chapter however, is the observed polarisation-selective excitation of individual surface wave modes. This behaviour is shown to be a direct consequence of the reduced symmetry of the system, with the orientation of the incident electric field with respect to the mirror plane key to determining the response of the structure. Also of note is the absence of the expected band gap at the first Brillouin zone boundary, attributable as well to the particular symmetry of this structure. Whilst the main focus of this chapter is the response of the zigzag hole array to radiation incident in the plane containing the long pitch of the structure, referred to as the 'zigzag pitch', a comparison is also presented of the response of the hole array to radiation incident in the

plane containing the orthogonal shorter pitch (i.e. the mirror plane). It is concluded that many of the symmetry arguments used to explain the response of the structure when the plane of incidence contains the zigzag pitch, are still valid. The experimental results in this chapter have been verified using numerical modelling technqiues, good agreement is demonstrated.

6.2 Background

The symmetry of a metamaterial or hole array may be reduced through the modification of the shape and/or arrangements of the constituent subwavelength elements, allowing access to modes and phenomena unavailable in structures with higher symmetry. The excitation of "trapped-modes" (i.e. electromagnetic modes that are weakly coupled to free space) on planar metamaterials based on asymmetric split rings resonators (ASRRs) for instance, has been reported at microwave [86–89], near- IR [90], THz [91] and optical [92] frequencies, with uncharacteristically strong and narrow (high- quality (Q) factor) resonances, being observed. In particular, when the incident electric field is perpendicular to the plane of mirror symmetry of an array of ASRRs [86], spectral selectivity, a special feature originating from asymmetrical structuring, has been reported. Further, the normal incidence reflection and transmission properties of circularly polarised radiation from and through chiral ASRRs [87] was shown to be highly dependent on the handedness and direction of incident radiation, attributable to the lack of mirror symmetry in this structure.

Another phenomenon arising from metamaterials with a high degree of asymmetry is metamaterial induced transparency, which has been observed using individual two-gap ASRRs [91]; here displacement of one gap from the central vertical axis reduces the symmetry, allowing for tuning of the amplitude and bandwidth of the transparency window. Further, negative refractive index resulting from symmetry-breaking of cut-wire pairs has been demonstrated at microwave frequencies [93] and polarization-independent resonant absorption, arising from crossed trapezoid array structures [94], at optical frequencies. Additionally, the studies of the propagation of surface waves on periodic structures with reduced symmetries formed from arrays of slits [22, 23] and holes [95] have shown that the reduced symmetry, which arises from the addition of a second periodicity or substructure within the unit cell, results in Fano-like phase resonances, not normally observed in their symmetric counterparts.

In this chapter, the microwave response of a reduced symmetry hole array, which is formed from an array of deep, geometrically identical, rhombic-shaped elements (holes), arranged in a zigzag pattern, is explored. Figure 6.1 shows a photograph of a section of the sample. In 1998 Ebbesen and his co-workers [96] observation of enhanced optical

transmission (E0T) confirmed that the transmission through an array of waveguide below cutoff could far exceed that predicted by Bethe [97] for an isolated hole. This transmission enhancement was later attributed to the excitation of diffractively coupled surfaces waves (SPPs at optical frequencies) [98]. Further theoretical [99, 100] and experimental studies [101] agreed with the SPP excitation theory. There are three possible mechanisms through which transmission can occur in this scenario; without the excitation of SPPs, the fields inside the metal film will exponentially decay with very little penetration into the metal, resulting in a very small probability of tunnelling occurring and transmission will be very low unless the film is very thin. However, if a SPP is excited on a single interface there will be an increased probability of tunnelling as the resonant fields at the surface will be enhanced over that of a non-resonant photon electron interaction. Further, if SPPs are excited on both interfaces they can couple together to give significant transmission enhancement if the system is symmetric.

At microwave frequencies although penetration of the electric field into the metal is assumed to be negligible, enhanced transmission phenomena through hole arrays can however still be observed, [84, 102–110]. At microwave frequencies the observed EOT through these structures is also a result of diffractively coupled surface waves. In this work presented in this chapter it is the surface waves that are supported on each interface of the zigzag hole array, which couple through the structure and re-radiate from the second surface giving the 'enhanced transmission recorded in the experiments, are limited in frequency by the localised resonances (waveguide modes) supported by the holes.

It is the unique symmetry of the zigzag hole array that is responsible for the unusual phenomena observed in its microwave transmission response. These include the polarisation-selective excitation of different surface wave bands and the absence of the expected band gap in the dispersion of the surface waves, which are discussed in detail later in this chapter. The unit cell (shaded green region Fig. 6.1) comprises paired rhombic-shaped holes that are the mirror image of each other and it is this paired arrangement that reduces the symmetry of the system, via the introduction of a second periodicity within the unit cell. When defining initially the plane of incidence to be the xz-plane ($\phi = 0°$), depicted by the dashed line Fig. 6.1, this zigzag geometry can be characterised by a surface modulation in the plane of the incident wavevector (xz-plane), with an orthogonal mirror plane (yz-plane) dotted line (Fig. 6.1).

The zigzag hole array, because of its particular symmetry, allows for direct coupling of both TM- and TE-polarised radiation to the surface modes supported by the structure, without the necessity to enhance the momentum of the incident wavevector by another means. This is in contrast to earlier microwave surface wave experiments, in particular the work of Hibbins *et al.* [2] who provided the first experimental verification of 'designer'

surface waves in the microwave regime, together with the work presented in Chapter 4. In these aforementioned studies, the required momentum enhancement was achieved by introducing a 'coupling-in grating into the system, which was placed on top of the hole array at a periodicity twice that of the hole array beneath. Originally non-radiative modes were then band-folded into the radiative region, via scattering from the periodicity associated with the grating. The grating however, creates a perturbation perpendicular to the plane of the hole array. Furthermore, as shown in Chapter 4, the size and shape of this 'coupling-in grating and its position relative to the hole array can greatly perturb the dispersion of the modes supported by the hole array. It is advantageous therefore, that scattering from the perurbation due to the 'zigzag' modulation *in* the plane of the sample, arising from the substructure in the unit cell, is the sole mechanism required to couple incident radiation to the supported surface modes.

It is worthy to note, that each element (hole) from which the zigzag hole array is formed, is geometrically identical. Consequentially each hole has identical eigenmodes i.e. support identical localised resonances (waveguide modes) and equivalent boundary conditions are maintained on every hole. The symmetry of the system is reduced by the particular orientation of neighbouring elements, i.e. their paired arrangement. Combined with their rhombic-shaped cross-section, this leads to a polarisation-dependent response. This is in contrast to the the work of Liu *et al.* [111] for instance, the unit cells in their study comprised either two different sized holes per unit cell or unequally spaced unit cells formed from multiple identical holes. However, in many ways the zigzag hole array is analogous to the slit array study by Rance *et al.* [23], in which each slit was geometrically identical, such that each cavity supported identical modes. It was the alternate arrangement of neighbouring slits that reduced the symmetry of the system, leading to the novel observed effects, not achievable in a similar system with a higher degree of symmetry.

6.3 Experimental Sample and Setup

The experimental sample was manufactured using 3D printing and metallisation techniques (see Section 3.3 for further details). Built from nine separate blocks of rhombic-shaped guides, due to the limitations on build size of the 3D printer, the sections were slotted together to form a structure approximately 360×360 mm in size. The assembled parts were then metallised, whereby each interface was coated with a thin, 15 μm layer of copper. The resulting sample can be approximated as a perfect electrical conductor (PEC) substrate perforated with an array of close-packed rhombic-shaped holes. Each hole (element) is geometrically identical with a uniform rhombic cross-section and of depth $h = 20$ mm.

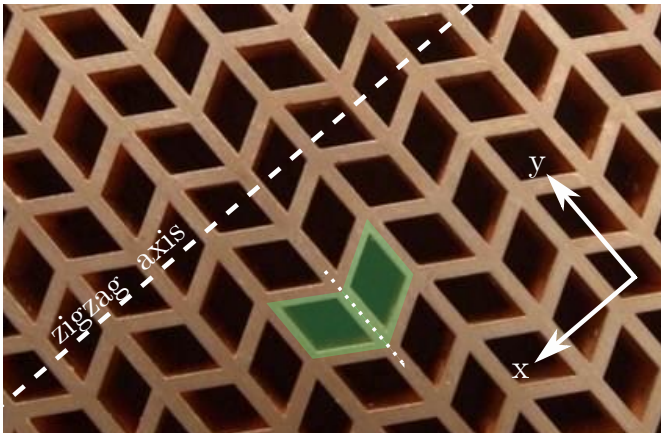

Figure 6.1: Photograph of experimental sample. Plane of incidence when $\phi = 0°$ (dashed line) and coordinate system is shown. The shaded green region highlights the unit cell and the dotted line represents a plane of mirror symmetry.

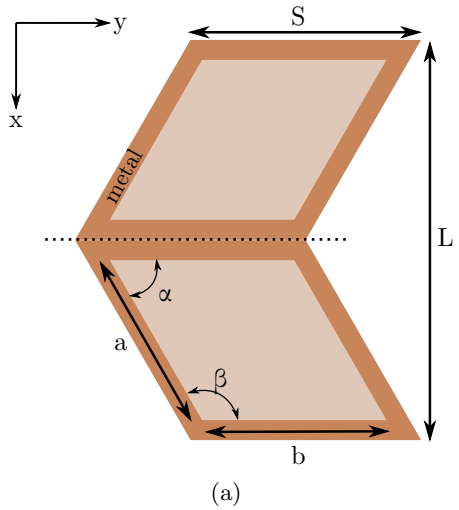

(a)

Figure 6.2: Schematic representation of the unit cell which is formed from paired rhombic-shaped holes of size, $a = b = 7.0$ mm, where $\alpha = 60°$. The long or zigzag pitch $L = 16.5$ mm and orthogonal pitch $S = 9.5$ mm are shown. The dotted line represents the plane of mirror symmetry.

The internal, a $(= b)$, and external, S, dimensions of each hole are 7.0 mm and 9.5 mm respectively, with $\alpha = 60°$ (and $\beta = 2\alpha = 120°$). The unit cell, Figure 6.2, contains two elements that are the mirror image of each other, the dotted line depicts the plane of mirror symmetry. The long or zigzag pitch, L, is of length 16.5 mm and the orthogonal shorter pitch, S, is of length 9.5 mm. At normal incidence ($\theta = 0°$), the onset of diffraction from the long (zigzag) pitch (L), occurs at 18.2 GHz, just below the cutoff frequency (f_1) of a single, isolated, rhombic-shaped waveguide of infinite length. Diffraction from the orthogonal pitch (S) occurs at 31.6 GHz for normally incident radiation, which, since it is above the frequency of the second supported waveguide

resonance, f_2, is beyond the region of interest of this study.

A collimated plane wave of microwave radiation ($8\,\text{GHz} \leq f \leq 40\,\text{GHz}$) is incident on the sample initially in the xz-plane, ($\phi = 0°$), i.e. the plane containing the 'zigzag axis', using a horn antenna placed at the focus of a 2 m focal length spherical mirror. The transmitted radiation is then collected by a similar spherical mirror and focused into a detector horn. A more detailed description of this experimental technique can be found in Section 3.2.1.2. The transmission spectra were recorded as a function of incident angle, θ, ($-65° \leq \theta \leq 65°$) in incremental steps of 0.2° and the resulting data discussed in the following sections of this chapter provides information on the dispersion of the modes supported by the zigzag hole array.

6.4 Localised Resonances of a Single Element

6.4.1 Rhombic-Shaped Cross-Section Waveguide

In order to understand the response of the hole array (the array of holes) it is first necessary to explore the modes supported by a single element, i.e. the localised resonances (waveguide modes) of the holes. As discussed previously, it is the frequency of these localised resonances which provide the asymptotic limits for the surface modes supported by the hole array (Chapter 2). The predicted field distributions in this section have been obtained using a waveport-type model [66]. The fundamental mode of a single, isolated, uniform rhombic-shaped waveguide, where each side is of length, $a = 7.0$ mm, with $\alpha = 60.0°$, formed from PEC, filled with vacuum and infinite in extent in the z-direction, is a transverse electric (TE) waveguide mode, supported at $f_1 = 18.33$ GHz, the predicted electric field profile of which is shown in Figure 6.3 (a). Here the colour map represents the time-averaged electric field with red and blue regions representing high and zero field enhancement respectively, and the arrows the instantaneous vector electric fields. Further higher order waveguide modes are supported, the electric field profiles of the next two are shown in Figure 6.3 (b) and (c). These two solutions are degenerate and are supported at $f_2 = 28.71$ GHz. However, to break the degeneracy and fully resolve these two modes, a rhombic cross-section with $\alpha = 60.001°$, has been modelled. At frequencies below f_1 and f_2, the evanescent fields within the hole create the necessary conditions for a bound mode to be supported on an array of such holes (as discussed in Chapter 2).

6.4.2 Triangular-Shaped Cross-Section Waveguide

It is possible to track the evolution of the waveguides modes of a rhombic-shaped guide from those supported by a guide with a square cross-section, by reducing the angle

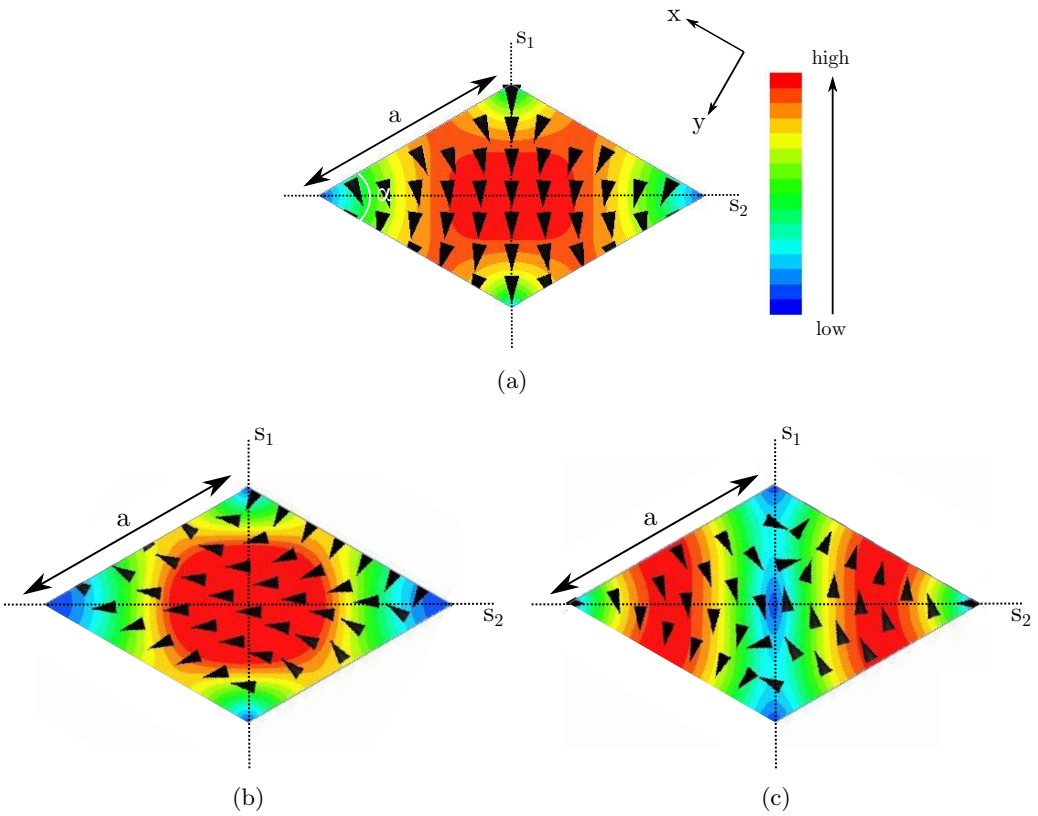

Figure 6.3: Predicted time-averaged (colour map) and instantaneous electric vector (arrows) field profiles of the three lowest order waveguide modes supported by a uniform rhombic-shaped waveguide, of side length $a = 7.0$ mm and infinite length, calculated over a surface parallel to the $xy-$plane of the waveguide at (a) $f_1 = 18.33$ GHz, and (b) and (c) at $f_2 = 28.71$ GHz. Red and blue regions corresponds to high and zero field enhancement respectively.

labelled α (Fig. 6.3 (a)), whilst maintaining each side of the guide to be of length a. However, it is helpful to refer to the work of Overfelt *et. al* [112] that in fact showed for a rhombic waveguide with a $60° - 120°$ cross-section, that mode (b) and (c) in Figure 6.3 can be found by applying the Riemann-Schwarz reflection principle [113] to the eigenfunctions of an equilateral triangle. It is not possible to determine the lowest-order mode using this technique however, and the dominant mode does not have an exact analytic solution. The field profiles of the dominant modes supported by a guide with an equilateral triangular cross-section of side length $a = 7.0$ mm and infinite in extent are shown in Fig. 6.4. It is clear that the time-averaged electric field profiles of mode (b) and (c) in Fig. 6.3 can be obtained by reflecting modes (a) and (b) in Fig. 6.4 about the axis labelled S_1. To fully resolve these modes and break the degeneracy, once again an angle $\alpha = 60.001°$ has been used. Further modelling (not shown) reveals that when the symmetry of the rhombic-shaped guide is reduced, i.e. is no longer formed from a pair of equilateral triangles ($\alpha \neq 60°$), the second order modes of the rhombic-shaped

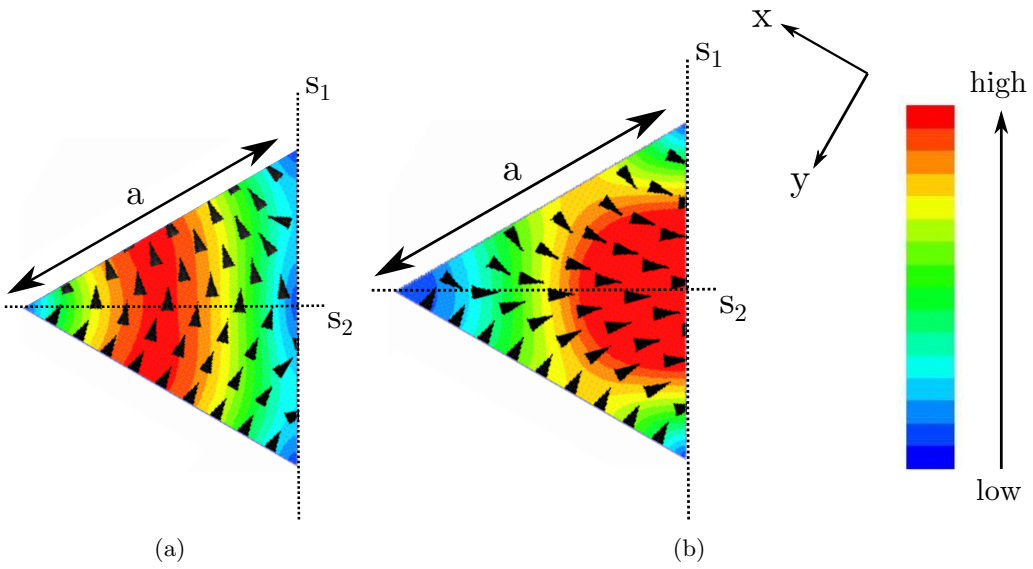

Figure 6.4: Predicted time-averaged (colour map) and instantaneous vector (arrows) electric field profiles of the two degenerate dominant modes supported by a waveguide with an equilateral triangle cross-section, of side length $a = 7.0$mm and infinite in length, calculated over a surface parallel to the $xy-$plane of the waveguide, at $f_2 = 28.71\,\text{GHz}$. Red regions corresponds to high field enhancement and blue corresponds to a field magnitude of zero.

guide are no longer degenerate.

6.5 Experimental Results, $\phi = 0°$

The experimental transmission spectra (grey scale) when TE- and TM-polarised radiation is incident in the xz-plane, i.e. plane of incidence contains the zigzag pitch ($\phi = 0°$) on the zigzag hole array is illustrated in Figure 6.5 (a) and (b) respectively, note the logarithmic scale. For reference, this data plotted on a linear scale, is shown in Figure 6.6 (a) and (b). The frequencies of the localised resonances ($f_1 = 18.33\,\text{GHz}$ and $f_2 = 28.71\,\text{GHz}$) supported by each hole (described in Section 6.4.1) are represented by the horizontal dashed lines. It is important to note these simply provide a guide for the frequencies to which the surface modes are limited by. The finite height and effect of the neighboring elements, i.e. the array, are not included in the calculation of these frequencies. These localised resonances hybridise with grazing diffracted orders and the resulting surface modes are highly dispersive, closely following the in-plane first and second order diffracted light lines (diagonal red and blue lines respectively), asymptotically approaching limiting frequencies dictated by f_1 and f_2, when they become strongly localised to the surface.

The key result however, is the striking polarisation-dependent response of the struc-

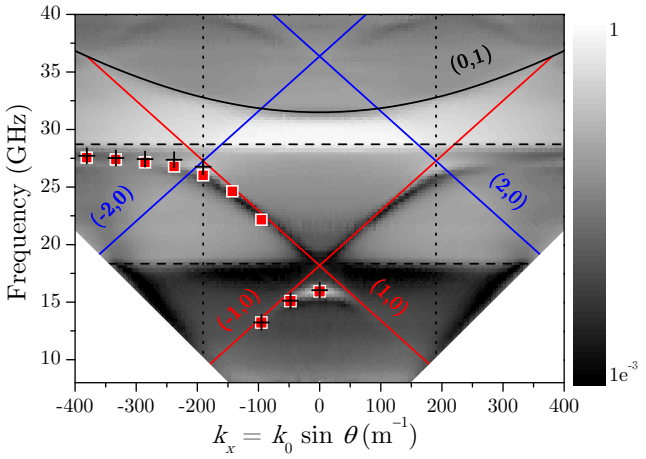

(a)

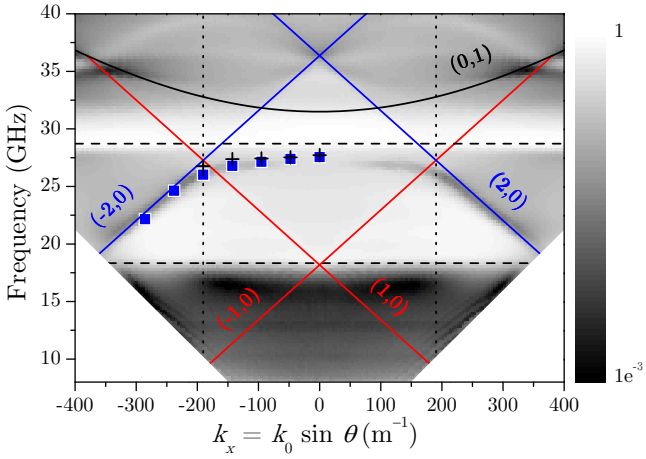

(b)

Figure 6.5: Experimental transmission data (grey scale) plotted on a log scale for (a) TE- and (b) TM-polarised radiation incident on the zigzag hole array in the xz-plane. Light and dark regions correspond to high and low transmissivity respectively. The horizontal dashed lines represent the frequencies of the first f_1 and second f_2 order localised resonances for an infinite length guide. The red and blue diagonal lines represent the first and second order in-plane diffracted light lines respectively, and the solid black line the first order parabolic out-of-plane diffracted light line. The vertical dotted lines define the first Brillouin zone. The squares and crosses correspond to the eigenmodes of the symmetric and anti-symmetric fields solutions of the supported surface modes, respectively.

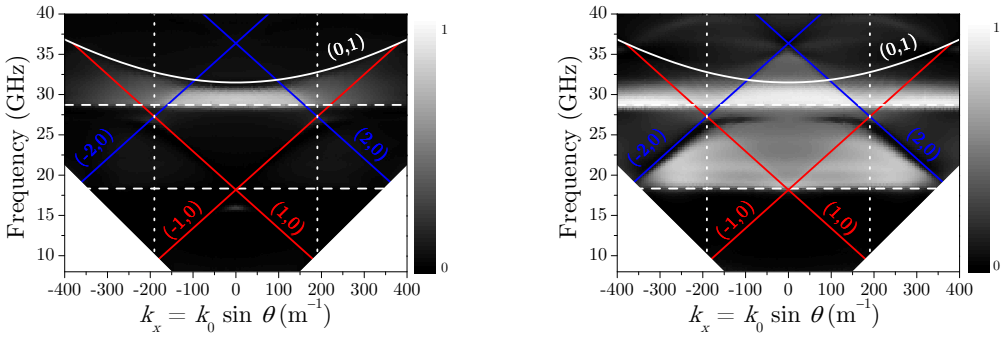

Figure 6.6: Experimental transmission data (grey scale) plotted on a linear scale for (a) TE- and (b) TM-polarised incident radiation in a xz-plane. Light and dark regions correspond to high and low transmissivity respectively. The horizontal dashed lines represent the frequencies of the first f_1 and second f_2 order localised resonances for an infinite length guide. The red and blue diagonal lines represent the first and second order in-plane diffracted light lines respectively, and the white solid line the first order parabolic out-of-plane diffracted light line. The vertical dotted lines define the first Brillouin zone.

ture. When TE-polarised radiation is incident on the sample (Fig. 6.5 (a)), a surface mode is observed, following the first order in-plane diffracted light lines, which is limited in frequency by the first-order localised resonance, before continuing to follow the same set of diffracted light lines, before being limited in frequency by the second order localised waveguide resonance. However, there is an obvious lack of coupling to this mode when TM-polarised radiation is incident on the sample, rather a mode is observed following the second order in-plane diffracted light lines in the TM response (Fig. 6.5 (b). (Note the absence of coupling to this mode in the TE-polarised response.) This intriguing polarisation-selective behaviour of coupling to different order surface wave bands will be discussed in detail in Section 6.5.3.

6.5.1 Variation in Hole Depth (h)

The observed 'enhanced transmission' in this study can be attributed to the excitation of diffractively coupled surface waves, as discussed in Section 6.2. The zigzag hole array can be considered analogous to a thin metal film (i.e. one that is thinner than a few skin depths) which is symmetrically surrounded by dielectric [114], or a thin metal film corrugated on both sides [115]. Both systems have multiple interfaces, and can support a surface mode at each interface. These modes are degenerate and couple together forming two resonances with different field profiles and energies and are often referred to as the symmetric and anti-symmetric modes, depending on their field and charge distribution.

For the zigzag hole array, coupling incident radiation to these modes strongly enhances the electric fields at the front interface, which exponentially decay along the length of the hole before strengthening again close to the bottom interface of the structure, leading to the 'enhanced transmission' observed in this study.

Modelling of the eigenmodes of the system reveals that close to the predicted limiting frequencies f_1 and f_2, the surface mode splits into a symmetric and anti-symmetric field solution, which approach two different limiting frequencies [59]. The predicted dispersions of which are represented by the squares and crosses respectively, in Figure 6.5 (a) and (b). The predicted instantaneous electric field distribution (arrows) of the coupled surface wave pair, supported below f_1 at $k_x = 0$ in the TE-polarised response, plotted in the xz-plane, are shown in Figure 6.7. The fundamental mode (N = 0), the dispersion of which is represented by the red squares (at frequencies lower than f_1) in Fig. 6.5 (a), has a symmetric field solution. That is, as can be seen in Fig. 6.7 (a), the electric field does not switch direction along the length of the hole. For a guide of infinite length this mode would be asymptotic to the effective surface plasma frequency at higher values of k_x, defined by the cut-off of the hole. For a system with finite length holes, this lowest order resonance is modified upwards in frequency due to the additional momentum contribution from the longitudinally quantised field along the length of the guide. As can be seen in Figure 6.7 (b), the higher order anti-symmetric mode (N= 1), the dispersion of which is represented by the crosses (at frequencies lower than f_1) in Figure 6.5 (a), has longitudinally quantised electric fields, the E-field does switch direction along the length of the hole. Note, that a similar coupled surface wave pair are also predicted at frequencies below f_2 (Fig. 6.5 (a)) with the squares and crosses once again depicting the predicted eigenmodes associated with the symmetric and anti-symmetric field solutions, respectively.

However, whilst two eigenmodes are predicted (which are very close in frequency), the coupled surface wave pair are not experimentally resolved in the transmission spectra. The length of the holes were selected such that only a single transmission peak is observed (which is in good agreement with numerical predictions), that is, the two solutions, i.e. the limiting frequencies of the coupled surface wave pair, converge on a single frequency. (Note this frequency is below the cutoff frequency (f_1) of an infinitely length hole due to band gaps in the modes dispersion). Plotting the instantaneous vector electric field at different values of phase, at the predicted transmission peak (not shown), reveals that the supported mode has a mixed character of both the symmetric and anti-symmetric field solutions. Further modelling of the transmissivity response shows that, as to be expected, the separation in frequency of these two solutions is highly dependent on the hole depth. Figure 6.8 shows the frequency of the predicted transmission peaks associated with the symmetric (crosses) and anti-symmetric (squares) solutions of the

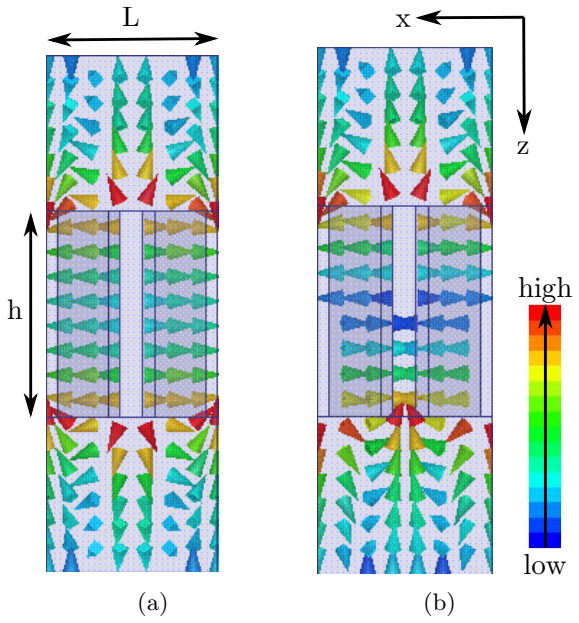

Figure 6.7: Predicted instantaneous vector electric field profiles plotted in the xz-plane associated with the (a) symmetric and (b) anti-symmetric field solution of the surface mode supported at $k_x = 0$, below f_1, in the TE-polarised response. Red regions and blue arrows correspond to a high field enhancement to a field magnitude of zero respectively.

fundamental surface mode supported below f_1, for different hole depths, h, when TE-polarised radiation is normally incident ($\theta = 0°$) on the sample in the plane containing the zigzag axis. It can be seen that as discussed previously, for a hole of depth $h = 20$ mm, a single transmission peak is predicted (as the two solutions overlie), but when the depth of the hole is reduced, the anti-symmetric (squares) and symmetric (crosses) field solution are resolved.

In addition to the coupled surface wave pair, a family of higher order modes associated with higher order quantisations of the field along the length of the holes, similar to those in Chapter 5, are also observed. These are evident in the TM-polarised response of the structure, particularly when the data is plotted on a linear scale (Fig. 6.6) where a band of high transmission is clear (white regions) in between f_1 and f_2. Interestingly this behaviour is not observed in the TE-polarised response (Fig. 6.6 (a)), extremely low transmission is observed at all frequencies below f_2. Further discussion and an explanation for this will be provided in Section 6.6.

6.5.2 Band Structure

In Section 6.5.3, the origin of the polarisation-selective excitation of different surface wave bands is presented. First in this section, a simplistic approach is adopted to explain the polarisation-independent band structure of the zigzag hole array, the analysis

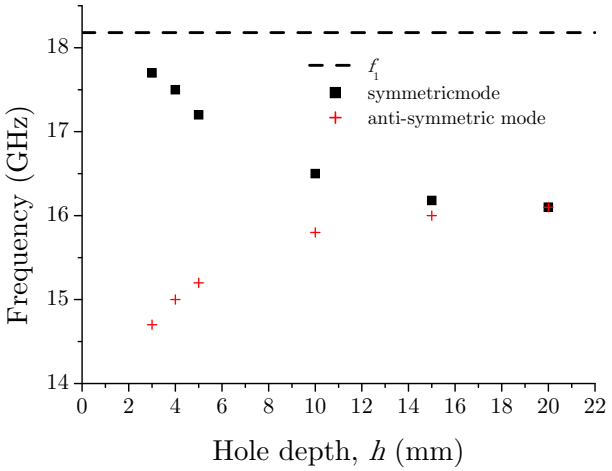

Figure 6.8: Predicted transmission peaks associated with the symmetric (crosses) and anti-symmetric (squares) solutions of the fundamental surface mode supported below f_1 (dashed line) for different hole depths, h when TE-polarised radiation is normally incident on the sample.

of which, can be effectively reduced to just two components of the profile of the hole array; a very large amplitude short pitch component of period $L/2$, i.e. the closely spaced array of deep holes, convolved with a much weaker, longer pitch component of period L, associated with the different orientation of neighbouring holes. It is the substructure of the array of holes (pitch $L/2$) which creates the necessary boundary conditions at the metal surface for bound surface waves to be supported and provides the biggest perturbation to the band structure. It is then the modulation in the plane of the incident wavevector, arising from the paired arrangement of the rhombic-shaped holes, associated with the zigzag geometry (pitch L), which provides a mechanism for the incident radiation to diffractively couple to the surface modes supported by the hole array.

A similar discussion of the band structure of systems with a dual periodicity can be found in Refs. [21–23]. In the work in this chapter, the ratio of the long to short pitch component is 2:1, correspondingly the wavevector associated with the long pitch component of the zigzag hole array, k_g, is half that associated with the short pitch component, $2k_g$, where $k_g = (2\pi/L)$. This is not a requirement of this analysis, examples of systems where the ratio of the two periodicities are 3:1 for instance, can be found in Refs[21, 22]. It is important to note though that this analysis does not provide information about the polarisation of the incident field required to couple radiation to the supported surface modes. Further, only the dispersion of the lower band-edge of the fundamental surface mode in the limit of weak coupling is considered in this analysis

and the presence of any structure-induced band gaps that may occur is ignored.

A schematic representation of the resulting band structure for a dual-pitch system, such as the zigzag hole array, can be seen in Figure 6.9 (a). The long pitch component of the profile of the hole array is too weak to cause any significant perturbation of the surface wave bands, it will however, as can be seen in Fig. 6.9 (a), introduce important band folding effects. That is, the originally non-radiative modes associated with the short pitch component ($L/2$), which have been scattered from $\pm 2k_{\mathrm{g}}$ (curved solid black lines Fig. 6.9 (a)) have now become radiative by diffraction associated with the long pitch component L, i.e. scattering by integer multiples of $\pm k_{\mathrm{g}}$. As can be seen in Figure 6.9 (a), this mode, the dispersion of which is represented by the dashed line, now lies within the radiative region (white regions).

It is only the modes which lie within the radiative region which can be directly coupled to by incident radiation and are observed in the transmissivity response of the zigzag hole array. Extending the aforementioned analysis to include higher order localised resonances (waveguide modes), the resulting band structure for the zigzag hole array can be obtained (Fig. 6.9 (b)). Note for clarity, only the dispersion of the lower band edge of the surface mode has been shown. In Figure 6.9 (b) each square corresponds to an eigenmode of the zigzag hole array, associated with the symmetric solution of the surface mode which is limited in frequency by the localised resonances f_1 and f_2 (horizontal dashed lines). The red and blue solid lines correspond to the first and second order in-plane diffracted light lines respectively, and the solid black lines the light lines which bound the radiative region (white region). The vertical dashed lines define the first Brillouin zone. Note that here, the different colours of the squares are not significant, only once the polarisation of the incidence field is considered, as in the following section, is it possible to distinguish between these modes.

6.5.3 Allowed Charge Distribution

The orientation of the incident electric vector, with respect to the mirror plane is key to understanding the polarisation-dependent response of the zigzag hole array. First consider when the electric vector lies perpendicular to the plane containing the incident wavevector (TE-polarised radiation) i.e. the electric field of the incident radiation lies in the plane of mirror symmetry. The schematic representation of the instantaneous electric field (solid arrows), in the low frequency limit is shown in Figure 6.10 (a). Note the local component of the electric vector contained *in the plane of incidence* (open arrows) switches direction at each mirror plane, a consequence of the alternate orientation of each hole. At low frequencies, the periodicity of the in-plane E-field component corresponds to a surface mode of wavelength λ_1, mode (1), which is equal to the pitch of the structure, L. This surface wave therefore originates from in-plane scattering via $k_{\mathrm{x}} = \pm k_{\mathrm{g}}$. Its inherent

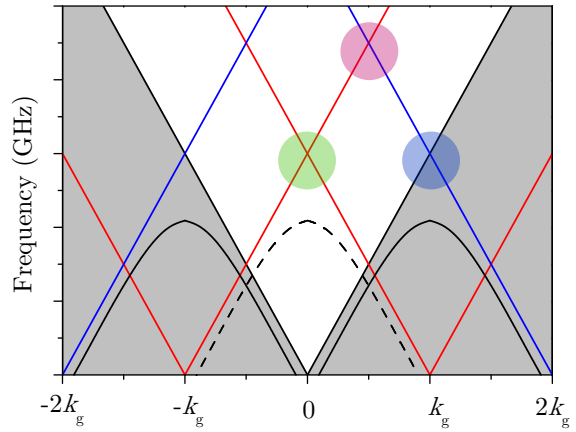

(a)

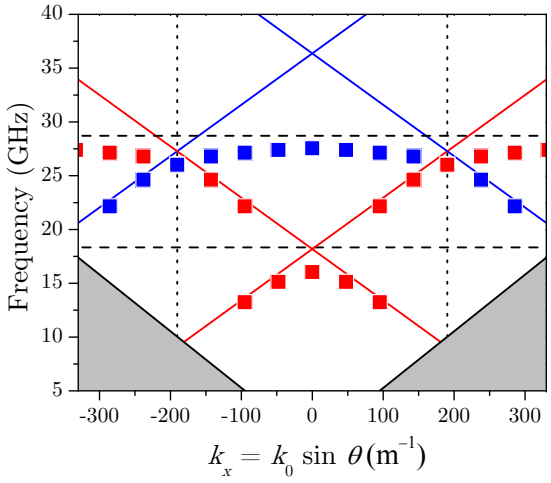

(b)

Figure 6.9: (a) Schematic representation of the band structure associated with a dual-pitch system. The curved solid and dashed black lines represent the modes diffracted from the short and long pitch respectively. The red and blue lines represent the first and second order in-plane diffracted light lines respectively. The solid black lines bound the radiative region (white region). (b) Predicted band structure for the zigzag hole array. Each square represents an eigenmode associated with the lowest band edge of the symmetric solution of surface modes limited in frequency by f_1 and f_2 (horizontal dashed lines). The red and blue lines represent the first and second order in-plane diffracted light lines. The vertical dotted lines define the first Brillouin zone.

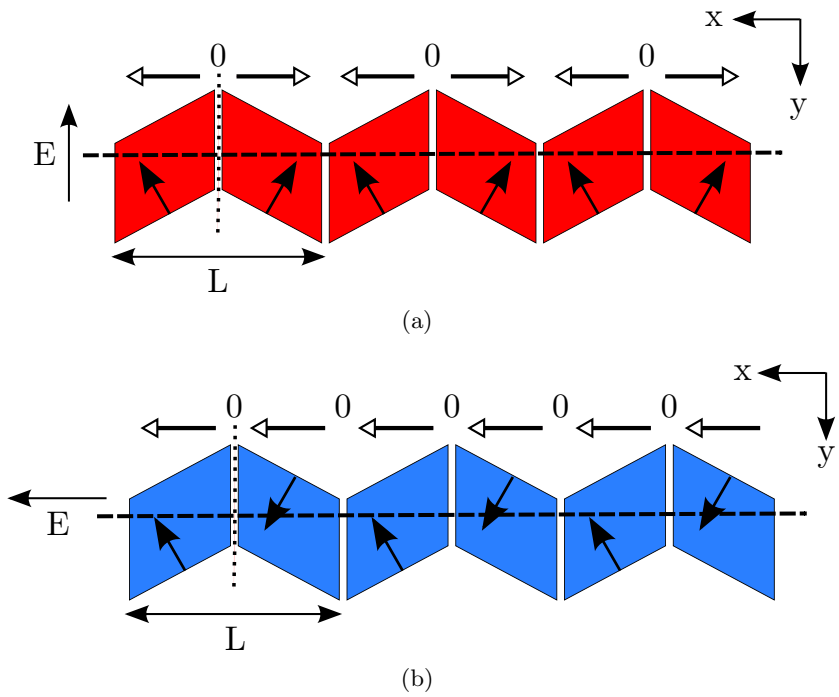

Figure 6.10: Schematic representation of the instantaneous electric field (solid arrows) for the surface mode supported at low frequencies for (a) TE- and (b) TM- polarised radiation incident in a plane containing the zigzag axis. Plane of incidence (dashed line) and mirror plane (dotted line) is shown. Open arrows represent the local component of the electric vector contained in the plane of incidence.

periodicity associated with L dictates it cannot be excited via scattering from $k_x = 0$. Therefore mode (1) is seen to follow the $\pm(1,0)$ in-plane diffracted light lines (Figure 6.5 (a)), is limited in frequency by the first supported waveguide mode (localised resonance) f_1, then continues to follow the same set of diffracted light lines before asymptotically approaching the frequency of the second localised resonance f_2.

However, when the electric field of the incident radiation is contained in the plane of incidence (TM-polarised radiation) i.e. the E-field of the incident radiation lies perpendicular to the plane of mirror symmetry, the orientation of the E-field with respect to the mirror plane, forbids the excitation of mode (1), this is evident from the lack of TM-polarised excitation of a mode associated with $\pm k_g$ scattering in Figure 6.5 (b). However, a surface wave, scattered from $k_x = \pm 2k_g$ is observed. The schematic representation of the instantaneous electric field (solid arrows) associated with this mode, in the low frequency limit is shown in Figure 6.10 (b). Again consider the component of the electric vector contained in the plane of incidence (open arrows). For an excitation field with this polarisation, at low frequencies, the in-plane E-field component cannot switch direction in alternate holes. There still is a structure induced periodicity though in the local component of the electric vector contained in the plane of incidence (open

arrows), with a periodicity *half* that of the long pitch L. Hence we observe a mode originating from in-plane scattering via $k_x = 2k_{\mathrm{g}}$ in the TM-polarised response (Fig. 6.5 (b)).

Due to the mirror symmetry of the structure, no polarisation conversion may occur for radiation incident in the plane containing the zigzag grating vector ($xz-$plane), hence the modes remain excited either via only TM- or TE-polarised radiation for all angles of illumination. Further, when considering the eigenmodes of the system (the polarisation-independent response) strictly the first Brillouin zone must be bounded by $k_x = \pm k_{\mathrm{g}}/2$. However, when the polarisation of the field required to excite the surface modes associated with the different diffracted orders is considered, the system is behaving as though the first Brillouin zone is effectively bounded by $k_x = \pm k_{\mathrm{g}}$, i.e. is twice that associated with the pitch of the structure L. It is therefore possible to make the general statement that TE-polarised radiation may only couple to surface modes scattered from in-plane *odd* diffracted orders, whilst TM-polarised radiation may only couple to surface modes scattered from in-plane *even* diffracted orders.

6.5.4 Band Gaps

As discussed in Section 2.2.3.1, at a Brillouin zone boundary, it is possible for a band gap to open up in the propagation of surface waves on corrugated surfaces, depending on the symmetry of the grating and the components present in grating profile [24, 25, 115]. Thus far in this chapter, the existence of structure-included band-splitting i.e. band gaps in the propagation of the surface waves supported by the zigzag hole arrray, has not been discussed. This issue is addressed by examining the dispersion curve in the region of the two lowest energy crossing points, firstly at normal incidence ($k_{\mathrm{x}} = 0$) and secondly at the first Brillouin zone boundary ($k_{\mathrm{x}} = \pm 1/2\, k_{\mathrm{g}}$). For reference, these two crossing points are highlighted by the green and pink shaded circles respectively, in Figure 6.9 (a).

First consider, the lowest energy crossing point within the radiative region (green circle Fig. 6.9 (a)), where a surface mode scattered from $-k_{\mathrm{g}}$ and $+k_{\mathrm{g}}$ meet at $k_{\mathrm{x}} = 0$. (Note this crossing point is equivalent to the crossing point highlighted by the blue circle Fig. 6.9 (a)). The wavelength of the surface mode at a crossing point, is equal to half that corresponding to the total wavevector associated with the scattering process. Therefore, the wavelength of the surface mode at $k_{\mathrm{x}} = 0$, is equal to the pitch of the hole array L, as it has arisen from a $2k_{\mathrm{g}}$ scattering process. Since there are two different energy standing wave solutions with a wavelength equal to the pitch of the hole array L, a band gap is opened up. The predicted dispersion of the two different energy bands associated with the two different standing wave solutions is shown in Figure 6.11 (a), (a section of the TE-polarised experimental transmissivity response of the sample (grey

scale) i.e. the data shown in Fig. 6.5 (a), is shown for reference.) Note that the different energy solutions are a result of a corrugation in the plane of the hole array, hence the time-averaged electric fields ((colour map) Fig. 6.11 (b)) associated with these modes have been examined in the plane of the top interface of the structure; the low energy band, the symmetric and anti-symmetric solutions of which are represented by the squares and black crosses respectively (Fig. 6.11 (a)), have high electric fields (red regions) centred on the metal regions in between the holes (top Fig. 6.11 (b)), whilst the high energy band (the symmetric and anti-symmetric solutions of which are represented by the triangles and white crosses respectively (Fig. 6.11 (a)) can be found by displacing the nodes of the aforementioned solution by a quarter of the pitch, such that regions of high electric field are centred over the holes (bottom Fig 6.11 (b)).

Now consider the next highest energy crossing point within the radiative region. This occurs at $k_x = 1/2\ k_g$ (pink circle Fig. 6.9), where the $2k_g$ and $-k_g$ diffracted light lines cross. As it turns out, due to the symmetry of the zigzag hole array, modes following the $2k_g$ and $-k_g$ diffracted light lines cannot be simultaneously excited by a field with the same polarisation, therefore two modes never meet at this crossing point. Furthermore, a band gap is forbidden here from symmetry arguments. The standing wave resulting from the coupling of two surface mode bands via scattering from -k_g and $2k_g$, has a wavelength equal to $2/3L$. Owing to the symmetry of the zigzag geometry, the two possible standing wave solutions in the plane of the surface with this periodicity have the same energies. The two field solutions are therefore degenerate, and no band gap is observed.

6.6 Experimental Results II, $\phi = 90^\circ$

So far in this chapter, the main focus has been on discussing the response of the zigzag hole array to radiation incident on the sample in the plane containing the zigzag axis (long pitch). It has been shown that the orientation of the incident E-field with respect to the mirror plane is the key to understanding the observed polarisation-selective excitation of different surface wave bands. In this section, the response of the zigzag hole array to radiation incident on the sample in the plane containing the shorter orthogonal pitch (yz-plane, dashed line Fig. 6.12) is explored and a comparison with the results discussed in Section 6.5 presented. In this new orientation, defined as $\phi = 90^\circ$, the plane of incidence and mirror plane are now collinear. Due to the particular symmetry of the zigzag structure, many of the symmetry arguments used to explain its response when the plane of incidence contains the zigzag axis are still in fact valid when the plane of incidence has undergone an azimuthal (ϕ) rotation of 90°.

The experimental transmission spectra (grey scale) for when TM- and TE-polarised

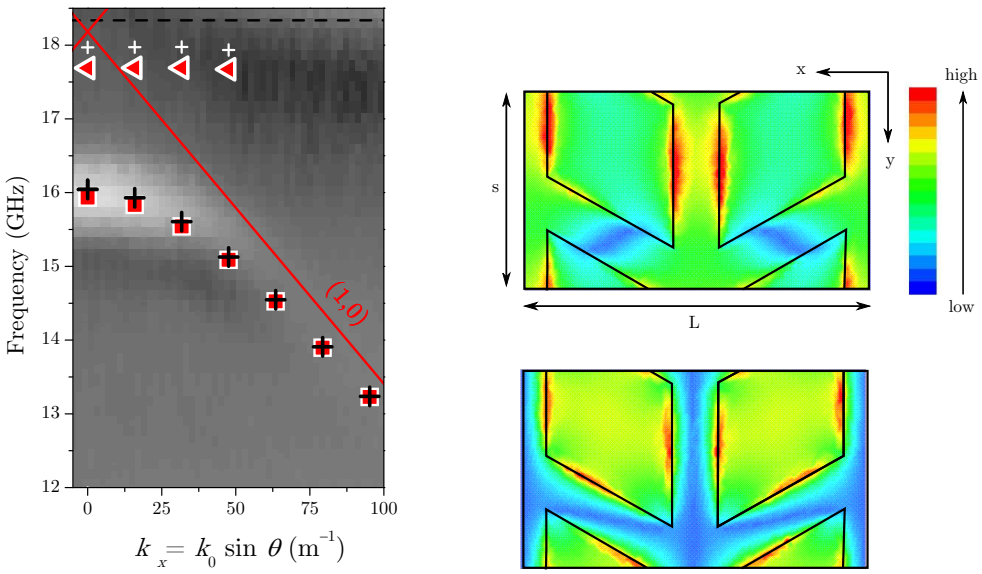

(a) (b)

Figure 6.11: (a) Predicted eigenmodes associated with the band gap centred around $k_x = 0$, below the first order localised resonance, f_1 (horizontal dashed line). The red squares and black crosses represent the predicted dispersion of the symmetric and anti-symmetric field solutions respectively of the mode associated with the lower band edge. The triangles and white crosses represent the dispersion of the symmetric and anti-symmetric solutions of the mode associated with the upper band edge. For reference the TE-polarised experimental transmission response (grey scale) when $\phi = 0°$ is shown. (b) Time-averaged (colour map) electric-field distribution of the symmetric solution associated with (top) lower band edge (bottom) upper band edge of the band gap at $k_x = 0$, plotted in the xy-plane on the top surface of the structure. Red and blue regions correspond to a high field enhancement and field magnitude of zero respectively.

radiation is incident on the sample in the yz-plane is illustrated in Figure 6.13 (a) and (b) respectively, note the logarithmic scale. For reference, the equivalent dispersion diagrams plotted on a linear scale are shown in Figure 6.14 (a) and (b). Light and dark regions correspond to high and low transmission respectively. The data was collected as described in Section 3.2.1.2. Note first, the first order parabolic *out-of-plane* diffracted light line, labelled (1,0) (solid white line) at small values of k_y, occurs at approximately the same frequency as the lowest order localised resonance f_1 (lowest frequency horizontal dashed line); recall when $\phi = 0°$, it lay *above* f_2. As evidenced by the bright band following the (1,0) diffracted light line in the TM-polarised response (Fig. 6.13 (a) and Fig. 6.14 (a)), it is clear that scattering from the the zigzag (long) pitch, still strongly influences the band structure of the zizag hole array. A more detailed discus-

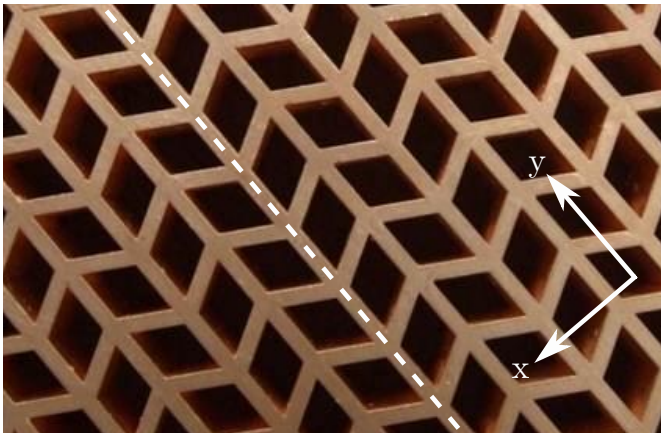

Figure 6.12: Photograph of experimental sample, plane of incidence when $\phi = 90°$ (dashed line) and co-ordinate system is shown.

sion of the nature of this aforementioned mode is provided later. Also of note is the absence of a similar band in the TE-polarised transmission response (Fig. 6.13 (b) and Fig. 6.14 (b)), thus indicating once again the zigzag hole array is displaying a strong polarisation-selective response.

From symmetry arguments, a mode excited at normal incidence ($\theta = 0°$) by a linearly polarised field, will be excited by a field with the opposite polarisation, when the plane of incidence undergoes an azimuthal (ϕ) rotation of 90°, with respect to the plane of the structure upon which the mode is supported. The red circles and black triangles in Figure 6.14 (c) show the TM- and TE-polarised response of the structure to normally incident radiation ($\theta = 0°$) in the plane containing the short ($\phi = 90°$) and long ($\phi = 0°$) axis respectively. As expected, they show good agreement. The solid black line represents the predicted transmission response when TE-polarised radiation is normally incident on the structure in the plane containing the long pitch, good agreement is shown with the experimental data. A peak in transmission is observed centred around approximately 16 GHz (and a second at approximately 29.5 GHz, above f_2). On examining the dispersion of the mode associated with the lowest frequency aforementioned peak, in the TM-polarised response (Fig. 6.13 (a) and Fig. 6.14 (a)), it can be seen that with increasing wavevector (k_y) this mode (bright band) follows the parabolic out-of-plane diffracted light line, and is limited in frequency by the first localised resonance supported by the holes f_1 (lowest frequency horizontal dashed line) at approximately 18 GHz. Two eigenmodes are predicted associated with this mode, corresponding to the symmetric and anti-symmetric field solution of the coupled surface wave pair, diffractively coupled by the out-of-plane pitch (i.e zigzag pitch), the dispersions of which are represented by the squares and crosses respectively in Figure 6.13 (a).

The periodicity of the mode associated with this coupled surface wave pair, on the

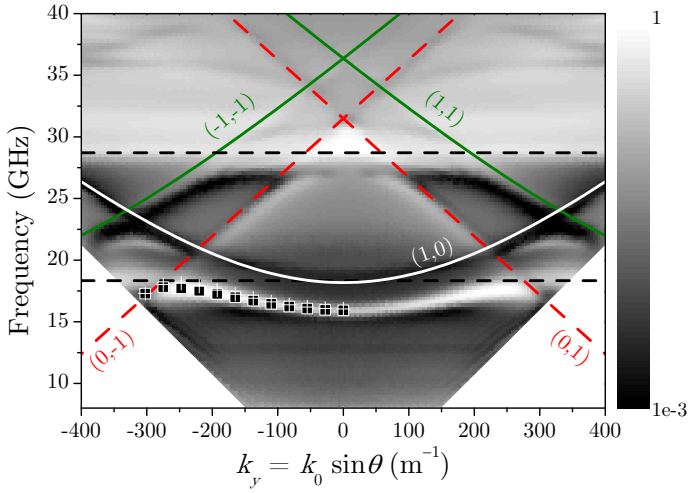

(a)

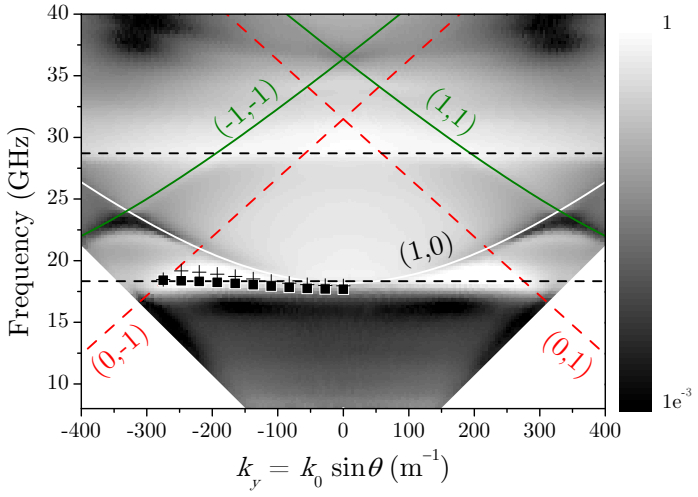

(b)

Figure 6.13: Experimental transmission data (grey scale) plotted on a log scale for (a) TM- and (b) TE-polarised radiation incident in the yz-plane. Light and dark regions correspond to high and low transmissivity respectively. The horizontal dashed lines represent the frequencies of the first (f_1) and second (f_2) order localised resonances of the rhombic shaped holes. The white and red lines represent the first order out-of-plane and in-plane diffracted light lines respectively and the green lines the $(\pm 1, \pm 1)$ diffracted light lines.

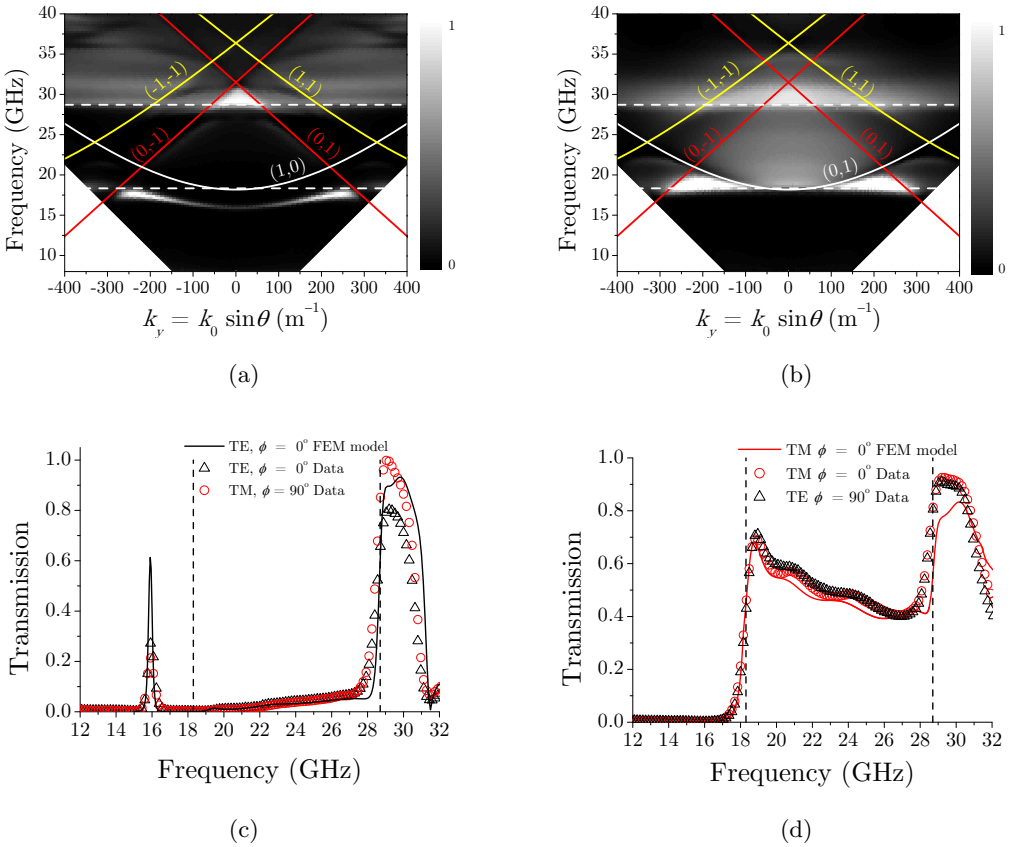

Figure 6.14: Experimental transmission data (grey scale) plotted on a linear scale for (a) TM- and (b) TE-polarised radiation incident on the sample in the yz-plane. Light and dark regions correspond to high and low transmissivity respectively. The horizontal dashed lines represent the frequencies of the first (f_1) and second (f_2) order localised resonances supported by the holes. The white and red lines represent the first order out-of-plane and in-plane diffracted light lines respectively and the yellow lines the $(\pm 1, \pm 1)$ diffracted light lines. (c) Experimental transmissivity response at $\theta = 0°$ when TM-(red circles) and TE-(black triangles) polarised radiation is incident on the sample at $\phi = 90°$ and $\phi = 0°$, respectively. Solid black line represents the predicted TE-polarised response at $\theta = 0°$ and $\phi = 0°$. (d) Experimental transmissivity response at $\theta = 0°$ when TM-(red circles) and TE-(black triangles) polarised radiation is incident on the sample at $\phi = 0°$ and $\phi = 90°$, respectively. Solid red line represents the predicted TM-polarised response at $\theta = 0°$ and $\phi = 0°$.

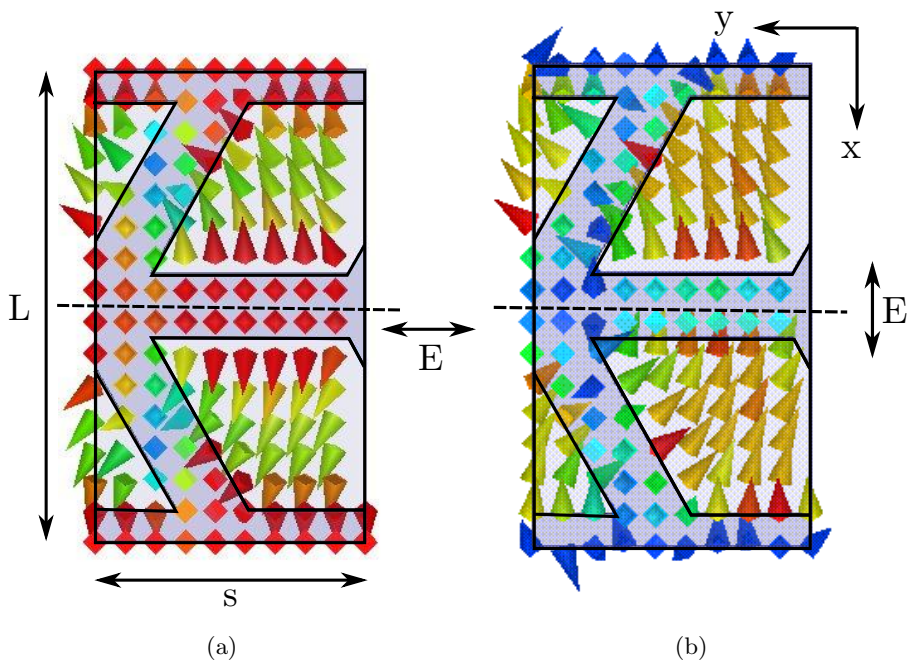

Figure 6.15: Instantaneous vector electric field profiles (arrows) plotted in the $xy-$ plane on the top interface of the structure, associated with the (a) TM- and (b) TE- excited mode supported at normal incidence, when the plane of incidence (dashed line) contains the short pitch. Red and blue arrows correspond to a high field enhancement and field magnitude of zero respectively.

surface of the structure is equal to the zigzag pitch; the resonant fields, illustrated by the vector electric fields (arrows), plotted at a phase corresponding to maximum field enhancement, in the xy-plane on the top interface of the structure, are shown in Figure 6.15 (a). Here the dashed lines represents the plane of incidence (as well as the plane of mirror symmetry) and the orientation of the incident electric (E)-field is shown. It is clear that in order to couple incident light to this mode, the electric field of the incident radiation is required to be contained in the plane of mirror symmetry. Hence, this mode can only be excited with TM-polarised radiation when the plane of incidence contains the short pitch ($\phi = 90°$) and with TE-polarised radiation when the plane of incidence contains the long pitch ($\phi = 0°$). Therefore, it is possible to conclude that this coupled surface wave pair are equivalent at normal incidence, to the coupled surface wave pair observed in the TE-polarised response below f_1 (squares and crosses Fig. 6.5 (a)), when the plane of incidence contains the long axis ($\phi = 0°$). Indeed, the resonant fields shown in Fig. 6.15 (a) are, as expected, the same as those in the top figure of Fig. 6.11 (b), which show the resonant field associated with the TE-excited lower band edge of the surface mode supported at normal incidence. In each case high fields (red regions) are centred over the metal regions of the structure.

Now, consider the transmissivity response of the zigzag hole array when it is illumi-

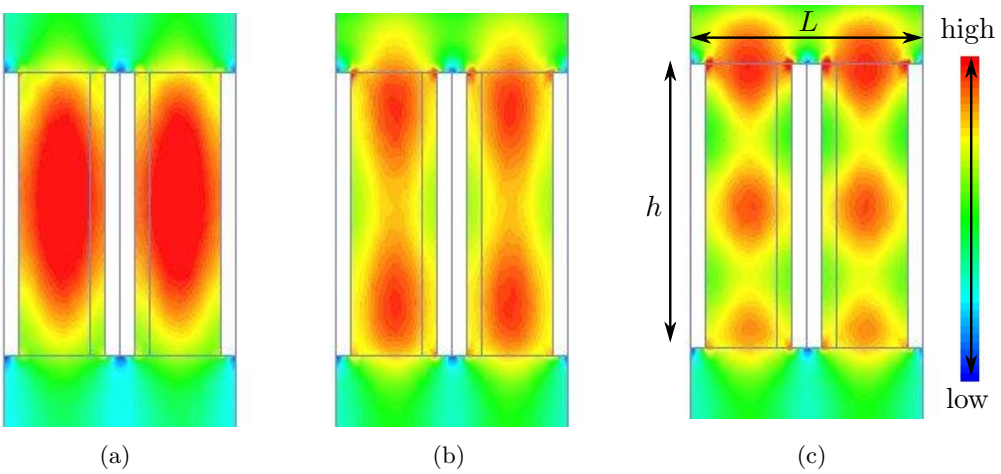

Figure 6.16: Predicted time-averaged electric field profiles (colour map) plotted at frequencies corresponding to the three lowest frequency transmission peaks ((a) - (c)) in the response of the structure to TM-polarised radiation normally incident in the $yz-$ plane. Red and blue regions correspond to a high and a field magnitude of zero, respectively.

nated with TE-polarised radiation when $\phi = 90°$, note in this orientation the incident E-field is perpendicular to the plane of mirror symmetry. Figure 6.13 (b) and Figure 6.14 (b) show the transmission spectra (grey scale) plotted on a logarithmic and linear scale respectively. Once again, a mode (bright band) is observed which, with increasing wavevector, disperses upwards in frequency above f_2, bound by the parabolic out-of-plane light line (0,1) and interacts with the mode following the $(\pm 1, 0)$ first order in-plane diffracted light lines. The eigenmodes associated with this band are represented by the squares and crosses in Figure (Fig. 6.13 (b)). Once again these correspond to the symmetric (squares) and anti-symmetric (crosses) field solutions of a coupled surface wave pair. On examining the resonant fields (vector electric fields) associated with this coupled surface wave pair on the top interface of the structure (Fig. 6.15 (b)), it is of note that the high fields (red regions) are now centred over the holes or voids and this mode can only be excited with an incident E-field that is *perpendicular* to the plane of mirror symmetry. (Note these fields closely resemble though associated with the upper band edge of the predicted band gap at $k_x = 0$ (bottom Fig. 6.11 (b)) Therefore, a TE-polarised field is required to excite this mode when the plane of incidence contains the short pitch ($\phi = 90°$) and a TM-polarised field when the plane of incidence contains the long pitch ($\phi = 0°$). As can be seen in Figure 6.14 the predicted transmission response (solid red line) of the structure at normal incidence when $\phi = 0°$ agrees well with the experimental data (red circles), and as expected from symmetry arguments agrees well with the experimental data taken at normal incidence, when TE-polarised radiation is incident in the plane containing the short axis (black triangles).

Before concluding remarks about this chapter are presented, one final issue needs to be addressed; it is observed that when the electric field of the incident radiation is perpendicular to the mirror plane (i.e.$\phi = 90°$, TE), a band of high transmission is recorded between f_1 and f_2, however, when the electric field is contained in the mirror plane, low transmission is recorded in this frequency window. In Figure 6.14 (d), which shows the transmissivity response of the structure to normally incident radiation in the plane perpendicular to the mirror plane (i.e.$\phi = 90°$, TM), a series of oscillations are observed between f_1 and f_2 (vertical dashed lines), which, in the angle dependent data (Fig. 6.5 (b) and 6.6 (b), and Fig. 6.13 (b) and 6.14 (b)), manifest themselves as a bright broad band. Each peak belongs to a family of waveguide modes associated with the first order localised resonance, f_1. With increasing frequency, the mode associated with each peak has an additional longitudinal quantisation of the field along the length of the hole (h) as can be seen in Figure 6.16 (a)-(c), where the predicted time-averaged electric fields of the first three modes, plotted in the $xz-$plane, associated with the transmission peaks at 18.75 GHz, 20.6 GHz and 23.7 GHz respectively, are shown. Red and blue regions correspond to high and low transmissivity respectively.

It is of note that in contrast this behaviour is not observed in the transmissivity response of the sample at normal incidence when the plane of incidence is contained in the mirror plane, Figure 6.14 (c); in addition to the transmission peak at approximately 16 GHz, there is simply low transmission until a second peak is observed around 29.5 GHz above f_2, hence the observation of a dark band in this frequency window in the angle dependent data (Fig. 6.5 (a) and 6.6 (a), and Fig. 6.13 (a) and 6.14 (a)). This suggests that an E-field which is contained in the mirror plane cannot excite the localised resonance f_1, whilst it is possible for an E-field that lies perpendicular to the plane of mirror symmetry.

6.7 Conclusions

In conclusion, in this chapter the intriguing behaviour of bound surface waves propagating on a reduced symmetry hole array with zigzag geometry has been investigated. Characterised by a modulation in the plane of the incident wavevector (when the plane of incidence contains the long pitch of the structure) and an orthogonal mirror plane, the zigzag hole array is formed from unit cells comprised of a pair of identical, alternately orientated, rhombic-shaped metal holes. The correct boundary conditions to support the surface modes are provided by the exponentially decaying fields at frequencies below the localised waveguide resonances within each hole. However, it is shown that their paired arrangement, which creates the symmetry specific to the zigzag geometry, enables the direct coupling of incident radiation to the supported surface modes. Further, the

unusual effect observed in its microwave transmission response, such as polarisation-selectivity of different orders and the absence of the expected band gap at the first Brillouin zone boundary, can be attributed to its unique symmetry. A comparison of the results obtained when the plane of incidence contains the shorter orthogonal pitch is also presented, and it is concluded that the orientation of the incident electric field with respect to the mirror plane is key to understanding the polarisation-dependent response of the zigzag hole array.

Chapter 7

Sievenpiper Structure with Rectangular Geometry

7.1 Introduction

In this chapter, the dispersion of the modes supported by an ultra-thin, high-impedance surface in the form of a Sievenpiper 'mushroom' structure with rectangular geometry is investigated and a comparison with the modes supported by a simpler patch array structure is presented. The anisotropy arising from the rectangular geometry is characterised. It will be shown that the behaviour of the mushroom-type structure is rather complex, particularly in comparison to a hole array with the equivalent geometry (Chapter 5). The focus therefore of this study is to fully understand the origin of the modes supported by a reduced symmetry Sievenpiper structure, a complete discussion of which is not presented in the literature.

Blade-coupling techniques and phase-resolved measurements are employed to measure directly the dispersion of both the bound transverse-magnetic (TM) *and* transverse-electric (TE) surface modes supported by the structure in the non-radiative region, whilst a free-space measurement technique is used to map the dispersion of the modes within the radiative region. Good agreement with numerical predictions is shown.

7.2 Background

Adding texture to a metal surface can greatly alter the electromagnetic boundary conditions on that surface. When the period of the structure is much less than the wavelength of the probing radiation, the structure can be assigned a surface impedance (Z_S), defined as the ratio of the tangential electric field to the tangential magnetic field at the surface. The propagation of surface waves supported on such structures can be manipulated by selecting the desired surface impedance via the surface texture.

One of the simplest ways to achieve a textured electromagnetic surface is to add a

periodic subwavelength corrugation of closely spaced, deep, vertical resonant slots to a metal slab [7–12]. A high-impedance boundary condition (i.e. small tangential magnetic field when the electric field is large) can be achieved for electric fields polarised perpendicular to the grooves upon reaching the quarter-wavelength ($\lambda/4$) resonant condition. For wavelengths four times longer than the depth of the slots, the effective surface impedance is positive and imaginary, i.e. inductive, which is the requirement for a transverse electric (TM) surface wave to be supported. Similarly, as discussed extensively within Chapters 2 of this thesis, a near-perfectly conducting substrate perforated with an array of deep, subwavelength holes can greatly alter the surface wave properties from that of a planar untextured near-perfectly conducting substrate, with the limiting frequency of the fundamental TM 'spoof' surface wave supported by such a structure being dictated by the cutoff of the holes [3]. However there are intrinsic limitations on the aforementioned textured geometries; the corrugation depth is required to be of the order $\lambda/4$ if a surface wave is to be supported by the array of resonant slots, whilst for the array of holes, the required transverse confinement of the field within the holes is of the order $\lambda/2$.

Recently low-profile structures have been developed that can alter the electromagnetic boundary condition of a metal surface that are much less than a quarter of a wavelength thick. In Sievenpiper's seminal work [53] on low-profile high-impedance surfaces (HIS), it was shown that a bound surface mode could be supported by a structure that is a fraction of the wavelength. A schematic cross-section of the Sievenpiper 'mushroom' structure together with a photograph of the top interface of the structure is shown in Figures 7.1 (a) and (b). It can be visualised as a two-dimensional version of the corrugated $\lambda/4$ slots, where the resonant cavity has been folded into a structure which has a thickness significantly less than the wavelength of the probing radiation. Comprised of an array of disconnected metal patches (also known as a frequency selective surface (FSS) [116] connected to an untextured planar metal ground plane by metal vias, thus forming a continuous conductive path. This structure can provide a high-impedance boundary condition for *both* polarisations and for all propagation directions.

These low-profile high-impedance surfaces have two desirable properties, a surface wave suppression band and a frequency band in which the reflection phase is between $\pm\pi/2$. (Note this surface wave suppression band is *not* due to the periodicity of the structure). The reflection phase is defined as the phase of the reflected electric field at the reflecting surface, referenced to the phase of the incident electric field at the reflecting surface. Perfect electrical conductors (i.e. a low impedance surface) reflect with a phase shift of π, the electric and magnetic fields have a node and antinode at the surface respectively. A perfect magnetic conductor (PMC) reflects with a phase shift of zero, the electric field at the surface has an antinode and the magnetic field a

node, resulting in a high surface impedance. At frequencies close to this PMC condition, the frequency range at which the reflection phase is between $\pm\pi/2$ and is often called the in-phase reflection band or artificial magnetic conductor (AMC) bandwidth. It is possible to tailor the parameters of the system to overlap the surface wave suppression and in-phase reflection frequency bands. Sievenpiper *et al.* studied the mushroom-type structure in this limit since it is desirable in antenna design.

When the period of the structure is small compared to the wavelength of interest, a highly simplified description of the response of the structure can be obtained by analysing the structure as an effective medium. In doing so its surface impedance can be defined by effective lumped-element circuit parameters determined by the geometry of the surface texture. An effective sheet capacitance, C, arises from capacitive coupling between adjacent patches due to their close proximity, while an inductance, L, originates from current loops within the structure (Fig. 7.1 (c)). These form a parallel resonant circuit (Fig. 7.1 (d)) that dictates the electromagnetic properties of the surface. Its surface impedance is given by the following expression

$$Z_S = \frac{j\omega L}{1 - \omega^2 LC}. \tag{7.2.1}$$

Below the resonant frequency, ω_0 of the circuit,

$$\omega_0 = \frac{1}{\sqrt{LC}}, \tag{7.2.2}$$

the surface is said to be inductive and therefore able to support bound TM surface waves, whilst above ω_0, the surface can be described as capacitive and therefore able to support TE surface modes. At frequencies close to ω_0, the surface impedance is significantly higher than that of free space and no bound surface waves are supported.

However, as well as not predicting the full band structure, in particular the presence of the surface wave suppression band, the effective medium approach, employed by Sievenpiper, provides a rather limited picture of the physical mechanism responsible for the behaviour of the structure. As previously discussed, the overlap of the surface wave suppression and in-phase reflection bands (AMC) is not a mere coincidence, and is a a key fact overlooked in Sievenpiper's original study on these high-impedance surfaces. In the literature significant efforts have been made to explain the physical origin of these two distinct phenomena [54, 117–121]. Employing finite difference time domain (FDTD) modelling techniques, Yang *et al.* [117] showed that for a specific set of parameters, the in-phase reflection band and surface wave suppression band of a Sievenpiper-type structure coincide. Using a two layer anisotropic uniaxial effective medium model, with one layer corresponding to the layer containing the vias (metallic pins) and the other to a layer containing the patches, Clavijo *et al.* [54] concluded that the surface wave

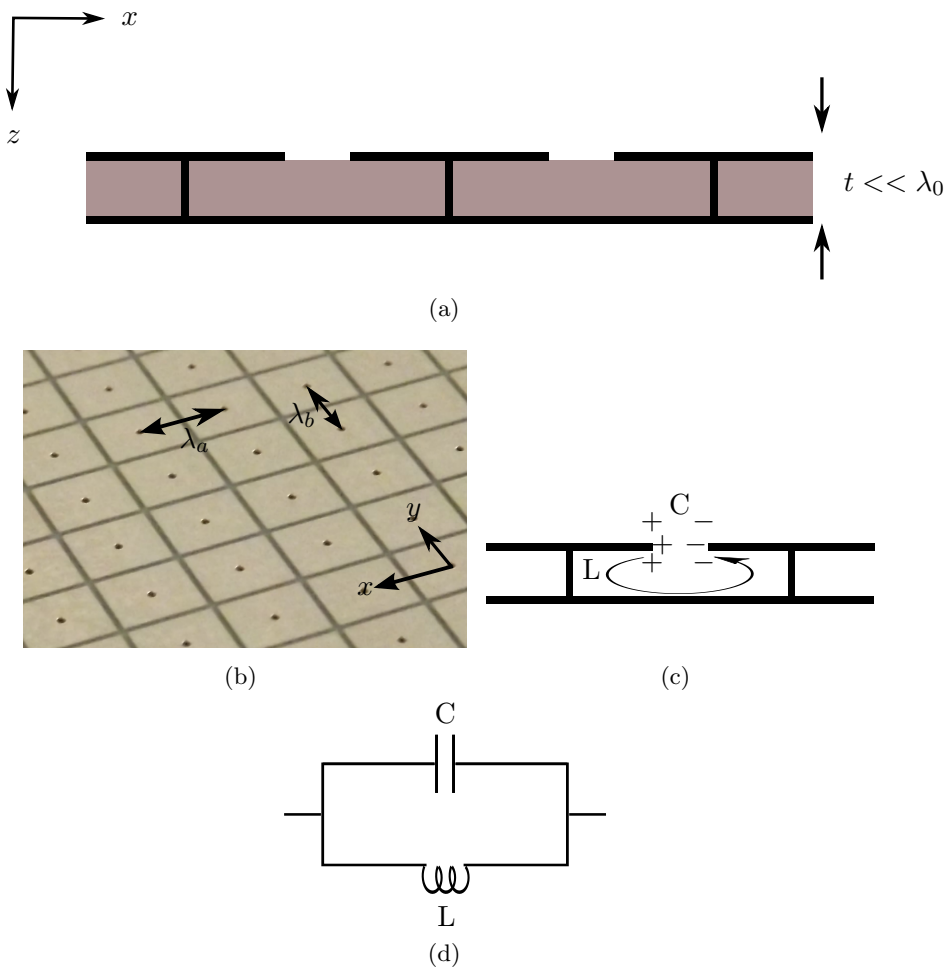

Figure 7.1: (a) Schematic representation of Sievenpiper 'mushroom' structure. (b) Photograph of the top interface of a Sievenpiper 'mushroom' structure. (c) Origin of the equivalent circuit elements (i.e. the inductance, L, and capacitance, C). (d) Equivalent circuit model for the high-impedance surface.

suppression band of a mushroom-type structure was governed by the normal components of the permittivity and permeability tensors of the via array layer, and that the band edges of the surface wave suppression and in-phase reflection bands need not correlate. Further, to study the complex behaviour of the two phenomena, Li *et al.* [120] performed parametric studies using numerical modelling techniques to ascertain how a variation in each of the characteristic parameters of the structure affected its response. Tailoring the ratio of the period of the structure to thickness of the structure was identified as a key parameter in obtaining a simultaneous in-phase reflection and surface wave suppression band.

In phase reflection bands can also be achieved from planar periodic metallic arrays printed on grounded substrates [119, 122, 123]. Goussetis *et al.* [119] discussed independently tuning the two bands on a uniplanar geometry comprising an array of disconnected metallic patches on a grounded dielectric layer. Complicated fabrication

issues were cited as a motivation for the desire to obtain the same behaviour as the mushroom-type structure but *without* the via array layer. The AMC operation was identified as being due to a resonance of the cavity formed between the periodic array of metallic elements and ground plane. However the structure in Goussetis *et al.* study, the surface wave bandgap, unlike for the mushroom-type structure, was identified as being due to the array periodicity.

In many of the studies on low-profile high-impedance surfaces the disconnected patch array comprises square patches in a square array with the via array placed centrally underneath each patch. However, a sub-category of high-impedance surfaces commonly referred to as polarisation-dependent electromagnetic band gap structures (PDEBG), have also been reported in the literature. In PDEBG structures, the symmetry of the system has been reduced such as to enable the observation of effects unobtainable in structures with a higher degree of symmetry. For instance, FDTD methods have been used to investigate the polarization-dependent reflection phase from a mushroom-type structure where the anisotropy in the system has been increased by offsetting the via array layer relative to the patch array [124, 125]. Further, the polarisation-dependent reflection phase [124], as well as the surface wave band gap characteristics [126], have been simulated using FDTD methods for a PDEBG structure in which the periodic spacing and the metal patch are both rectangular. However, an insight into the physical mechanism behind the predicted response is not discussed.

In this chapter the main focus is on the experimental characterisation of the dispersion of both the transverse magnetic (TM) and transverse electric (TE) modes supported by two highly anisotropic low-profile high-impedance surfaces and to understand the physical mechanisms behind their response. To date the experimental characterisation of the dispersion of the modes supported by the Sievenpiper mushroom structure has been limited to the studies of Lockyear *et al.* and Hibbins *et al.*. They used prism coupling techniques to couple microwave radiation to the fundamental TM [39] and TE [67] modes respectively supported by the structure. (In their studies, the periodic spacing and metal patches were both square, with each via placed centrally underneath each patch). However the disadvantage of using this technique is that the resonant frequency is shifted due to the exponentially decaying fields associated with the surface mode significantly penetrating into the wax prism. A compromise is made to achieve maximum coupling strength, whilst the resonant frequency shows some dependence on the size of the tunnelling gap between the sample and prism.

As in Chapter 5, blade-coupling techniques and phase-resolved measurements are employed to characterise the modes supported by the two structures discussed in this chapter. Advantageously this technique allows for the direct measurement of the dispersion of the modes supported by the structures without significantly perturbing the fields

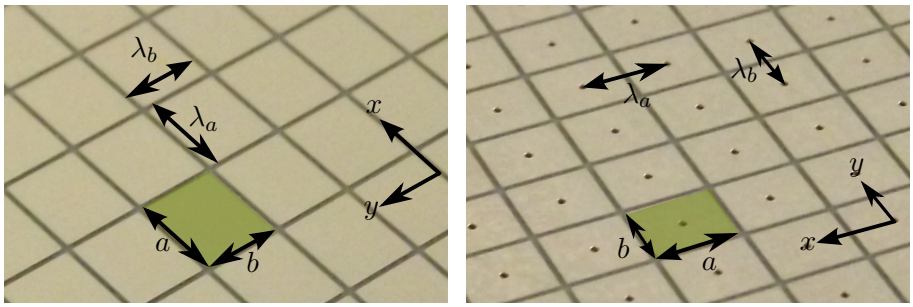

Figure 7.2: Photograph of (a) patch array and (b) Sievenpiper mushroom structure. Co-ordinate system is shown.

associated with the modes. The response of two highly anisotropic low-profile structures are considered in this chapter; a Sievenpiper mushroom-type structure, the patch array of which comprises rectangular patches in a rectangular array, and the equivalent structure without the via array, which will henceforth be referred to as the patch array structure.

As will be discussed in this chapter, the behaviour of the Sievenpiper mushroom structure in particular, is rather complex. By exploring and comparing the modes supported by a Sievenpiper-type and patch array structure, in which the symmetry of the system has been reduced (by the rectangular patches in a rectangular array), one may explore the effect that increasing the anisotropy has on the dispersion of the supported modes, thus gaining a deeper understanding of the physical mechanisms responsible for the observed effects. The anisotropy arising from the rectangular geometry is also discussed.

7.3 Experimental Samples and Techniques

Two samples constructed from standard printed circuit board (PCB) materials are considered; the first is a rectangular array of 18 μm thick copper rectangular patches of side lengths $a = 3\,\text{mm} \times b = 2.5\,\text{mm}$, separated from a continuous metal ground plane by a thin ($d_t = 0.787\,\text{mm}$) low loss dielectric layer (Nelco NY9220) characterised by a permittivity of $\epsilon = 2.22 + 0.002\text{i}$ (Fig. 7.2 (a)). The second, commonly referred to as a Sievenpiper structure (Fig. 7.2 (b)), has an additional array of copper vias of radius $r_v = 0.15\,\text{mm}$, placed centrally underneath each patch, forming an electrical connection between the patches and ground plane. The resulting structure is subwavelength with respect to the probing radiation ($7.5 < \lambda_0 < 10$ mm), with a pitch of $\lambda_a = 3.2\,\text{mm}$ in the x direction and of $\lambda_b = 2.7\,\text{mm}$ in the y direction.

Phase-resolved measurements and blade-coupling techniques, details of which can be found in Section 3.2.3, are used to experimentally characterise the dispersion of the

modes in the non-radiative region of reciprocal space (to the high wavevector side of the light line.) However, it is also necessary to study the modes in the radiative region (within the light line) in order to obtain the complete band structure. Here it is not possible to directly couple freely propagating incident radiation to the supported modes therefore a different technique is employed for determining the dispersion of the modes in this region. The resonances are observed as reflectivity minima in the specular beam due to power being dissipated into the dielectric core. From the information at which these minima occur for a discrete set of incident polar angles (θ) using a free-space measurement technique (see Section 3.2.1.3 for further details), one may characterise the dispersion of the modes in this region.

7.4 Experimental Results

7.4.1 Plane containing Short Pitch k_y

The experimentally characterised and numerically predicted modes supported by the Sievenpiper and patch array structures in both the radiative and non-radiative regions, when the plane of incidence contains the short axis of each structure, are discussed in this section. Initially we consider the modes supported within the radiative region (grey shaded region Fig. 7.3). The experimentally measured (circles) and predicted (red curve) dispersion of the modes supported by the Sievenpiper and patch array structures are shown in Figure 7.3 (a) and (b), respectively. The black dashed line corresponds to the first Brillouin zone boundary. The lowest order mode supported by the Sievenpiper structure is a TM mode (black circles Fig. 7.3 (a)) which will be referred to as the TM_0 mode from here on. Additionally, at higher frequencies, a second TM mode (TM_1) is observed (green circles, Fig. 7.3 (a)). This structure can also support TE modes, the experimentally characterised dispersion of which is represented by the blue circles in Figure 7.3 (a). On a comparison of these results to the response of the patch array structure (Figure 7.3 (b)), it can be seen that the dispersion of the TE mode (blue circles, Fig. 7.3 (b)) closely resembles that of the TE mode supported by the Sievenpiper structure, as illustrated in Ref [67]. However, it is clear that the dispersion of the TM modes change dramatically with the removal of the metal vias, with only one TM mode being supported by the patch array structure. The TM mode (green circles, Fig. 7.3 (b)) supported by the patch array structure, which will be referred to as TM_1, passes through the TE mode, approaching the same limiting frequencies as the TM_1 mode of the Sievenpiper structure defined by the Brillouin zone boundary.

As discussed previously the most striking difference in the response of the two structures is the absence of a surface wave suppression band in the dispersion of the modes supported by the patch array structure, i.e. frequencies at which a surface mode is not

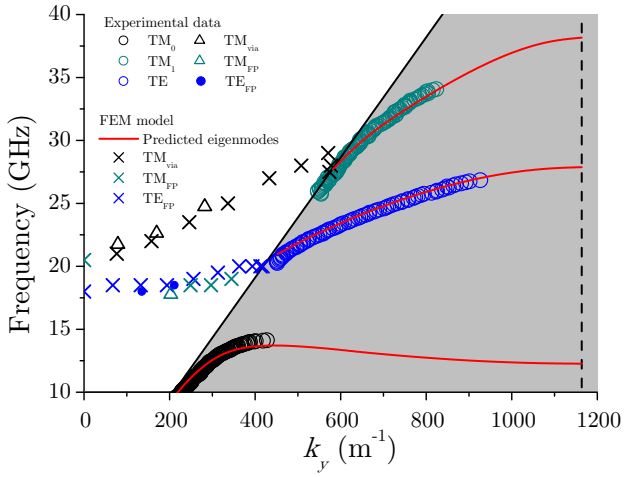

(a)

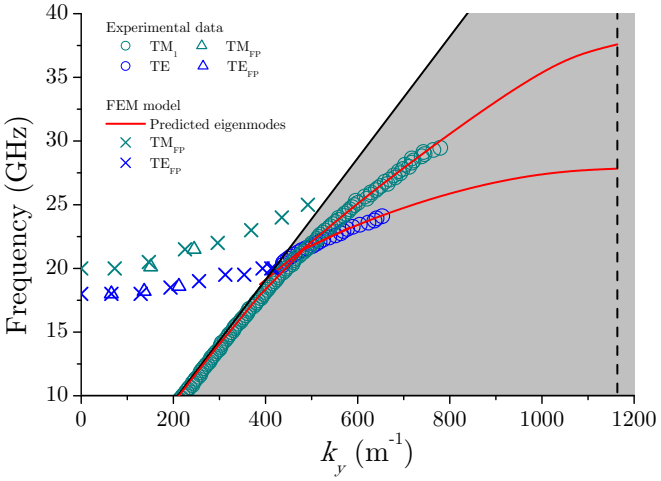

(b)

Figure 7.3: Experimentally characterised modes (circles) and predicted eigenmodes (red curves) supported within the non-radiative (grey region) by the (a) Sievenpiper and (b) patch array structure, when the plane of incidence contains the short pitch of each structure. The crosses depict the predicted minima in reflectivity associated with each mode supported by the structures within the radiative region. Whilst the triangles and closed circles represent the experimentally obtained data within this region. The black dashed line represents the first Brillouin zone boundary.

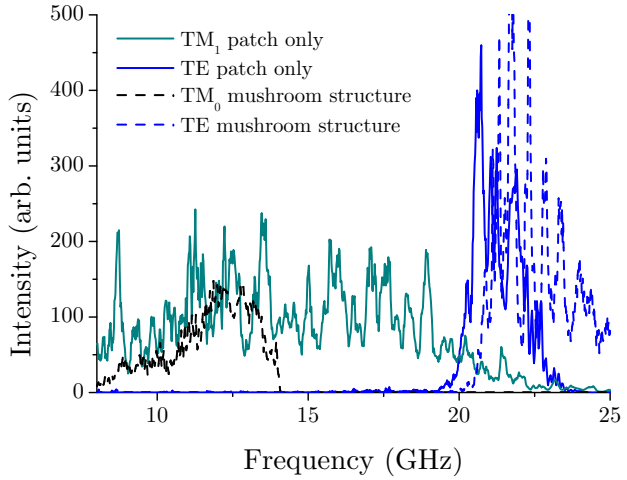

Figure 7.4: Signal measured at the detector horn associated with the TM_1 (solid green curve) and TE mode (solid blue curve) supported by the patch array structure, and the TM_0 (black dashed curve) and TE (dashed blue curve) modes associated with the Sievenpiper structure, when the plane of incidence contains the short pitch.

supported (Fig. 7.3 (a)). This is illustrated further in Figure 7.4, which shows the intensity of the signal detected at the second microwave horn when the plane of incidence contains the short pitch of each of the stuctures. Frequencies at which a signal is measured is indicative of a mode being supported by the structure. The solid green and blue lines represent the signal associated with the TM_1 and TE modes supported by the array of patches, whilst the dashed black and blue lines represent the signal associated with the TM_0 and TE modes supported by the Sievenpiper structure. It can be seen that there is a frequency band in which neither a TE or TM mode is supported by the Sievenpiper structure (i.e. zero signal) between approximately 14 GHz and 18 GHz. This behaviour is not observed in the response of the patch structure.

Next consider the modes supported in the radiative regions (Fig. 7.3) by both the Sievenpiper and patch array structures. Each cross corresponds to a predicted minimum in reflectivity in the free space measurement and each triangle and solid circle an experimentally characterised reflection minimum. In Figure 7.3 (a) one observes that the dispersion of the transverse electric mode (blue crosses) labelled TE_{FP}, originates at $k_y = 0$ and forms a continuous band with the TE mode supported within the non-radiative regions. The behaviour of the TM modes is more complicated. Whilst there is a transverse magnetic mode (green crosses), labelled TM_{FP}, the dispersion of which originates at $k_y = 0$ and continues to disperse to high frequencies with increasing wavevector, there is a second TM mode (black crosses) labelled TM_{via}. The TM_{via} mode is *not* supported when radiation is normally incident on the sample ($k_y = 0$). By

comparison with the modes supported by the patch array structure within the radiative region, it can be seen in Figure 7.3 (b) that both a TM (green crosses) and TE (blue crosses) mode, labelled TM_{FP} and TE_{FP} respectively are observed, the dispersions of which commence at $k_y = 0$ and disperse to high frequency with increasing wavevector. This TE mode forms a continuous band with the TE mode within the non-radiative region.

7.4.2 Plane containing Long Pitch (k_x)

Next the response of the Sievenpiper and patch array structures to radiation incident in the plane containing the long pitch of each structure (Figure 7.5 (a) and (b) respectively) are discussed. First consider the modes supported by the two structures within the non-radiative region, the experimentally characterised modes are depicted by the circles and the predicted eigenmodes by the red curves. It can be seen that, once again, the Sievenpiper structure supports three modes; two TM modes, labelled TM_0 (black circles) and TM_1 (green circles) and a TE mode (blue circles). As observed in the response of the patch array structure to radiation incident in the plane containing the orthogonal pitch, only two modes are supported by the patch array, a TE (blue circles) and a TM (green circles) mode. The dispersion of the lower TM mode, TM_0, is almost identical to that of the TM_0 mode supported by the mushroom-type structure when the plane of incidence contains the short pitch. It is observed however, that the higher order TM mode (TM_1) approaches the Brillouin zone boundary (black dashed line) at a lower frequency when the plane of incidence contains the longer pitch, whilst the TE mode approaches the Brillouin zone boundary at a slightly lower frequency. The same observations are made for the TM_1 and TE mode supported by the patch array structure.

Next consider the modes within the radiative region. It can be seen that for both the patch array and mushroom-type structure, a TE mode (blue crosses) labelled TE_{FP}, and TM mode (green circles) labelled TM_{FP} are supported at $k_x = 0$. Note the frequency at which these modes are supported at $k_x = 0$ are identical to those supported by the structures when the plane of incidence contains the orthogonal pitch, but are excited with the opposite polarisation. This can be understood from the rectangular geometry of the system. Further discussion about this, as well as the nature of all the modes discussed thus far will be presented later within this chapter.

7.4.3 Comparison of Experiment and Theoretical Predictions

First it is necessary to comment on the experimental data. Excellent agreement between the dispersion of the experimentally characterised modes and predicted eigenmodes (circles and red curves respectively, Fig. 7.3 and Fig. 7.5), supported by both structures

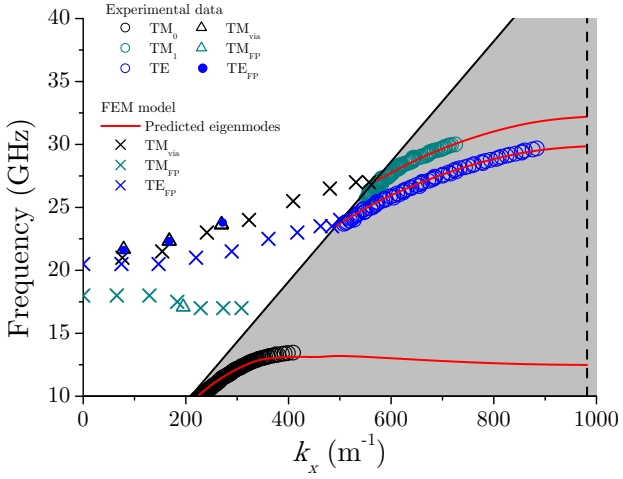

(a)

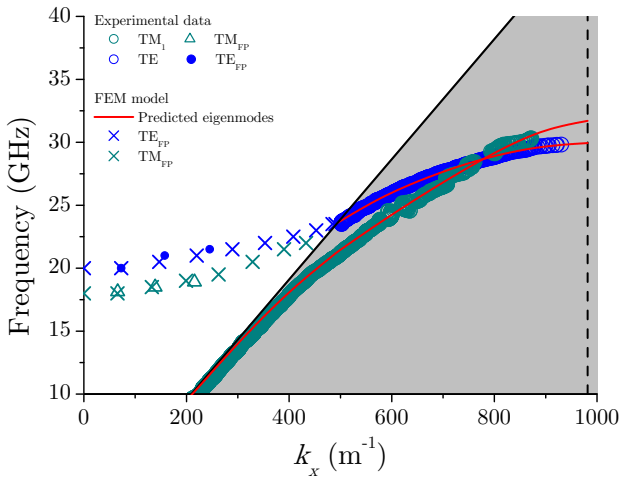

(b)

Figure 7.5: Experimentally characterised modes (circles) and predicted eigenmodes (red curves) supported within the non-radiative (grey region) by the (a) Sievenpiper and (b) patch array structures when the plane of incidence contains the long pitch of each structure. The crosses depict the predicted minima in reflectivity associated with each mode supported by the structures within the radiative region. Whilst the triangles and closed circles represent the experimentally obtained data within this region. The black dashed line represents the first Brillouin zone boundary.

in the radiative region is shown. However, it is of note that as observed in the experimental data discussed in Chapter 5, which was obtained using the same blade-coupling and phase-resolved measurement techniques, it has not been possible to characterise the modes at high values of in-plane momentum. It is proposed that the inability to characterise the mode at high k-values is due to the limitations of the experimental setup to produce an evanescent wave with all k-values with sufficiently high intensities to excite the mode.

The experimental data within the non-radiative region to the left of the light line has been obtained for three discrete angles, $\theta = 10°, 22°$ and $33°$, where θ is the angle measured between the wavevector of the incident radiation and the normal to the structure. (Note this data was recorded by Ben Tremain and reproduced with permission.) In general, good agreement is shown between experimental data (squares) and the predicted minima in reflectivity (crosses) in terms of the frequency at which the mode is supported. However, for the lowest frequency TM mode labelled $\mathrm{TM_{FP}}$ (green square) supported by the Sievenpiper structure when the plane of incidence contains the long pitch (Fig. 7.5 (a)), where the mode is particularly broad and shallow, it has been difficult to accurately experimentally obtain the resonant frequency of this mode. Further, the agreement between the measured TE mode (solid blue circles) and predicted minima in reflectivity (blue crosses) supported by the same structure, also when the plane of incidence contains the long pitch, is particularly poor. Indeed the dispersion of the mode appears to follow that as predicted and experimentally measured for the $\mathrm{TM_{FP}}$ mode. Since the equivalent mode supported by the patch array structure does not show such discrepancies between the predicted and experimentally measured response, it therefore can be concluded that an additional anisotropy within the via array layer is responsible for the observed discrepancy. Indeed further modelling (not shown) reveals that this TE mode is highly sensitive to the via array layer when it is tilted with respect to the normal of the patch array layer, in the plane perpendicular to the plane of incidence.

7.5 Via-Array Thickness Dependence

Exploring the dependence of the modes supported by the mushroom-type structure on the thickness of the dielectric layer (i.e. the thickness of the via array) reveals important information about the nature and origin of the modes. Fig. 7.6 shows the predicted response of the mushroom-type structure when the plane of incidence contains the long pitch, for dielectric layers of thickness (a) 0.395 mm, (b) 0.787 mm, and (c) 1.517 mm. One of the key observations is the fact that the dispersion of the mode labelled TM_{via} (black crosses) shows a relatively weak dependence on the thickness of the via array layer, compared to the dispersion of the modes labelled $\mathrm{TM_{FP}}$ and $\mathrm{TE_{FP}}$ (green and

blue crosses, respectively). Additionally the lowest order TM mode (TM_0) within the radiative region (black curves) also displays a strong dependence on the thickness of the dielectric layer. Further discussion of these observations will be presented in Section 7.6.

The fundamental resonant frequency of these structures can be calculated from the geometrical parameters using an effective medium surface impedance (Z_s). In the limit of $\lambda_{a,b} < \lambda_0$ and for normal incidence radiation, Z_s may be expressed as [127]

$$Z_s = \frac{j\frac{\eta}{\sqrt{\epsilon_r}}\tan(k'h)}{1 - \frac{(\epsilon_r+1)kD}{pi\sqrt{\epsilon_r}}\log\frac{2D}{\pi\omega}\tan(k'h)}. \tag{7.5.1}$$

Here w represents the distance between nearest neighboring patches, ϵ_r and h are the dielectric constant and thickness of the dielectric core respectively, η is the free space impedance and $k' = \frac{k}{\sqrt{\epsilon_r}}$ where k is the free space wavevector. By plotting Z_s as a function of k the resonant frequency of the structure can be obtained from the pole in equation 7.5.1. Numerically solving this equation for a dielectric thickness of (a) 0.395 mm, (b) 0.787 mm, and (c) 1.517 mm predicts resonant frequencies at 27.14 GHz, 21.1 GHz and 12.9 GHz respectively (red dashed lines on Fig. 7.6 (a)-(c)). Thus revealing a strong dependence on the thickness of the dielectric layer, and suggesting that the fundamental resonance is due to a cavity mode in the dielectric core. The reader should however treat the significance of these calculated resonant frequencies with caution, since equation 7.5.1 is only valid when $\lambda_{a,b} < d_t$, which is not true for the structures considered in this work. They should be used as a guide to physical understanding only.

7.6 Discussion

A deeper discussion of the modes supported by both structures, including the resonant fields associated with each mode, is presented in the following sections. It will be shown that the modes supported by the mushroom-type structure can be divided into two categories, those whose existence relies on the via array layer and those which do not. Before this discussion a brief summary of the key results discussed in Sections 7.4.1, 7.4.2 and 7.5 is presented.

- A transverse electric mode is supported by both the patch array and mushroom-type structures, the dispersion of which is identical for both structures. The mode commences at $k_{x,y} = 0$ and forms a continuous band with the TE mode supported within the non-radiative region.

- Two transverse magnetic modes are observed in both the radiative and non-radiative regions in the response of the mushroom-type structure, whilst only one

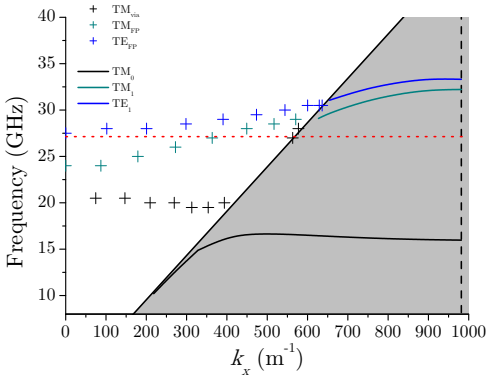

(a)

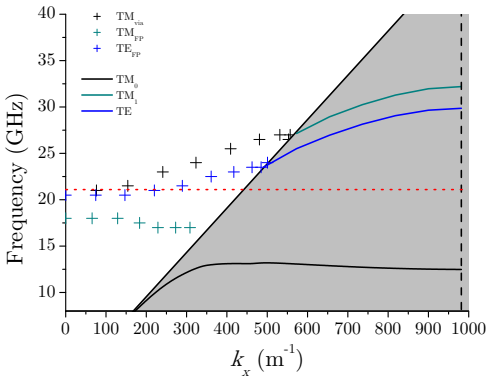

(b)

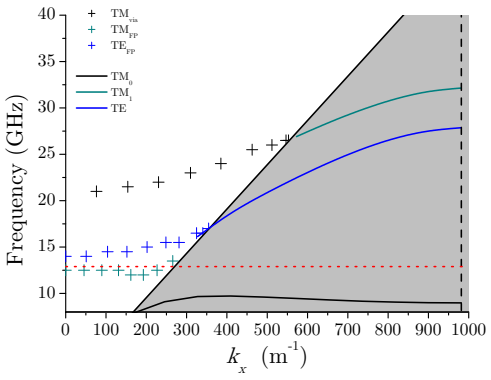

(c)

Figure 7.6: Predicted eigenmodes (solid lines) and minima in reflectivity (crosses) associated with the modes supported by the Sievenpier mushroom structure within the non-radiative and radiative region respectively, when the plane of incidence contains the long pitch, for dielectric layers of thickness (a) 0.395 mm, (b) 0.787 mm, and (c) 1.517 mm. The black dashed line represents the first Brillouin zone boundary. The red dotted lines correspond to the resonant frequency as predicted by expression 7.5.1.

is observed in the response of the patch array structure.

- The dispersion of one of the transverse magnetic modes (TM_{FP}) is observed at $k_{x,y} = 0$, whilst the other TM mode (TM_{via}) is only observed when $k_{x,y} \neq 0$.
- The frequency at which the $(TE/TM)_{FP}$ pair are supported when radiation is normally incident on the structure, are polarisation dependent.
- The dispersion of the pair of $(TE/TM)_{FP}$ modes within the radiative region, which are observed at $k_{x,y} = 0$, are strongly dependent on the thickness of the structure, whilst the dispersion of the other TM mode (TM_{via}) is only weakly dependent on the thickness of the via-array layer.
- A surface wave suppression band is observed in the response of the mushroom-type structure which is not present in the response of the patch array.

7.6.1 TE Mode

In this section the transverse electric (TE) mode, previously shown to be supported by both the patch array and the mushroom-type structures (Fig. 7.3 and Fig. 7.5) is discussed. It has been observed that the dispersion of the TE mode is almost identical for both structures, thus suggesting the mode is insensitive to the presence of the metal vias. This observation can be understood by considering that when the polarisation of the incoming wave is TE, the E-field is parallel to the ground plane and it does *not* interact with the metallic vias. Essentially the textured substrate (via array layer) is equivalent to a dielectric slab backed by a PEC substrate, with an array of patches on top.

The predicted time-averaged (colour map) and instantaneous (arrows) magnetic field profile of the TE mode supported by the Sievenpiper structure, plotted in the xz-plane, when the plane of incidence contains the long pitch of the structure (plotted at $k_x = 818\ \mathrm{m}^{-1}$) are shown in Figure 7.7 (a). Red and blue regions correspond to high and zero fields magnitude respectively. The mode is characterised by looping magnetic fields around the patch. High fields (red regions) are observed between the patches. On examining the time-averaged (colour map) and instantaneous (arrows) electric fields plotted in a plane parallel to the $xy-$plane, at the centre of the dielectric layer (Fig. 7.7 (b)), it can be seen that the mode is strongly quantised along the short pitch of the structure. On examining the equivalent modes to those shown for the mushroom structure in Fig. 7.7 (a) and (b), for the patch array structure (Fig. 7.7 (c) and (d)), it can be seen that the field profiles are very similar, and as expected the presence of the via array perturbs the fields minimally.

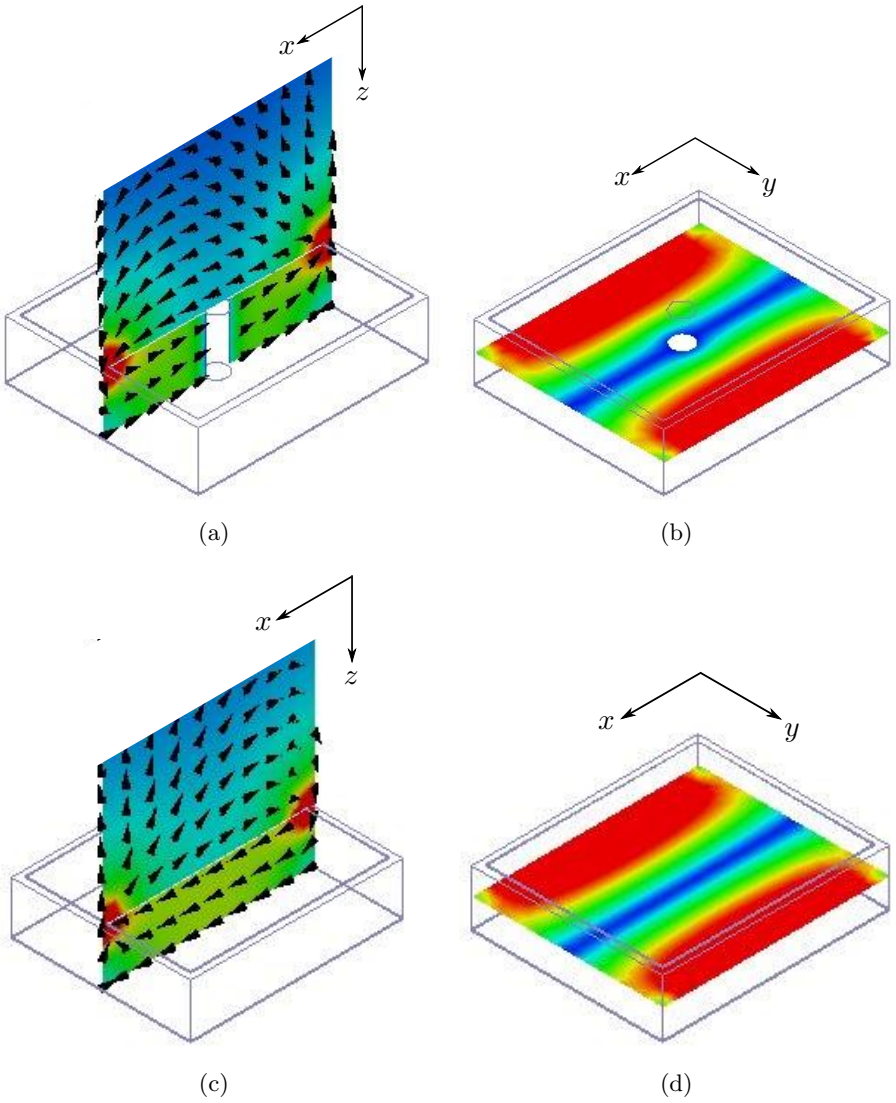

Figure 7.7: Time-averaged (colour) and instantaneous (arrows) (a) magnetic field plotted in the xz-plane and (b) electric field plotted in the xy-plane, associated with the TE mode supported by the mushroom-type structure, plotted at $k_x = 818\ \mathrm{m}^{-1}$. Time-averaged (colour) and instantaneous vector (c) magnetic field plotted in the xz-plane and (d) electric field plotted in the xy-plane, associated with the TE mode for the patch array structure, plotted at $k_x = 818\ \mathrm{m}^{-1}$. Red and blue regions correspond to a high and zero field magnitude, respectively.

The TE mode can be described as a Fabry-Perot (FP)-like mode guided by the dielectric layer. It can be viewed simply as a modified version of the fundamental mode supported by a grounded dielectric slab, with a perturbation attributed to the array of patches. For a grounded dielectric slab a family of modes are supported at frequencies corresponding to integer number of $\lambda/4$ quantisations within the layer. The tangential electric-field must fall to zero at the ground plane, and the boundary between the dielectric layer and air will act as a poor mirror. These modes are supported above a cutoff frequency determined by the thickness of the structure and the permittivity of the slab (ϵ) [76]. The cutoff frequency is determined by equation

$$f = \frac{c}{4t\sqrt{\epsilon - 1}}, \tag{7.6.1}$$

where t is the thickness of the structure and ϵ is the permittivity of the dielectric layer.

Now we introduce the patch array layer back into the system. The field will be highly compressed in the patch layer and it will have a much higher reflection coefficient as the layer can be considered as having a very high permittivity. The total phase shift supplied by the array of patches and the substrate must be equivalent to one quarter of a wavelength. The mode commences at $k_{x,y} = 0$ at the 'skewed' $\lambda/4$ resonance and disperses upwards in frequency, passing through the light line and forming a continuous band with the non-radiative branch of the mode, where it is a trapped mode with evanescent decay into the air. At the Brillouin zone boundary the group velocity of the mode must fall to zero, however this is an artificial limiting frequency, purely dictated by the periodicity of the structure. As expected for a Fabry-Perot (F-P)-type mode, this mode is highly dependent on the thickness of the structure as shown in Figure 7.6. Note that due to the rectangular geometry of the structure, the frequency at which the mode originates is also polarisation-dependent.

7.6.2 TM_1 Mode

A grounded dielectric slab can also support transverse magnetic modes [76]. It is not surprising therefore that a TM F-P-type mode is also observed in the response of both the Sievenpiper and patch array structure. The fundamental TM mode supported by a grounded dielectric slab does not have a cutoff frequency, a TM mode can be supported for arbitrary thicknesses. The mode is characterised by a dispersion to the high-wavevector side of the light line, originating from the origin. Relating this to the patch array structure, it can be seen that the dispersion of the fundamental TM mode (TM_1) in the non-radiative region (green circles, Fig. 7.3 (b) and Fig. 7.5 (b)) closely follows the light line at low frequencies, experiencing a limiting frequency due to the periodicity

of the structure at the Brillouin zone boundary. Due to the in-plane anisotropy of the structures, this limiting frequency will be dependent upon the pitch contained within the plane of incidence. For the Sievenpiper structure the TM_1 mode (green circles Fig. 7.3 (a) and Fig. 7.5 (a)) is only supported at frequencies above the TE mode. Note that this mode is not predicted by the effective medium approximation, in which, above the resonant frequency, the impedance of system is said to be capacitive, and only able to support TE modes.

The predicted time-averaged (colour map) and instantaneous vector (arrows) electric fields plotted in the xz-plane at $k_x = 818\,\mathrm{m}^{-1}$ associated with the TM_1 mode supported by the Sievenpiper structure and patch array structure are shown in Figure 7.8 (a) and (c), respectively. Red and blue regions correspond to high and zero field magnitude respectively. Figure 7.8 (b) and (d) show the predicted time-averaged (colour map) and instantaneous vector (arrows) electric field profiles plotted in the xy-plane at the centre of the dielectric layer at $k_x = 818\mathrm{m}^{-1}$ of the TM_1 mode supported by the Sievenpiper and patch array structure, respectively. It can be seen that the mode is strongly quantised along the long pitch of the structure underneath the patch. Note the fundamental TM mode supported by the patch structure is analogous to the fundamental TE waveguide mode supported by a rectangular hole within a PEC substrate.

In the radiative region a F-P-like guided mode, similar to the TE mode discussed in the previous section, is observed. The predicted dispersion of this mode is depicted by the green crosses in Fig. 7.3 (b) and 7.5 (b). Obviously, for a square geometry, the frequency at which these two modes would occur at $\mathrm{k}_{x,y} = 0$ would be degenerate. However, for the rectangular geometry under consideration in this study, the two modes split, with each polarisation sensitive to orthogonal periodicities. It is also shown that the TM_{FP} mode disperses differently with frequency for the case when there is a via array layer within the dielectric when compared to the no-via. This is expected, since the incident electric field contains a component normal to the via array layer.

7.6.3 TM_0 Mode

The second family of transverse magnetic (TM) modes are associated with the via array layer and are only supported by the Sievenpiper structure. In fact it will be shown that their existence is reliant on the presence of the via array layer. The time-averaged (colour map) and instantaneous (arrows) electric field profile, plotted in the xz-plane, associated with the TM_0 mode (black circles Fig. 7.3 (a) and Fig. 7.3 (a)) at a value of $k_x = 818\,\mathrm{m}^{-1}$ is shown in Figure 7.9 (a). Red and blue regions correspond to high and zero field magnitude, respectively. It can be seen that the mode is characterised by electric fields looping around the patches and metallic pins. On examining the time-averaged (colour map) and instantaneous (arrows) magnetic field profile in the xy- plane

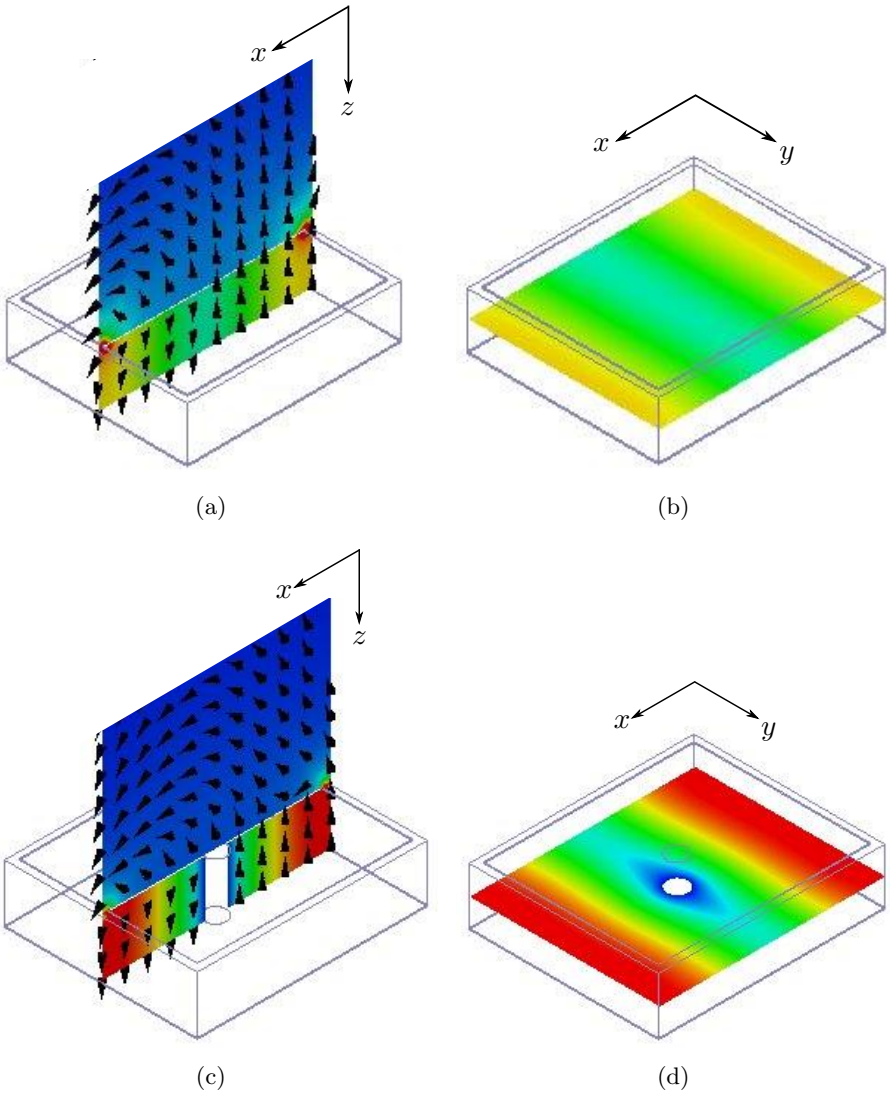

Figure 7.8: Time-averaged (colour map) and instantaneous (arrows) (a) magnetic field plotted in the xz-plane and (b) electric field plotted in the xy-plane, associated with the TM_1 mode supported by the mushroom-type structure, plotted at $k_x = 818\ \mathrm{m}^{-1}$. Time-averaged (colour map) and instantaneous (arrows) (c) magnetic field plotted in the xz-plane and (d) electric field plotted in the xy-plane, associated with the TM_1 mode for the patch array structure, plotted at $k_x = 818\ \mathrm{m}^{-1}$. Red and blue regions correspond to a high and zero field magnitude, respectively.

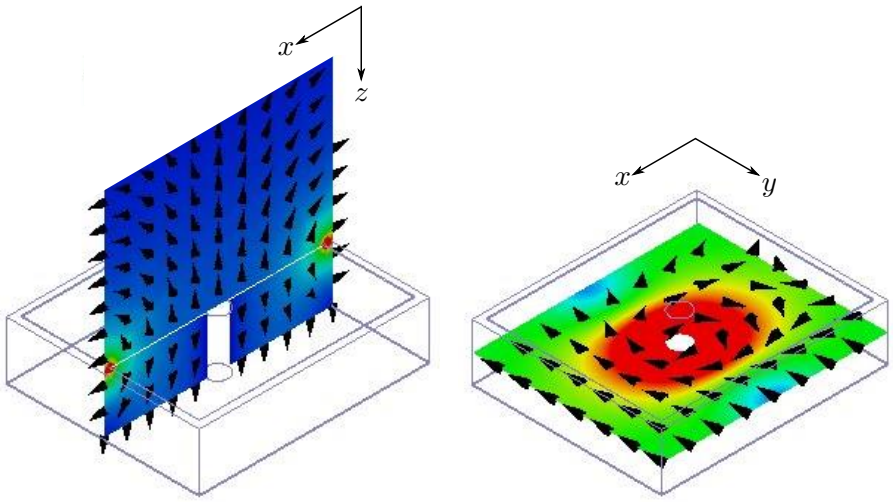

Figure 7.9: Time-averaged (colour map) and instantaneous (arrows) (a) magnetic field profile in the xz-plane and (b) electric field plotted in the xy-plane, associated with the TM_1 mode for the mushroom-type structure, plotted at $k_x = 818\text{m}^{-1}$. Red and blue regions correspond to a high and zero field magnitude respectively.

at the centre of the dielectric core, it can be seen that unlike for the TE and TM_1 modes, the associated fields of which are strongly quantised along the length of the patch, the magnetic fields have a strong circumferential component. It is clear this mode is associated with the via array layer.

This mode can only ever be excited by an incident field with an electric vector component normal to the array of pins (i.e. the via array layer). Therefore, as discussed previously, the mode associated with the via array layer within the radiative region labelled TM_{via} (black crosses and squares Fig. 7.3 (a) and Fig. 7.5 (a)) can only be supported when $k_{x,y} \neq 0$. It is also worth reminding the reader that the dispersion of this mode within the radiative region is independent of the thickness of the via array layer, the reason for this will be discussed in due course. The fundamental transverse magnetic mode (TM_0) supported by the mushroom structure in the non-radiative region (black circles Fig. 7.3 (a) and Fig. 7.5 (a)) closely follow the light line at low frequencies and at high values of wavevector the mode is characterised by a negative dispersion (the physical mechanism behind which will be discussed later on in this chapter). It also defines the lower band edge of a surface wave suppression band that occurs between the fundamental TM mode and fundamental TE mode.

The via array (i.e. a regular lattice of ideally conducting wires with small radii compared to the lattice period and wavelength) in microwave applications is known as an artificial dielectric or rodded medium [128, 129]. For electric fields polarised parallel

to the wires, the medium is characterised by a frequency-dependent effective dielectric constant, with an effective plasma frequency [129]. Assuming the wires are very thin, for electric-field polarisation perpendicular to the wires, the effective permittivity is ϵ_r (i.e. that of the surrounding medium). Clavijo [54] showed that the Sievenpiper mushroom structure also exhibits a frequency-dependent permittivity. Adopting an effective medium approach, Clavijo *et al.* modelled the structure as a two-layer anisotropic uniaxial material in both permittivity and permeability, with the top layer representing the array of patches and the bottom layer the via-array substrate. It was shown that the via array layer is highly anisotropic; the effective permittivity in the direction normal to the surface (ϵ_z) is characterised by a Drude-like dispersion with a negative real part up to a cutoff 'plasma' frequency, whilst in the transverse direction ϵ_x and ϵ_y are equal and positive. In other words ϵ_z exhibits a 'plasmonic' response.

The surface mode supported at the interface between a plasmonic metal and a dielectric will asymptotically approach a limiting frequency when the real part of the dielectric function is equal but opposite to the real part of the dielectric function of the dielectric, i.e. the 'cutoff' frequency described by Clavijo. At higher frequencies, when the dielectric functions of both the metal and dielectric are positive, the mode is no longer bound to the surface. Specifically at the plasma frequency, the real part of the permittivity is zero, and the wavelength inside the material tends to infinity. The predicted insensitivity of the TM_{via} mode (which is supported within the radiative region) to the thickness of the via array layer (Fig. 7.6) can be explained using the plasmonic analogy; the frequency at which the dispersion of the mode originates within the radiative region corresponds to the frequency at which the effective permittivity is zero and a small change in the thickness of the via array layer is not expected to perturb the dispersion of the mode significantly. Further the insensitivity of the dispersion of the TM_0 mode to the periodicity of the structure (i.e. whether the plane of incidence contains the long or short axis) can also be explained by the fact that this mode is highly dependent on the properties of the via array layer and not the array of patches. Therefore the anisotropy within the patch array layer will not have a strong effect. However a variation in the thickness of the dielectric core (via array layer), will strongly affect the dispersion of this mode as shown in Figure 7.6.

The origin of the negative dispersion of the lowest order TM mode (TM_0) supported by the Sievenpiper structure in the non-radiative regime can be understood by considering the ratio of the power flow associated with the mode in the dielectric region above the structure, and within the via array layer. An effective medium model has been employed to produce the modelling discussed in the remainder of this thesis. The work has been undertaken by Dr Ian Hooper and is reproduced with permission. The reflectivity and field profiles have been calculated using an in-house multilayer optics

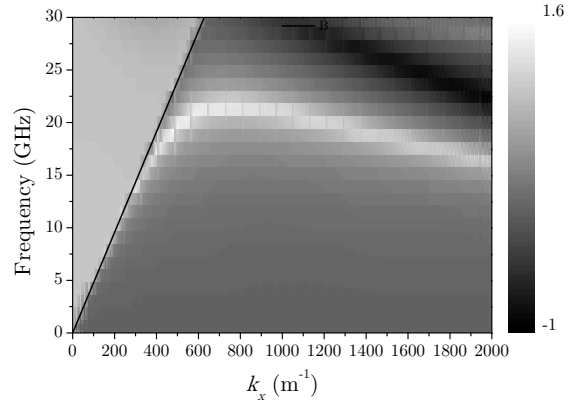

(a)

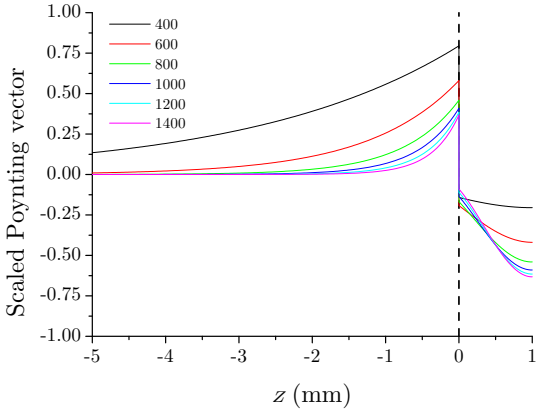

(b)

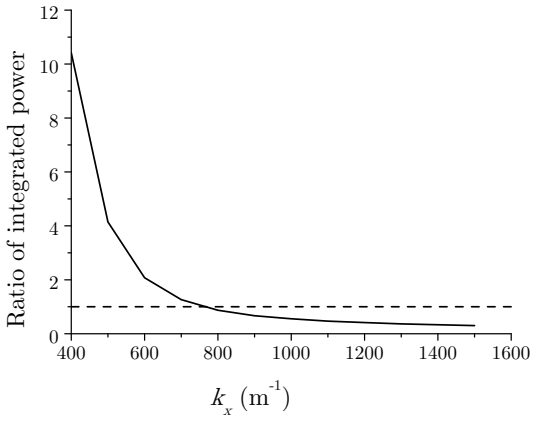

(c)

Figure 7.10: (a) Magnitude of reflection coefficient (grey scale) plotted on a $\log_{10}$ scale. (b) Scaled Poynting vector in medium 1 and medium 2 as a function of distance z in mm normal to the structure, for different values (solid lines) of in-plane wavevector (k_x). The dashed line represents the boundary between the two media. (c) Ratio of the magnitude of the integrated power in the two media (solid line). The horizontal dashed line represents the point at which the power flow into each medium is equal.

code based on the 4x4 Berreman method [130], and allows the fields of both radiative and non-radiative modes to be calculated.

The system under consideration is a 1 mm thick anisotropic medium upon a ground plane, referred to as medium one and represents the via layer of the Sievenpiper structure. The patch array structure is not needed in order to replicate the TM_0 mode. The normal component of the permittivity tensor of the layer is given by $\epsilon = 2.2 + 0.1i - \frac{\omega_p^2}{\omega^2}$, and the in-plane permittivity given by $\epsilon = 2.2 + 0.1\text{i}$. Medium two, which bounds medium one is air. The predicted dispersion of the mode supported by structure is shown in Figure 7.10 (a). The grey scale represents the magnitude of the reflection coefficient on a $\log_{10}$ scale. Since bound modes correspond to poles in the reflection coefficient, white regions to the high wavector side of the light line (solid black like) represent the dispersion of the mode. At high wavevector the mode is characterised by a negative dispersion, in agreement with numerical predictions in Figure 7.3 (a) and Fig. 7.5 (a).

The fields of the modes for various values of k_x have been obtained and used to calculate the Poynting vector (Figure 7.10 (b)) as a function of distance through the system (where $z = 0$ is the boundary between the two media), the Poynting vector has been scaled for clarity (solid lines). It can be seen that power flow in each medium is strongly dependent on k_x. Note that due to the negative value of the normal component of the permittivty, the power flow in medium one is in the opposite direction to that in the bounding dielectric. At $k_x = 400\,\text{m}^{-1}$ (black curve), a much greater portion of the power flow is in the dielectric region, whilst at $k_x = 1400\,\text{m}^{-1}$, a greater portion of the power flow is in medium one. Note that maximum power flow is at the ground plane (i.e. $z = 1\,\text{mm}$) in medium one, indicating that the mode resembles a guided mode in region one. The ratio of the magnitude of the integrated power in each medium is shown in Figure 7.10 (c). Here the horizontal line is indicative of where the power flow in each medium is equal, which corresponds to the value of $k_x \approx 765\text{m}^{-1}$. Since the power flow is in opposite directions in each medium, the net power flow is zero. On inspection of Figure 7.10 (a) one notes that this value of k_x corresponds to the region of the dispersion with zero group velocity as one would expect. For wavevectors less than this, a greater portion of the power is in the dielectric region than in medium one and the dispersion of the mode is positive, whilst at wavevectors greater than this, more power flow is in medium one and the dispersion of the mode is negative.

7.7 Conclusions

In this chapter the anisotropy arising from the rectangular geometry of a Sievenpiper 'mushroom' structure and a similar patch-array structure have been characterised. Blade-

coupling techniques and phase-resolved measurements have been used to directly measure the dispersion of both the TM and TE modes supported by the structure in the non-radiative region. It has been revealed that two families of modes are supported by the Sievenpiper structure, with the existence of one family dependent on the via array layer and a second displaying similar character to those supported by the patch array structure. Further it has been discussed that via array layer within the Sievenpiper structure is highly anisotropic; with an effective permittivity in the direction normal to the surface characterised by a Drude-like dispersion with a negative part up to a cutoff 'plasma' frequency. Lastly it is shown that the dispersion of the lowest order TM mode supported by the Sievenpiper structure in the non-radiative region is determined by the relative power flow of the mode in the via-array layer and the region which it bounds.

Chapter 8

Conclusions and Future Work

8.1 Summary of Thesis

The work presented in this thesis focuses on the experimental investigation of structurally-dictated or 'spoof' surface waves supported by periodically textured metallic (pseudo-plasmonic) structures in the microwave regime. Two different geometries are considered; a near-perfectly conducting substrate perforated with an array of periodic holes and the Sievenpiper 'mushroom' structure, a discussion of the limiting frequency of the modes supported by which, has been presented. Through the work discussed in this thesis, it has been shown that increasing the anisotropy of a structure through the modification of the shape and/or arrangement of the constituent subwavelength elements allows access to modes and phenomena unavailable in structures with higher symmetry.

In Chapter 4, 5 and 6, the geometry upon which the propagation of surface waves has been studied is that of near-perfectly conducting substrates perforated with arrays of holes. They have been investigated at frequencies close to the fundamental resonance of the holes (dictated by the cutoff frequency of the hole). Initially, in Chapter 4 an array of holes with square geometry is considered. The holes are close-ended and the azimuthally-dependent reflectivity response of the structure, at a fixed polar angle, has been used to obtained information about the modes supported by the structure. Due to its high symmetry, it serves as an ideal structure for investigating grating-coupling to surface modes supported by the hole array. Since the structure and wavelength of the probing radiation are comparable at frequencies close to the fundamental resonance of the hole (i.e. the limiting frequency of the surface mode), it has been shown that the position of the coupling-in grating, relative to the hole array, can greatly alter the dispersion of the surface modes supported by the structure.

It has also been shown in Chapter 4 that when the grating, which has a periodicity ($2d$) twice that of the pitch of the hole array, comprises metallic rods and is placed on top of the metal regions of the hole array, a single mode is observed below the fundamental resonance of the hole array. This mode is the lowest order surface wave supported

by the structure. However, when the metallic coupling in grating is placed over the dielectric regions of the hole array (at a position of $a/3 : 2a/3$, such as to maintain the $2d$ periodicity of the structure and equivalent boundary conditions on each hole) it is found that two modes are observed at frequencies below the fundamental resonance of the hole array. These modes correspond to the upper and lower band edges, of the lowest order surface wave, supported at frequencies below the fundamental resonance of the hole. The observation of these modes is attributed to the reduced symmetry of the coupling-grating. Of particular note is the ability to 'switch off' the broad deep mode, associated with the upper band edge of the surface mode, supported below the fundamental resonance of the hole array, by breaking electrical contact between the substrate and the grating. This is attributed to the field distribution of this mode not being maintained when the electrical connection is broken. Good agreement with numerical predictions is shown.

In Chapters 5 and 6, the concept of pseudo-plasmonic surfaces has been extended to include structures with a high degree of surface symmetry. In Chapter 5, the fundamental resonance in the orthogonal directions is different, therefore the frequency to which the dispersion of the surface waves supported by the structure is limited, varies with sample orientation, resulting in an ellipsoid of limiting frequencies. The surface asymmetry of the rectangular hole array studied in this chapter provides an additional degree of freedom in the manipulation of designer surface waves. Whilst the width of the hole in one direction (i.e. $a\hat{\mathbf{x}}$) dictates the resonant frequency for an incident polarisation (electric vector) directed along the y-direction, the pitch in the orthogonal direction (i.e.$\lambda_b\hat{\mathbf{y}}$) dictates the onset of diffraction. New capabilities of directly measuring the dispersion of the mode were employed, in particular the technique for obtaining the dispersion of the higher-order modes was developed.

In Chapter 5, it was shown that when the incident plane contained the short pitch of the structure, the family of surface modes associated with the quantisation of the field within the holes along the orthogonal direction could readily be measured in the non-diffracting regime. This is because the onset of diffraction occurs significantly above the fundamental resonance of the array of holes. However when the plane of incidence contains the orthogonal longer pitch, the surface mode approaches its limiting frequency above the onset of diffraction. It does so whilst displaying very limited dispersion. The experimentally observed results agree well with numerical predictions.

A reduced-symmetry hole array with zigzag geometry, characterised by a modulation in the plane of the incident wavevector (when the plane of incidence contains the long pitch of the structure) and an orthogonal mirror plane has been discussed in Chapter 6. The recorded 'enhanced transmission' through the hole array, is attributed to the excitation of diffractively coupled surface waves. Due to the inherent periodicity of

the zigzag structure, unlike in Chapter 4, direct coupling of incident radiation to the surface modes can be achieved, without the requirement of an additional coupling-in grating. Further, due to the reduced symmetry of the zigzag hole array, polarisation-dependent excitation of individual surface wave bands is observed. It is concluded that, as confirmed by numerical predictions, the orientation of the incident electric field with respect to the mirror plane is key to understanding the polarisation-dependent response of the zigzag hole array.

Finally in Chapter 7, a low-profile sample in the form of a Sievenpiper 'mushroom' structure is investigated, it is also shown to support structurally-dictated surface modes, the dispersion of which have been directly mapped using blade-coupling and phase-resolved measurement techniques (as in Chapter 5). The response of the structure is shown to be rather complex when compared for instance, to the response of a patch array with a similar geometry or indeed a hole array with the same symmetry. Both transverse electric (TE) and transverse magnetic (TM) modes are supported by the Sievenpiper structure (unlike for the hole array structures which are only capable of supporting TM modes). The anisotropy arising from the rectangular geometry of the Sievenpiper structure is characterised and compared to a more simple patch array structure with the equivalent symmetry. The 'plasmonic'-like response of the normal permittivity of the via array is discussed. Modelling the via array layer as thick anisotropic medium upon a ground plane, the fields of the mode supported by this layer, for various values of in-plane wavevector have been obtained and used to calculate the Poynting vector as a function of distance through the system. From this it has been shown that the dispersion of the lowest order TM surface mode supported by the Sievenpiper structure is dictated by the relative power flow of the fields of the surface mode in the via array region and the bounding medium. The finding presented in this chapter show that a deeper understanding of the origin of the modes supported by the structure have been obtained, thus extending previous knowledge of the structure reported in the literature.

8.2 Future Work

Possible suggestions for extending the work in this thesis include investigations into hole arrays and Sievenpiper (and the simpler patch array) structures with symmetries further reduced than those discussed within this thesis.

For example, within Chapter 6 of this thesis, it was shown that the polarisation-dependent excitation of the individual surface waves band was attributed to the reduced symmetry of the system. It was shown that the orientation of the electric vector with respect to the mirror plane was key to understanding the response of the structure. However, it may be potentially interesting to investigate a hole array with zigzag geom-

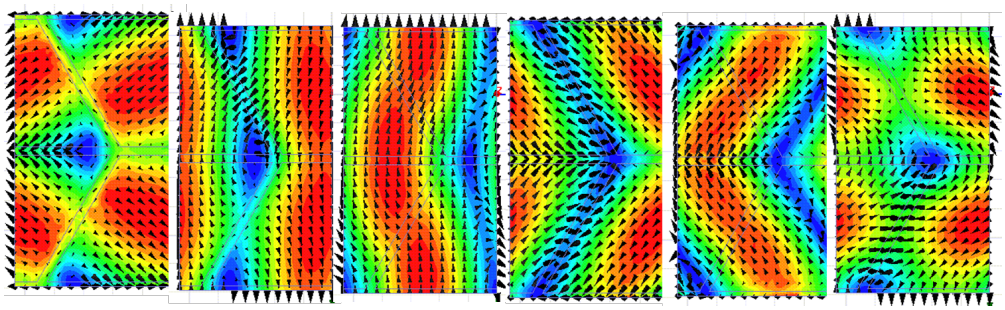

(a)

Figure 8.1: Time-averaged (colour map) and instantaneous vector electric fields (arrows), plotted in the centre of the dielectric core, of the first six modes supported by a 'zigzag patch array' structure. Red and blue regions correspond to high and zero field enhancement respectively.

etry, the unit cells of which, do not contain any mirror planes. However, given that the limiting frequency of the surface modes supported by the array is dictated by the frequency at which the localised modes of the hole are supported, it would be advantageous to ensure each hole within the array supports a localised mode at the same frequency. In doing so, the increased anisotropy would have to arise from the pitch of neighbouring pairs of elements being different. Filling the holes with different dielectric materials may be a way of tuning the resonances supported by the holes, such that, even if the size of the hole in neighbouring elements was designed to be different (to account for the requirement of the pitch of neighbouring elements to be different) each hole would still support localised modes at identical frequencies. It is anticipated that recording the 'enhanced' transmission through the structure at several different azimuthal angles may yield interesting polarisation-dependent results.

Further, an obvious extension of the work in Chapter 7 would be to explore the response of a Sievenpiper-type and simpler patch array structure with reduced symmetry. In particular it may be interesting to compare the response of the zigzag hole array structure to for instance, a Sievenpiper and patch array structure, the patch array of which comprises arrays a rhombic-shaped patches in a 'zigzag geometry'. Whilst diffraction from the dual periodicity is expected to be a much weaker perturbation on the band structure than that observed in the response of the zigzag hole array. It is anticipated, due to the novel symmetry of the modes supported underneath each patch (as shown in Fig. 8.1 for 'a zigzag patch array') in the dielectric layer, that a highly-anisotropic response as a function of azimuthal angle would be observed.

Finally it may be favourable to spend some time developing the technique in which the dispersion of the surface mode is directly recorded using phase-resolved measurements. In particular it would be advantageous to explore methods to extend the region

of k-space that the surface modes can be experimentally characterised. Exploring different excitation techniques may possible be a route to achieving this, with the ultimate aim of being able to experimentally characterise the negative slope of the dispersion of the lowest order TM surface mode supported by the Sievenpiper structure in Chapter 7.

Chapter 9

Publications and Presentations

9.1 Publications

- Rance H. J., Constant T. J., Hibbins A. P. and Sambles J. R. 'Surface waves at microwave frequencies excited on a zigzag metasurface.' *Physical Review B* **86** 125144 (2012)
- Constant T. J., Taphouse T. S., Rance H. J., Kitson S. C., Hibbins A. P., and Sambles J. R. 'Surface plasmons on zig-zag gratings.' *Optics Express* **20** 23921 (2012)
- Rance H. J., Hooper I. R., Hibbins A. P. and Sambles J. R. 'Structurally dictated anisotropic designer surface plasmons' *Applied Physics Letters* **99** 181107 (2011)
- Rance H. J., Hamilton O. K., Hibbins A. P. and Sambles J. R. 'Phase resonances on metal gratings of identical, equally spaced alternately tapered slits.' *Applied Physics Letters* **95** 041905 (2009)

9.2 Oral Presentations

- Cimtec 2012, Rance H. J., Hibbins A. P. and Sambles J. R., 'Novel pseudo-plasmonic surfaces in the microwave regime', Montecatini Terme, Italy, June 2012.

9.3 Poster Presentations

- Metamaterials 2011, Rance H. J., Hibbins A. P. and Sambles J. R., 'Microwave transmission of a zigzag hole array', Barcelona, Spain, October 2011.
- PECS-IX 2010, Rance H. J., Hibbins A. P. and Sambles J. R., 'Grating excitation of microwave surface modes supported by metamaterials', Granada, Spain, September 2010.

- The Royal Society, Theo Murphy International Scientifc Meeting on Metallic Metamaterials and Plasmonics, Rance H. J., Hibbins A. P. and Sambles J. R., 'Excitation of microwave modes supported by deep hole arrays', Chicheley Hall, United Kingdom, June 2010.

- Nanometa 2009, Rance H. J., Hamilton O. K., Hibbins A. P. and Sambles J. R., 'Phase resonances supported by transmission gratings of tapered-width slits', Seefeld, Austria, January 2009.

References

[1] Hooper, I.R. *The Optical Response of Short-Pitch Surface- Relief Gratings*. Ph.D. thesis, University of Exeter (2002). viii, 10, 13

[2] Hibbins, A.P., Evans, B.R., and Sambles, J.R. Experimental verification of designer surface plasmons. *Science (New York, N.Y.)*, **308**, 670 (2005). ix, x, 1, 16, 22, 23, 39, 40, 41, 45, 67, 88

[3] Pendry, J.B., Martín-Moreno, L., and Garcia-Vidal, F.J. Mimicking Surface Plasmons with Structured Surfaces. *Science*, **305**, 847 (2004). ix, 1, 4, 5, 16, 21, 22, 23, 37, 38, 39, 40, 67, 113

[4] Garcia-Vidal, F.J., Martín-Moreno, L., and Pendry, J.B. Surfaces with holes in them: new plasmonic metamaterials. *Journal of Optics A: Pure and Applied Optics*, **7**, S97 (2005). ix, 1, 16, 17, 21, 22, 23, 37, 67

[5] García de Abajo, F.J. and Sáenz, J.J. Electromagnetic Surface Modes in Structured Perfect-Conductor Surfaces. *Physical Review Letters*, **95**, 233901 (2005). ix, 22, 23, 38

[6] Hendry, E., Hibbins, A.P., and Sambles, J.R. Importance of diffraction in determining the dispersion of designer surface plasmons. *Physical Review B*, **78**, 235426 (2008). ix, 16, 22, 23, 38, 40, 67, 70

[7] Brillouin, L. Wave Guides for Slow Waves. *Journal of Applied Physics*, **19**, 1023 (1948). 1, 5, 113

[8] Rotmant, W. A Study of Single-Surface Corrugated Guides. *Proceedings of the IRE*, **39**, 952 (1951).

[9] Barlow, H. and Cullen, A.L. Surface Waves. *Proceedings of the IEE - Part III: Radio and Communication Engineering*, **100**, 329 (1953). 4, 16

[10] Elliot, R.S. On the Theory of Corregated Plane Surfaces. *IRE Transactions Antennas and Propagation*, **2**, 71 (1954).

[11] Harvey, A.F. Periodic and Guiding Structures at Microwave Frequencies. *IRE Transactions on Microwave Theory and Techniques*, **8**, 30 (1960). 1, 4

[12] Cutler, C. Genesis of the corrugated electromagnetic surface. *Proceedings of IEEE Antennas and Propagation Society International Symposium and URSI National Radio Science Meeting*, **3**, 1456 (1994). 1, 5, 16, 113

[13] Ulrich, R. and Tacke, M. Submillimeter waveguiding on periodic metal structure. *Applied Physics Letters*, **22**, 251 (1973). 1, 16

[14] Fano, U. The Theory of Anomalous Diffraction Gratings and of Quasi-Stationary Waves on Metallic Surfaces (Sommerfeld's Waves). *Journal of Optical Society of America*, **31**, 213 (1941). 4

[15] Mills, D.L. and Burstein, E. Polaritons : the electromagnetic modes of media. *Reports on Progress in Physics*, **817**, 37 (1974). 5

[16] Barnes, W.L., Dereux, A., and Ebbesen, T.W. Surface plasmon subwavelength optics. *Nature*, **424**, 824 (2003). 5

[17] Zenneck, J. Uber die Fortpanzung ebener elektromagnetischer Wellen langseiner ebenen Leiterache und ihre Beziehung zur drahtlosen Telegraphie. *Annalen der Physik*, **328**, 846 (1907). 5

[18] Sommerfeld, A. The broadening of the waves and the wireless telegraph. *Annalen der Physik*, **28** (1909). 5

[19] Drude, P. Zur Elektronentheorie der Metalle. *Annalen der Physik*, **306**, 566 (1900). 8

[20] Butler, C.A.M. *The Microwave Response of Square Mesh Metamaterials*. Ph.D. thesis, University of Exeter (2012). 8

[21] Hibbins, A.P., Sambles, J.R., and Lawrence, C.R. Excitation of remarkably nondispersive surface plasmons on a nondiffracting, dual-pitch metal grating. *Applied Physics Letters*, **80**, 2410 (2002). 11, 98

[22] Hibbins, A.P., Hooper, I.R., Lockyear, M.L., and Sambles, J.R. Microwave Transmission of a Compound Metal Grating. *Physical Review Letters*, **96**, 257402 (2006). 45, 87, 98

[23] Rance, H.J., Hamilton, O.K., Sambles, J.R., and Hibbins, A.P. Phase resonances on metal gratings of identical, equally spaced alternately tapered slits. *Applied Physics Letters*, **95**, 041905 (2009). 11, 45, 87, 89, 98

[24] Barnes, W.L., Preist, T.W., Kitson, S.C., and Sambles, J.R. Physical origin of photonic energy gaps in the propagation of surface plasmons on gratings. *Physical Review B*, **54**, 6227 (1996). 15, 102

[25] Barnes, W.L., Kitson, S.C., Preist, T.W., and Sambles, J.R. Photonic surfaces for surface-plasmon polaritons. *Journal of the Optical Society of America A*, **14**, 1654 (1997). 15, 102

[26] Williams, C.R., Andrews, S.R., Maier, S.A., Fernández-Domínguez, A.I., Martín-Moreno, L., and García-Vidal, F.J. Highly confined guiding of terahertz surface plasmon polaritons on structured metal surfaces. *Nature Photonics*, **2**, 175 (2008). 16, 39, 67

[27] Qiu, M. Photonic band structures for surface waves on structured metal surfaces. *Optics Express*, **13**, 7583 (2005). 16

[28] Hibbins, A.P., Hendry, E., Lockyear, M.J., and Sambles, J.R. Prism coupling to 'designer' surface plasmons. *Optics Express*, **16**, 20441 (2008).

[29] Gan, Q., Fu, Z., Ding, Y., and Bartoli, F. Ultrawide-Bandwidth Slow-Light System Based on THz Plasmonic Graded Metallic Grating Structures. *Physical Review Letters*, **100**, 256803 (2008).

[30] Shen, J., Catrysse, P., and Fan, S. Mechanism for Designing Metallic Metamaterials with a High Index of Refraction. *Physical Review Letters*, **94**, 197401 (2005).

[31] Ruan, Z. and Qiu, M. Slow electromagnetic wave guided in subwavelength region along one-dimensional periodically structured metal surface. *Applied Physics Letters*, **90**, 201906 (2007). 16, 68

[32] Maier, S.A., Andrews, S.R., Martín-Moreno, L., and García-Vidal, F. Terahertz Surface Plasmon-Polariton Propagation and Focusing on Periodically Corrugated Metal Wires. *Physical Review Letters*, **97**, 176805 (2006). 16, 67

[33] Fernández-Domínguez, A., Moreno, E., Martín-Moreno, L., and García-Vidal, F. Guiding terahertz waves along subwavelength channels. *Physical Review B*, **79**, 233104 (2009).

[34] Navarro-Cía, M., Beruete, M., Agrafiotis, S., Falcone, F., Sorolla, M., and Maier, S.A. Broadband spoof plasmons and subwavelength electromagnetic energy confinement on ultrathin metafilms. *Optics Express*, **17**, 18184 (2009).

[35] Martin-Cano, D., Nesterov, M.L., Fernandez-Dominguez, A.I., Garcia-Vidal, F.J., Martin-Moreno, L., and Moreno, E. Domino plasmons for subwavelength terahertz circuitry. *Optics Express*, **18**, 754 (2010).

[36] Wood, J.J., Tomlinson, L.A., Hess, O., Maier, S.A., and Fernández-Domínguez, A.I. Spoof plasmon polaritons in slanted geometries. *Physical Review B*, **85**, 075441 (2012). 16

[37] Fernandez-Dominguez, A.I., Williams, C.R., Garcia-Vidal, F.J., Martin-Moreno, L., Andrews, S.R., and Maier, S.A. Terahertz surface plasmon polaritons on a helically grooved wire. *Applied Physics Letters*, **93**, 141109 (2008). 16

[38] Zhu, W., Agrawal, A., and Nahata, A. Planar plasmonic terahertz guided-wave devices. *Optics Express*, **16**, 6216 (2008).

[39] Lockyear, M.J., Hibbins, A.P., and Sambles, J.R. Microwave Surface-Plasmon-Like Modes on Thin Metamaterials. *Physical Review Letters*, **102**, 073901 (2009). 116

[40] Zhao, W., Eldaiki, O.M., Yang, R., and Lu, Z. Deep subwavelength waveguiding and focusing based on designer surface plasmons. *Optics Express*, **18**, 21498 (2010).

[41] Williams, C.R., Misra, M., Andrews, S.R., Maier, S.a., Carretero-Palacios, S., Rodrigo, S.G., Garcia-Vidal, F.J., and Martin-Moreno, L. Dual band terahertz waveguiding on a planar metal surface patterned with annular holes. *Applied Physics Letters*, **96**, 011101 (2010).

[42] Kumar, G., Pandey, S., Cui, A., and Nahata, A. Planar plasmonic terahertz waveguides based on periodically corrugated metal films. *New Journal of Physics*, **13**, 033024 (2011).

[43] Kim, S.H., Kim, T.T., Oh, S., Kim, J.E., Park, H., and Kee, C.S. Experimental demonstration of self-collimation of spoof surface plasmons. *Physical Review B*, **83**, 165109 (2011).

[44] Brock, E.M.G., Hendry, E., and Hibbins, A.P. Subwavelength lateral confinement of microwave surface waves. *Applied Physics Letters*, **99**, 051108 (2011). 31, 38

[45] Ma, Y.G., Lan, L., Zhong, S.M., and Ong, C.K. Experimental demonstration of subwavelength domino plasmon devices for compact high-frequency circuit. *Optics Express*, **19**, 21189 (2011).

[46] Jin Zhou, Y., Jiang, Q., and Jun Cui, T. Bidirectional bending splitter of designer surface plasmons. *Applied Physics Letters*, **99**, 111904 (2011).

[47] Jiang, T., Shen, L., Wu, J.J., Yang, T.J., Ruan, Z., and Ran, L. Realization of tightly confined channel plasmon polaritons at low frequencies. *Applied Physics Letters*, **99**, 261103 (2011). 16

[48] Yu, N., Wang, Q.J., Kats, M.A., Fan, J.A., Khanna, S.P., Li, L., Davies, A.G., Linfield, E.H., and Capasso, F. Designer spoof surface plasmon structures collimate terahertz laser beams. *Nature Materials*, **9**, 730 (2010). 16

[49] Huang, X.R., Peng, R.W., and Fan, R.H. Making Metals Transparent for White Light by Spoof Surface Plasmons. *Physical Review Letters*, **105**, 243901 (2010). 16

[50] Khanikaev, A.B., Mousavi, S.H., Shvets, G., and Kivshar, Y.S. One-Way Extraordinary Optical Transmission and Nonreciprocal Spoof Plasmons. *Physical Review Letters*, **105**, 126804 (2010). 16

[51] Smith, D.R. and Pendry, J.B. Homogenization of metamaterials by field averaging (invited paper). *Journal of the Optical Society of America B*, **23**, 391 (2006). 16, 40

[52] Nazarov, M. and Coutaz, J.L. Terahertz Surface Waves Propagating on Metals with Sub-wavelength Structure and Grating Reliefs. *Journal of Infrared, Millimeter, and Terahertz Waves*, **32**, 1054 (2011). 16

[53] Sievenpiper, D., Zhang, L., Broas, R., Alexopolous, N., and Yablonovitch, E. High-Impedance Electromagnetic Surfaces with a Forbidden Frequency Band. *IEEE Transactions on Microwave Theory and Techniques*, **47**, 2059 (1999). 18, 113

[54] Clavijo, S., Díaz, R.E., and Mckinzie, W.E. Design Methodology for Sievenpiper High-Impedance Surfaces: An Artificial Magnetic Conductor for Positive Gain Electrically Small Antennas. *IEEE Transactions on Antennas and Propagation*, **51**, 2678 (2003). 18, 22, 114, 132

[55] Pozar, D. *Microwave Engineering.* John Wiley & Sons, Inc (2005). 19

[56] Lan, Y.C. and Chern, R.L. Surface plasmon-like modes on structured perfectly conducting surfaces. *Optics Express*, **14**, 11339 (2006). 22, 38, 40, 67

[57] García de Abajo, F. Colloquium: Light scattering by particle and hole arrays. *Reviews of Modern Physics*, **79**, 1267 (2007).

[58] Shen, L., Chen, X., and Yang, T.J. Terahertz surface plasmon polaritons on periodically corrugated metal surfaces. *Optics Express*, **16**, 3326 (2008). 22, 38, 40, 67

[59] Stone, E. and Hendry, E. Dispersion of spoof surface plasmons in open-ended metallic hole arrays. *Physical Review B*, **84**, 035418 (2011). 23, 39, 96

[60] *Flann Microwave: Microwave Products, Bodmin, United Kingdom* (2010). 27

[61] Unknown. *The Essentials of Vector Network Analysis.* Anritsu (USA) (2009). 29

[62] Saxler, J., Gómez Rivas, J., Janke, C., Pellemans, H.P.M., Haring Bolívar, P., and Kurz, H. Time-domain measurements of surface plasmon polaritons in the terahertz frequency range. *Physical Review B*, **69**, 155427 (2004). 30

[63] Maier, S.a., Andrews, S.R., Martín-Moreno, L., and García-Vidal, F.J. Terahertz surface plasmon polariton propagation and focusing on periodically corrugated metal wires. *Optics Express*, **14**, 13021 (2006). 30

[64] *Morganic Metal Solutions Ltd , Farnham, United Kingdom.* 32

[65] ANSYS. ANSYS HFSS (2012). 33

[66] Kopp, M. *An Introduction to HFSS:Fundamental Principles, Concepts, and Use.* ANSYS Inc, Pittsburgh, PA (2009). 33, 91

[67] Hibbins, A.P., Lockyear, M.J., and Sambles, J.R. Otto coupling to a transverse-electric-polarized mode on a metamaterial surface. *Physical Review B*, **84**, 115130 (2011). 38, 116, 118

[68] Kushiyama, Y., Arima, T., and Uno, T. Experimental verification of spoof surface plasmons in wire metamaterials. *Optics Express*, **20**, 18238 (2012). 38, 39

[69] Berry, S.J., Campbell, T., Hibbins, A.P., and Sambles, J.R. Surface wave resonances supported on a square array of square metallic pillars. *Applied Physics Letters*, **100**, 101107 (2012). 39, 69

[70] Rance, H.J., Hooper, I.R., Hibbins, A.P., and Sambles, J.R. Structurally dictated anisotropic "designer surface plasmons". *Applied Physics Letters*, **99**, 181107 (2011). 39

[71] Maier, S.A. and Andrews, S.R. Terahertz pulse propagation using plasmon-polariton-like surface modes on structured conductive surfaces. *Applied Physics Letters*, **88**, 251120 (2006). 39, 67

[72] Wang, J., Qu, S., Ma, H., Xu, Z., Zhang, A., Zhou, H., Chen, H., and Li, Y. High-efficiency spoof plasmon polariton coupler mediated by gradient metasurfaces. *Applied Physics Letters*, **101**, 201104 (2012). 39

[73] Hibbins, A.P., Sambles, J.R., and Lawrence, C.R. Grating-coupled surface plasmons at microwave frequencies. *Journal of Applied Physics*, **86**, 1791 (1999). 39

[74] Hooper, I.R. and Sambles, J.R. Dispersion of surface plasmon polaritons on short-pitch metal gratings. *Physical Review B*, **65**, 165432 (2002). 40

[75] Herminghaus, S., Klopfleisch, M., and Schmidt, H.J. Attenuated total reflectance as a quantum interference phenomenon. *Optics Letters*, **19**, 293 (1994). 44

[76] Collin, R.E. *Field Theory of Guided Waves*. John Wiley & Sons, New York (1990). 52, 128

[77] Tanaka, M., Miyamaru, F., Hangyo, M., Tanaka, T., Akazawa, M., and Sano, E. Effect of a thin dielectric layer on terahertz transmission characteristics for metal hole arrays. *Optics Letters*, **30**, 1210 (2005). 63

[78] Han, J., Lu, X., and Zhang, W. Terahertz transmission in subwavelength holes of asymmetric metal-dielectric interfaces: The effect of a dielectric layer. *Journal of Applied Physics*, **103**, 033108 (2008).

[79] Miyamaru, F., Sasagawa, Y., and Takeda, M.W. Effect of dielectric thin films on reflection properties of metal hole arrays. *Applied Physics Letters*, **96**, 021106 (2010). 63

[80] Ruan, Z. and Qiu, M. Enhanced Transmission through Periodic Arrays of Subwavelength Holes: The Role of Localized Waveguide Resonances. *Physical Review Letters*, **96**, 233901 (2006). 67

[81] Feng, L., Liu, Z., Lomakin, V., and Fainman, Y. Form birefringence metal and its plasmonic anisotropy. *Applied Physics Letters*, **96**, 041112 (2010). 68

[82] Jiang, T., Shen, L., Zhang, X., and Ran, L. Progress In Electromagnetics Research M, Vol. 8, 91–102, 2009. *Progress In Electromagnetic Research M*, **8**, 91 (2009). 68

[83] Qiu, M. Photonic band structures for surface waves on structured metal surfaces. *Optics Express*, **13**, 7583 (2005). 68

[84] Edmunds, J.D., Hendry, E., Hibbins, A.P., Sambles, J.R., and Youngs, I.J. Multi-modal transmission of microwaves through hole arrays. *Optics Express*, **19**, 13793 (2011). 69, 88

[85] Born, M. and Wolf, E. *Principles of Optics*. Cambridge University Press, 7th edition (1999). 83

[86] Fedotov, V.A., Rose, M., Prosvirnin, S.L., Papasimakis, N., and Zheludev, N.I. Sharp Trapped-Mode Resonances in Planar Metamaterials with a Broken Structural Symmetry. *Physical Review Letters*, **99**, 147401 (2007). 87

[87] Plum, E., Fedotov, V.A., and Zheludev, N.I. Planar metamaterial with transmission and reflection that depend on the direction of incidence. *Applied Physics Letters*, **94**, 131901 (2009). 87

[88] Abdeddaim, R., Ourir, A., and Rosny, J.D. Realizing a negative index metamaterial by controlling hybridization of trapped modes. *Physical Review B*, **83**, 033101 (2011).

[89] Kang, M., Cui, H.X., Li, Y., Gu, B., Chen, J., and Wang, H.T. Fano–Feshbach resonance in structural symmetry broken metamaterials. *Journal of Applied Physics*, **109**, 014901 (2011). 87

[90] Aydin, K., Pryce, I.M., and Atwater, H.A. Symmetry breaking and strong coupling in planar optical metamaterials. *Optics Express*, **18**, 13407 (2010). 87

[91] Singh, R., Al-naib, I.A.I., Yang, Y., Chowdhury, D.R., Cao, W., Rockstuhl, C., Ozaki, T., Morandotti, R., and Zhang, W. Observing metamaterial induced transparency in individual Fano resonators with broken symmetry. *Applied Physics Letters*, **99**, 201107 (2011). 87

[92] Tuz, V.R., Prosvirnin, S.L., and Kochetova, L.A. Optical bistability involving planar metamaterials with broken structural symmetry. *Physical Review B*, **82**, 233402 (2010). 87

[93] Burokur, S.N., Sellier, A., Kante, B., and de Lustrac, A. Symmetry breaking in metallic cut wire pairs metamaterials for negative refractive index. *Applied Physics Letters*, **94**, 201111 (2009). 87

[94] Aydin, K., Ferry, V.E., Briggs, R.M., and Atwater, H.A. Broadband polarization-independent resonant light absorption using ultrathin plasmonic super absorbers. *Nature Communications*, **2**, 517 (2011). 87

[95] Liu, Z. and Jin, G. Phase effects in the enhanced transmission through compound subwavelength rectangular hole arrays. *Journal of Applied Physics*, **106**, 063122 (2009). 87

[96] Ebbesen, T.W., Lezec, H.J., Ghaemi, H.F., Thio, T., and Wolff, P. Extraordinary optical transmission through sub-wavelength hole arrays. *Nature*, **391**, 667 (1995). 87

[97] Bethe, H.A. Theory of Diffraction by Small Holes. *Physical Review*, **66**, 163 (1944). 88

[98] Ghaemi, H.F. and Thio, T. Extraordinary optical transmission through subwavelength hole arrays. *Nature* (1998). 88

[99] Martín-Moreno, L., García-Vidal, F.J., Lezec, H.J., Pellerin, K.M., Thio, T., Pendry, J.B., and Ebbesen, T.W. Theory of Extraordinary Optical Transmission through Subwavelength Hole Arrays. *Physical Review Letters*, **86**, 1114 (2001). 88

[100] Darmanyan, S.A. and Zayats, A.V. Light tunneling via resonant surface plasmon polariton states and the enhanced transmission of periodically nanostructured metal films: An analytical study. *Physical Review B*, **67**, 035424 (2003). 88

[101] Barnes, W.L., Murray, W.A., Dintinger, J., Devaux, E., and Ebbesen, T.W. Surface Plasmon Polaritons and Their Role in the Enhanced Transmission of Light through Periodic Arrays of Subwavelength Holes in a Metal Film. *Physical Review Letters*, **92**, 107401 (2004). 88

[102] Beruete, M., Sorolla, I., Campillo, J.S., Dolado, L., Martín-Moreno, J., Bravo-Abad, and García-Vidal, F.J. Enhanced millimetre wave transmission through subwavelength hole arrays. *Optics Letters*, page 2500 (2004). 88

[103] Beruete, M., Sorolla, M., Campillo, I., and Dalado, L. Increase of the transmission in cut-off metallic hole arrays. *Microwave and Wireless Component Letters, IEEE*, **15**, 116 (2005).

[104] García de Abajo, J.F., Gomez-Medina, R., and Sanez, J. Full transmission through perfect-conductor subwavelength hole arrays. *Physical Review E*, **72**, 016608 (2005).

[105] García de Abajo, J.F. and Sanez, J.J. Electromagnetic surface modes in structured perfect-conductor surface. *Physical Review Letters* (2005).

[106] Hou, B., Hang, Z.H., Wen, W., Chan, C.T., and Sheng, P. Microwave transmission through metallic hole arrays: Surface electric field measurements. *Applied Physics Letters*, page 3 (2006).

[107] Hibbins, A.P., Lockyear, M.J., Hooper, I.R., and Sambles, J.R. Surface plasmons enhance optical transmission through subwavelength holes. *Physical Review Letters*, **96**, 073904 (2006).

[108] Beruete, M., Campillo, I., Navarro-cía, M., Falcone, F., Ayza, M.S., and Member, S. Molding Left- or Right-Handed Metamaterials by Stacked Cutoff Metallic Hole Arrays. **55**, 1514 (2007).

[109] Medina, F., Mesa, F., and Marqués, R. Extraordinary Transmission Through Arrays of Electrically Small Holes From a Circuit Theory Perspective. **56**, 3108 (2008).

[110] Miyamaru, F., Kamijyo, M., Hanaoka, N., and Takeda, M.W. Controlling extraordinary transmission characteristics of metal hole arrays with spoof surface plasmons. *Applied Physics Letters*, **100**, 081112 (2012). 88

[111] Liu, J., Ding, L., Wang, K., and Yao, J. A method to design transmission resonances through subwavelength apertures based on designed surface plasmons. *Optics Express*, **17**, 12714 (2009). 89

[112] Overfelt P. L. and Kenney C. S. Power-handling capability of the rhombic waveguide. *IEEE Transactions on Microwave Theory and Techniques*, **38**, 934 (1990). 92

[113] Overfelt P. L. and White D. J. Short Papers. *IEEE Transactions on Microwave Theory and Techniques*, **34**, 161 (1986). 92

[114] Economou, E.N. Surface Plasmons in Thin Films. *Physical Review*, **2**, 539 (1969). 95

[115] Hooper, I.R. and Sambles, J.R. Coupled surface plasmon polaritons on thin metal slabs corrugated on both surfaces. *Physical Review B*, **70**, 045421 (2004). 95, 102

[116] Munk, B.A. *Frequency Selective Surfaces: Theory and Design*. Wiley, New York (2000). 113

[117] Yang, F. and Rahmat-Samii, Y. Reflection Phase Characterizations of the EBG Ground Plane for Low Profile Wire. *IEEE Transactions on Antennas and Propagation*, **51**, 2691 (2003). 114

[118] Aminian, A., Yang, F., and Rahmat-Samii, Y. In-phase reflection and EM wave suppression characteristics of electromagnetic band gap ground planes. *IEEE Antennas and Propagation Society International Symposium.*, **4**, 430 (2003).

[119] Goussetis, G., a.P. Feresidis, and Vardaxoglou, J. Tailoring the AMC and EBG Characteristics of Periodic Metallic Arrays Printed on Grounded Dielectric Substrate. *IEEE Transactions on Antennas and Propagation*, **54**, 82 (2006). 115

[120] Li, L., Chen, Q., Yuan, Q., Liang, C., and Sawaya, K. Surface-wave suppression band gap and plane-wave reflection phase band of mushroom-like photonic band gap structures. *Journal of Applied Physics*, **103**, 023513 (2008). 115

[121] Samani, M.F., Borji, A., and Safian, R. Relation Between Reflection Phase and Surface-Wave Bandgap in Artificial Magnetic Conductors. *IEEE Transactions on Microwave Theory and Techniques*, **59**, 1901 (2011). 114

[122] Zhang, Y., Member, S., Member, S., Younis, M., Fischer, C., and Wiesbeck, W. Patch Antennas. *October*, **51**, 2704 (2003). 115

[123] Feresidis, A., Goussetis, G., and Vardaxoglou, J. Artificial magnetic conductor surfaces and their application to low-profile high-gain planar antennas. *IEEE Transactions on Antennas and Propagation*, **53**, 209 (2005). 115

[124] Yang, F. and Rahmat-Samii, Y. Polarization-dependent electromagnetic band gap (PDEBG) structures: Designs and applications. *Microwave and Optical Technology Letters*, **41**, 439 (2004). 116

[125] Yan, D., Gao, Q., Wang, C., Zhu, C., and Yuan, N. A Novel Polarization Convert Surface Based on Artificial Magnetic Conductor. *Microwave Conference Proceedings, 2005. APMC 2005. Asia-Pacific Conference Proceedings*, **3**, 1 (2005). 116

[126] Fu, Y. and Yuan, N. Surface-Wave Bandgap of Polarization Dependent Electromagnetic Bandgap Structures. *Microwave and Optical Technology Letters*, **49**, 946 (2007). 116

[127] Tretyakov, S. *Analytical Modelling in Applied Electromagnetics*. Artech House Publishing (2003). 124

[128] Brown, J. Artificial Dielectrics having Refractive Index Less than Unity. *Proceedings of the IEE - Part IV: Institution Monographs*, **100**, 51 (1953). 131

[129] Rotman, W. Plasma Simulation by Artifical Dielectrics. *IRE Transactions Antennas and Propagation*, **10**, 82 (1962). 131, 132

[130] Berreman, D.W. Optics in stratified and anisotropic media: 4x4-matrix formulation. *Journal of the Optical Society of America*, **62**, 502 (1972). 134